PORTABLE MAGNETIC TRACKING SYSTEMS EXPLOITING NEURAL NETWORKS AND SPACE MAPPING MODELING

To my parents

PORTABLE MAGNETIC TRACKING SYSTEMS EXPLOITING NEURAL NETWORKS AND SPACE MAPPING MODELING

By

KAI WANG, B. ENG.

A Thesis

Submitted to the School of Graduate Studies

in Partial Fulfillment of the Requirements

for the Degree

Master of Applied Science

McMaster University

MASTER OF APPLIED SCIENCE (2008) McMaster University
(Electrical and Computer Engineering) Hamilton, Ontario

TITLE: **PORTABLE MAGNETIC TRACKING SYSTEMS EXPLOITING NEURAL NETWORKS AND SPACE MAPPING MODELING**

AUTHOR: KAI WANG
B. ENG.
(Electrical Engineering, McMaster University, Canada)

SUPERVISOR: Dr. Mohamed H. Bakr, Associate Professor
Department of Electrical and Computer Engineering
B. Sc. (Cario University, Egypt)
M. Sc. (Cario University, Egypt)
Ph. D. (McMaster University, Canada)
P. Eng. (Province of Ontario)

CO-SUPERVISOR: Dr. M. Jamal Deen, Professor and Senior Canada Research Chair in Information Technology
Department of Electrical and Computer Engineering
B. Sc. (University of Guyana, South American)
M. S. (Case Western Reserve University, USA)
Ph. D. (Case Western Reserve University, USA)
F.R.S.C., F.C.A.E., F.I.E.E.E., F.E.I.C., F.E.C.S., F.A.A.A.S.

NUMBER OF PAGES xv, 138

ABSTRACT

The traditional approach of Magnetic Tracking Systems (MTS) utilizes approximate models and Parameter Extraction (PE) for Position and Orientation (P&O) determination. The approximate models give inaccurate P&O information outside the "constrained region". PE is an iterative, intensive process for P&O calculations, which limits the speed of the tracking process.

Our MTS approach aims at accurate real-time P&O tracking. We utilize Artificial Neural Networks (ANN) with PE functionality to carry out the computational task for real-time P&O tracking. We apply Space Mapping (SM) modeling afterwards for system calibration to improve the accuracy of P&O determination.

This thesis addresses a different approach for P&O determination. The main motivation of this work is to determine the P&O in a fast and accurate manner. It this work, we mathematically develop and experimentally implement our MTS for both 2-D and 3-D examples. The results show good match between our extracted P&O based on our MTS approach and the actual P&O measured values.

ACKNOWLEDGMENTS

The author wishes to express his greatest appreciation to his supervisor, Dr. Mohamed H. Bakr, the Computational Electromagnetics Research Laboratory, McMaster University, for his expert supervision, continuous encouragement and constant support throughout this work.

The author would also like to offer his greatest gratitude to his co-supervisor, Dr. M. Jamal Deen, the Microelectronics Research Laboratory, McMaster University, for his professional advice and expert guidance in this research.

The author would also like to express his appreciation to Dr. O. Marinov for his technical support throughout this work.

The author wishes to thank his colleagues in the Computational Electromagnetics Research Laboratory and the Simulation Optimization Systems Research Laboratory of the Department of Electrical and Computer Engineering at McMaster University, for their useful comments and valuable discussions.

The author greatly acknowledges the financial support provided by NSERC, PREA, and the Department of Electrical and Computer Engineering, McMaster

University. The author also wishes to thank all the staff members of the ECE department for their assistance and support, especially Cheryl Gies, Terry Greenlay, and Cosmin Coroiu.

Finally, the author would like to express his deep gratitude to his family for their continuous understanding, encouragement and unconditional support.

CONTENTS

LIST OF FIGURES

LIST OF TABLES

CHAPTER 1

INTRODUCTION

1.1 MOTIVATION

Gastrointestinal diseases are commonly occurring diseases and are of great international concern. People may notice abnormal bleeding such as blood in vomits. Sometimes, continuous blood loss goes unnoticed. The source of bleeding has to be identified. The full visualization of the entire gastrointestinal track is required for diagnostic purposes.

The traditional method is to use wired "scope" equipped with camera and illumination source for both gastroscopy and colonoscopy. Gastroscopy is used to examine the upper digestive system [1]. Colonoscopy is used examine the lower digestive system [2]. Unfortunately, in some cases the bleeding problem lies somewhere in between the upper and lower digestive systems where traditional gastroscopy and colonoscopy cannot reach [3]. Scopes with longer cable do not help due to difficulty in its control and manipulation [3]. Furthermore, the examination is an uncomfortable procedure because of

the wire and optical fibers needed for imaging and powering purposes.

Ingestible medical devices such as the wireless capsule endoscopy (also known as capsule endoscopy or wireless endoscopy) are finding increasing use in diagnosing and monitoring the gastrointestinal track, especially within the small intestine. It has a color video camera fitted inside a pill and a wireless radiofrequency transmitter to send the observation images outside the body. It is easy to swallow with just a sip of water. It moves along the digestive track naturally with the aid of intestinal muscle activities. The patients can continue their regular activities comfortably during the examination [3].

Commercial ingestible image devices are available, such as PillCam [4], EndoCapsule [5], Sayaka and Norika3 [6], MicroCam [7] and OMOM [8].

The image devices can tell us of the existence of the problem source. However, it cannot tell us the location of the problem source. If we would like to monitor the recovery status of a certain bleeding source for diagnostics purposes, position information is required to be correlated with the observed images.

The major techniques for position and orientation determination include magnetic tracking, optical tracking and ultrasonic tracking. A magnetic tracking system is the best candidate for wireless endoscopy applications. In electromagnetic tracking, the magnetic field value is position-dependent. The low frequency magnetic field penetrates the body without attenuation or change so the tracking may be continuous during the entire operation. More importantly, the field is not limited by line-of-sight due to operating room personnel moving into positions that obstruct the line-of-sight paths, which is

usually required for optical tracking and ultrasonic tracking [9].

Optical or ultrasonic tracking, by contrast, may require a large or excess number of line-of-sight paths and corresponding detectors to assure that position can be determined by triangulation despite occluded pathways [9]. The body-penetrating electromagnetic fields also allow tracking the location or movements inside the body with minimal resort to the fluoroscopic or ultrasound techniques normally required for visualization [9].

Most of these devices utilize a magnetic field as the signal source for position and orientation determination [10] - [19].

1.2 OVERVIEW OF THE THESIS

This thesis consists of two major parts. The first part (chapter 2~4) provides the comprehensive reviews of Magnetic Tracking Systems (MTS) and the relevant concepts of Space Mapping (SM) and Artificial Neural Networks (ANN). These researches are the building blocks for the works reported in this thesis. The second part (chapter 5~6) presents the major contributions and implementations of MTS for both 2-D and 3-D cases.

Chapter 2 reviews the basic concepts of MTS. We present various implementations and its corresponding features. We mathematically develop how to utilize Faraday's induction law and Biot-Savart's law to implement our own portable MTS for wireless endoscopy application.

Chapter 3 reviews the concept of ANN, including their structures, information propagation and the development of the ANN model. We also present the mathematical formulation for the ANN training process. The ***NeuroModeler*** software [20] is introduced for automated ANN model generation.

In Chapter 4, we briefly review the concept of Space Mapping (SM) and its framework for optimization and modeling. We present different mapping methods in SM to match surrogate model responses with the corresponding fine model responses. Parameter Extraction (PE) is the key to establish the mapping and updating of the surrogate model. The framework for SM optimization and SM modeling is presented step by step.

In Chapter 5 and Chapter 6, we present our portable MTS exploiting ANN and SM modeling. We design a suitable geometrical configuration for our MTS such that patients can continue their regular activities during the Position and Orientation (P&O) tracking. Under this design constrain, we optimize the geometrical shape of the field generating elements of the field generator in order to achieve signals of high sensitivity with respect to P&O change.

A MatLab [21] program is developed to model the electromagnetic field distribution. PE is implemented using the MatLab optimization toolbox to verify the mathematical algorithm of P&O determination.

We apply ANN model for real-time P&O tracking, which is traditionally done by an iterative PE process. We utilize SM modeling to improve the accuracy of P&O

responses. The quality of the determined orientation is evaluated by a Quality Factor (QF), which will tells us how accurate the orientation measurement is in advance, without knowing the actual orientation.

We combine the ANN and SM modeling to achieve short computational time and accurate P&O determination simultaneously without the time consuming complex fine model development. Very good match of P&O is obtained between our calculated P&O and the actual P&O.

In Chapter 7, we conclude with a summary of the research contributions and future works.

1.3 CONTRIBUTIONS

The author contributed to the following developments presented in this thesis:

1. Mathematically developed 6 degree-of-freedom MTS algorithm.
2. Determined geometrical configuration and shape of field generating and field sensing elements.
3. Train and test ANN model.
4. Experimentally verifying 2-D and 3-D MTS.
5. Applying SM modeling for system calibration.

REFERENCES

[1] *All About Gastroscopy*. (n.d). Retrieved July 28, 2008, from http://www.gihealth.com/html/test/gastroscopy.html

[2] *Colonoscopy*. (n.d). Retrieved July 28, 2008, from http://www.gihealth.com/html/test/colonoscopy.html

[3] *Wireless Capsule Endoscopy "The Camera in a Pill"*. (n.d). Retrieved July 28, 2008, from http://www.gihealth.com/html/test/given.html

[4] Given Image, Israel. (n.d). *Overview of Capsule Endoscopy*. Retrieved July 29, 2008, from http://www.givenimaging.com/en-us/Patients/Pages/pagePatient.aspx

[5] Olympus Corp, Japan. (2008). *EndoCapsule*. Retrieved July 29, 2008, from http://www.nano-tera.ch/nanoterawiki/EndoCapsule

[6] RF System Lab, Japan. (n.d). *The Next Generation Capsule Endoscope: Sayaka*. Retrieved July 29, 2008, from http://www.rfamerica.com/sayaka/index.html

[7] Intro Medic KIST, Korea. (2008). *MicoCam*. Retrieved July 29, 2008, from http://www.nano-tera.ch/nanoterawiki/MicroCam

[8] Jinshan Science & Technology, China. (2008). *OMOM*. Retrieved July 29, 2008, from http://www.nano-tera.ch/nanoterawiki/OMOM

[9] P.T. Anderson, G.L. Beauregard and C.D. Cherry, "Magnetic Tracking System," U.S. Patent 7,096,148 B2, Aug. 2006.

[10] T. Nagaoka and A. Uchiyma, "Development of a small wireless position sensor for medical capsule devices," IEEE EMBS, *International Conference*, pp. 2137-2140, Sept. 2004.

[11] W. Hou, X. Zheng, and C. Peng, "Experimental Study of Magnetic-based Localization Model for Miniature Medical Device Placed Indwelling Human Body," *IEEE Conference*, Changhai, China, pp. 1309-1312, Sept. 1-4, 2005.

[12] E. Paperno, I. Sasada, and E. Leonovich, "A new method for magnetic position and orientation tracking," *IEEE Trans. Magn.*, vol. 37, pp. 1938-1940, July 2001.

[13] E. Paperno, and P. Keisar, "Three-Dimensional Magnetic Tracking of Biaxial Sensors," *IEEE Trans. Magn.*, vol. 40, no. 3, pp. 1530-1536, May 2004.

[14] M. H. Bakr, K. Wang and M. J. Deen, "Accuracy Improvement of Magnetic Tracking Systems Using ANNs and Space Mapping Modeling," *ACES Conference*, Niagara Falls, pp. 603-608, March 2008.

[15] NDI. (2008). *NDI Electromagnetic (EM) Tracking Technology*, Retrieved July 30, 2008, from http://www.ndigital.com/medical/technology-em.php

[16] Ascension Technology Corporation. (2008). *Tracking 3D World*, Retrieved July 30, 2008, from http://www.ascension-tech.com/index.htm

[17] M. Schneider, "Measuring Position and Orientation using Magnetic Fields," U.S. Patent 6,073,043, June 2000.

[18] F. H. Rabb, "Remote Object and Orientation Locator," U.S. Patent 4,314,251, Feb. 1982.

[19] A. S. Edelstein, "Magnetic Tracking Methods and Systems," U.S. Patent 6,675,123 B1, Jan. 2004.

[20] ***NeuroModeler*** Ver. 1.5, Carleton University., 1125 Colonel By Drive, Ottawa, Canada, K1S 5B6.

[21] MatLab ver. 7.1, The MathWorks Inc, 3 Apple Hill Drive, Natick, MA 01760-2098, USA, 1994, http://www.mathworks.com/

CHAPTER 2

MAGNETIC TRACKING SYSTEMS

2.1 INTRODUCTION

Magnetic Tracking (MT) provides an inexpensive means to automatically track the positions and orientations of multiple sensors [1]. Numerous applications exist for tracking objects that generate or detect magnetic fields. All types of land vehicles, ships, and aircraft have structures and power systems capable of generating substantial magnetic signatures [2].

MT offers the advantage that the magnetic field is position dependent, which makes it possible for the MT algorithm to recover the position parameters from the magnetic field. The low frequency magnetic field penetrates the human body without attenuation or change, so MT may be continuous during a surgery. More importantly, the field is not limited by line-of-sight due to operating room personnel moving into positions that would obstruct the line-of-sight paths. This is usually required for optical tracking and ultrasonic tracking [3].

The early applications of MT systems include underground drilling systems and landing-aid systems [4]. For landing-aid systems, MT is used to determine the position and orientation of an airplane with respect to a land site for navigation purposes. For underground drill systems, it is used to determine the position and orientation of a remotely controlled underground drill with respect to the surface of the earth.

More and more MT related research has been carried out with special focus on medical applications such as image-guided surgery [3], [5], and wireless endoscopy for diagnostic purpose [6]-[9]. In the area of image-guided surgery, the magnetic sensor is usually mounted on the surgery tools. Position parameters of the surgery tools are correlated with the scanned images to help the doctors do the surgery during the entire operation. In the area of diagnoses, the position sensor can be inserted into a wireless endoscope. Images taken by the endoscope can be correlated with the position of the inserted magnetic sensor to monitor recovering status of the interest region.

2.2 BASIC CONCEPTS

A MT method utilizes magnetic fields for determining the position and orientation of a remote object relative to a reference coordinate system. The tracking system generally has three major components: field generator, field sensor and signal processing unit (Fig. 2.1).

The field generator includes a plurality of field generating elements to generate magnetic fields that are distinguishable from one another in the work area. The field

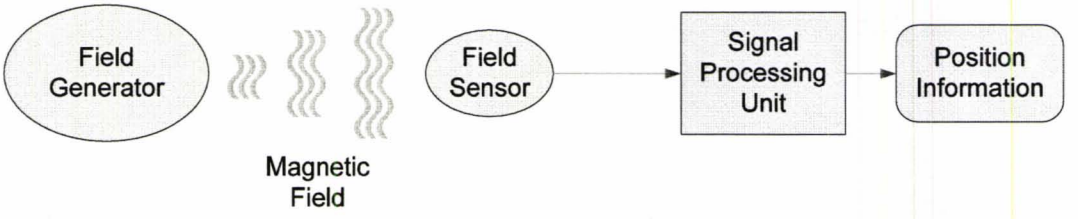

Fig 2.1: Magnetic Tracking system.

sensor includes one or more field sensing elements to sense the generated fields. The signal processing unit is used to process the outputs of the sensing elements into remote object's position and orientation relative to the generator's reference coordinate frame. The position and orientation solution is based on the magnetic field coupling between the field generator and field sensor.

2.2.1 Magnetic Tracking Assemblies

Magnetic field generating and sensing assemblies can be implemented in different ways. For example, conventional wire coils forming current loops or paths, semiconductor formed conductive lead or circuit board traces forming current paths can be arranged in an appropriate geometry to generate or sense the desired field components.

Various MT systems use circular loop coils for magnetic field generation and detection [3]-[7], [10]-[11]. One or more coils generate distinguishable magnetic fields and one or more coils detect the generated fields.

There may be a symmetry or duality between the generating and sensing elements. For example, in many cases, it is possible to have a small multi-coil array that generates a spatially distributed magnetic field and a similar or even identical array that senses the generated field [3]-[5], [11]-[15].

Small coils offer the prospect of generating a close approximation to dipole fields. On the other side, small sized coils may limit the attainable field strength or the achievable level of signal amplitude detection.

The generating and sensing coils construction may have different scales. For example, relatively large and high current coils may be used to establish magnetic field components along different axes. Smaller and localized coils are used for sensing field values [7]. For example, small coils may be attached to surgical instruments or inserted in ingestible devices such as a wireless endoscope for magnetic field sensing and position tracking.

It is necessary to characterize the magnetic field distribution (signal value) with some degree of accuracy. It is also necessary to detect the resulting field accurately. The field distribution can be determined by a combination of field modeling and empirical field mapping. The field mapping may be carried out as a calibration to correct the theoretical field distribution in the presence of interfering materials.

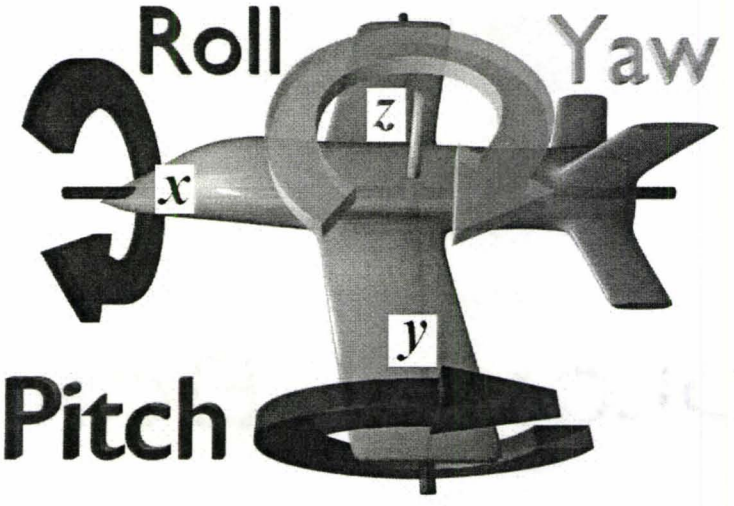

Fig 2.2: Yaw, Pitch and Roll axis definition for an airplane [16].

2.2.2 Degree of Freedom (DOF)

Depending on the number and the geometrical shape of generating and sensing coils, up to 6 degree-of-freedom (6-DOF) can be obtained. They include three position parameters and three orientation parameters. The position parameters are the x, y and z position values in the observation region. Orientation parameters are the azimuth rotation ϕ (Yaw), the elevation rotation θ (Pitch), and the roll rotation φ (Roll) as shown in Fig. 2.2.

In most cases, however, we search for only 5 unknowns. The geometrical shape of the sensing elements usually has a symmetry axis which makes the Roll rotation angle

redundant. For example, simple circular wire loops have a symmetry axis perpendicular to the surface of the circle and passing through its center point.

2.2.3 Spatial Coordinate Frame

The spatial coordinate system is generally computed for one magnetic assembly with respect to the other. Typically, one of the assemblies is fixed. The magnetic field generating coils usually define the coordinate reference frame for position and orientation measurements, either relative or absolute. Once the spatial coordinate system is defined, the movable magnetic sensing elements can be located at a given instant in time with respect to the predefined reference frame.

2.2.4 Position Parameters Determination

Given the geometry, position and orientation of the field generating coils in addition to the signals sensed in response to magnetic field generation, position and orientation of the sensing coils can be determined with respect to field generator. To estimate the position and orientation, a theoretical model describing the coupling between the generating and the sensing coils is utilized.

In general, the theoretical model includes a number of n nonlinear system equations with a number of m unknowns. The nonlinear equations define the coupling relationship between field generator and field sensor. The unknowns are the position

parameters. m=5 for 5-DOF (3 position parameters and 2 orientation angles) or m=6 for 6-DOF (3 position parameters and 3 orientation angles).

Each equation is an excitation-observation pair. The total number of system equations depends on the field generating and field sensing elements. The number of equations n is equal to the number of different field generating elements multiplied by the number of different field sensing elements. Here, "different" field generating elements or field sensing elements mean that they have different geometrical shape, position and orientation. It is independent of their excitations.

Since the obtained equations are nonlinear, it is likely that multiple solutions exist. In order to eliminate all the other unwanted possibilities, an over-determined system with more equations ($n>m$) is created.

Traditionally, position and orientation parameters can be calculated through a Parameter Extraction (PE) process [17]. PE requires a good starting point for global minimum convergence and it has to be carried out in an iterative process. This makes the tracking system relatively slow in terms of computational time. Also, the PE process, which is essentially an optimization problem, may get trapped into a local minimum, leading to incorrect extracted parameters.

2.3 MAGNETIC TRACKING IMPLEMENTATIONS

Depending on the source excitation, MT can be divided into two major categories: AC magnetic tracking and DC magnetic tracking.

2.3.1 AC Magnetic Tracking Systems

AC MT utilizes continuous sinusoidal excitation. It allows an efficient phase-locking and noise filtering of the sensor outputs. Consequently, sensor outputs can be detected accurately. On the other hand, the magnetic field can be affected by the presence of nearby conducting materials, because of the eddy current effect. The sensing elements for AC MT can be as simple as copper wired loops. Sinusoidal excitation can be applied at a number of areas.

T. Nagaoka et al. [6] developed a 5-DOF small wireless sensor for capsule endoscopy applications (Fig. 2.3). Current excitation of approximate value of 2.5 Amperes is utilized for magnetic field generation. The calibrated measured values [18] neglect the influence of the presence of nearby metallic objects. Position and orientation parameters are calculated based on Newton's method. Newton's method is a gradient-based optimization technique to solve multidimensional nonlinear equations. Its solution is starting-point dependent and the solution may be a local minimum. In addition, the solution is carried out by an iterative trial-and-error process. The position error is 2.8 ± 2.2 mm and the orientation error is 13.4 ± 20.9 deg (average $\pm$ standard deviation).

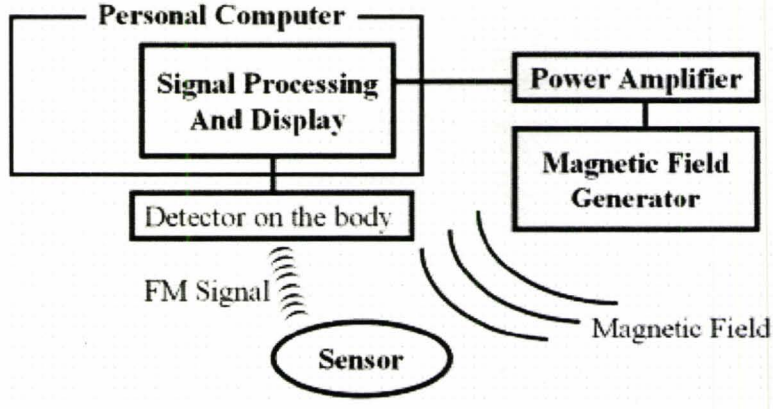

(a)

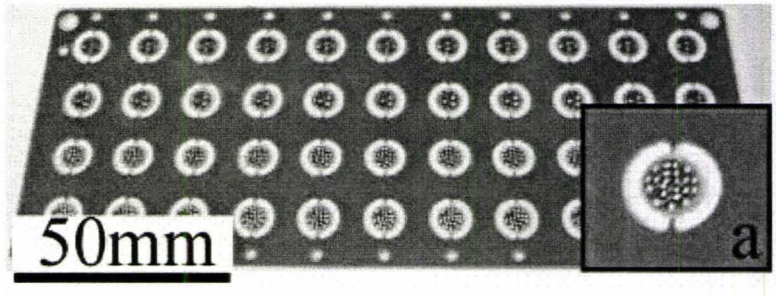

(b)

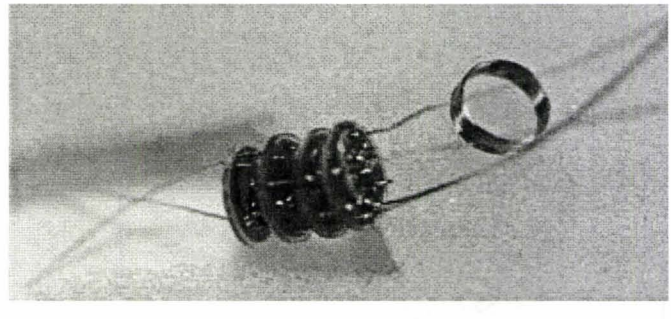

(c)

Fig 2.3: 5-DOF wireless magnetic tracking system [6]. (a) Block diagram of the sensor system. (b) PCB for the capsule shaped sensor. (c) Fabricated wireless position sensor.

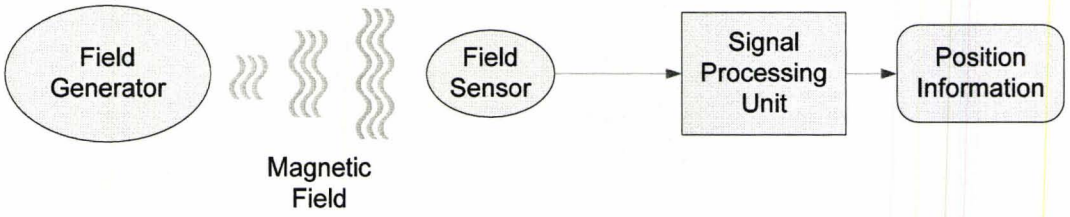

(a)

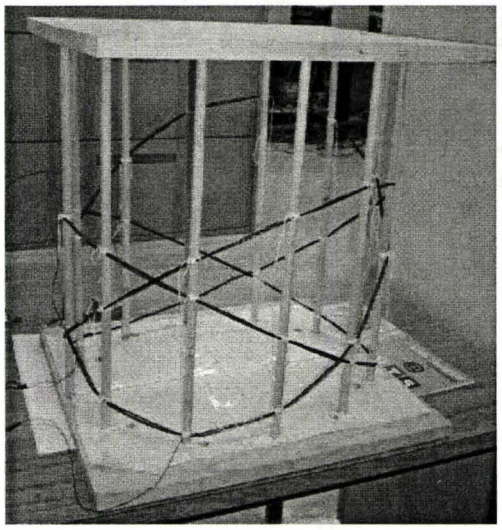

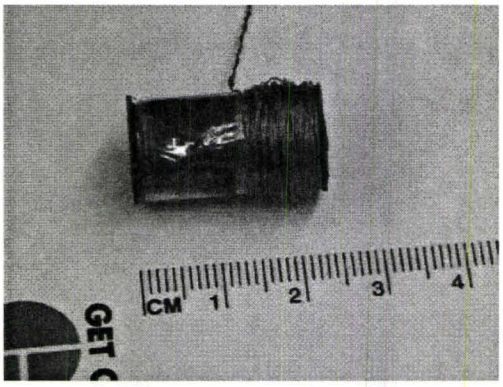

(b) (c)

Fig 2.4: 2-DOF magnetic tracking system [7]. (a) Block diagram of the tracking system (Figure is copied from Fig. 2.1). (b) Field generator. (c) Field sensor.

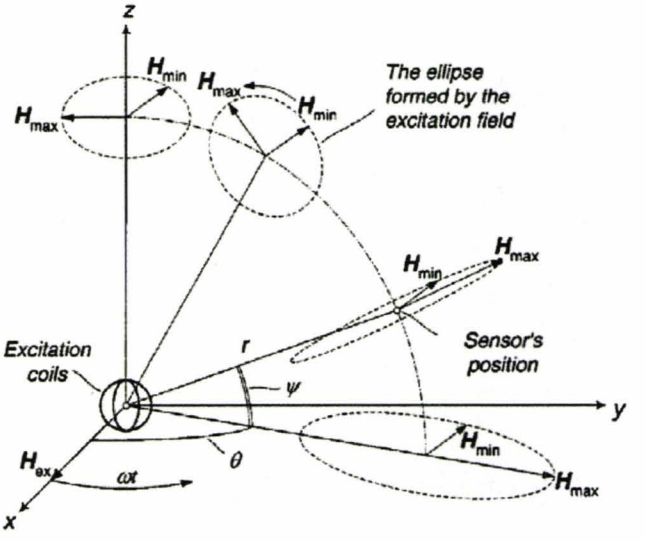

(a)

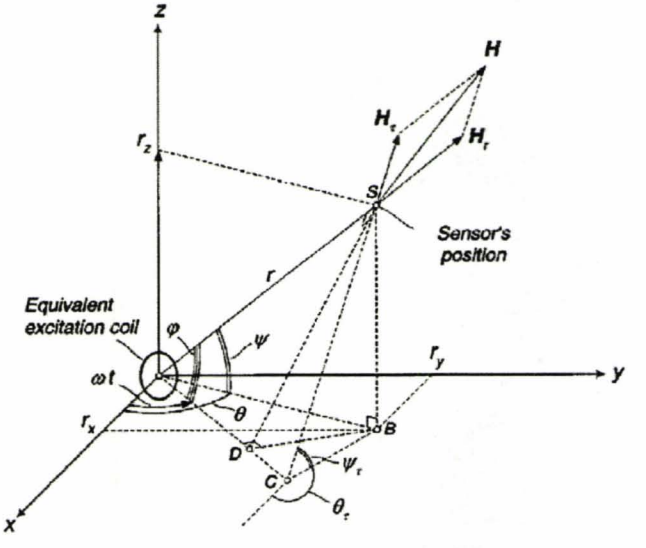

(b)

Fig 2.5: 6-DOF magnetic tracking system [10]. (a) The excitation field pattern. (b) Description of the sensor orientation.

M. H. Bakr et al. [7] implemented a 2-DOF sensor for wireless endoscopy applications (Fig. 2.4). Relatively large field generator can be mounted around the human body and small sized field sensor can be inserted into ingestible medical devices such as a wireless endoscope. 2-D position parameters are calculated by an ANN modeling the PE process. In this particular application, the iterative PE process is replaced with straight computation and signal processing time is improved significantly. This running time improvements make the real-time MT possible. In this case, the position error is 2.4 ± 1.4 mm (average $\pm$ standard deviation).

E. Paperno et al. [10] proposed a new, simple and fast 6-DOF MT method (Fig. 2.5). The field generator is a two-axis orthogonal collocated coils. A mechanically rotating magnetic dipole is used for modeling the generated field. Position and orientation parameters are determined from analytical computations. No iterative PE is involved. Preliminary experimental verifications have shown the resolution of 1 mm in a 3.6 m range for $\psi < 70$ deg. The angle ψ is defined in Fig. 2.5.

2.3.2 DC Magnetic Tracking Systems

DC MT utilizes continuous pulsed excitation. Its magnetic field is not affected by the conducting material, since there is no eddy current effect for the DC source. On the other hand, the sensor outputs are not easy for noise filtering. Environmental interference from DC sources has to be removed. The sensing elements usually are Hall-effect sensors.

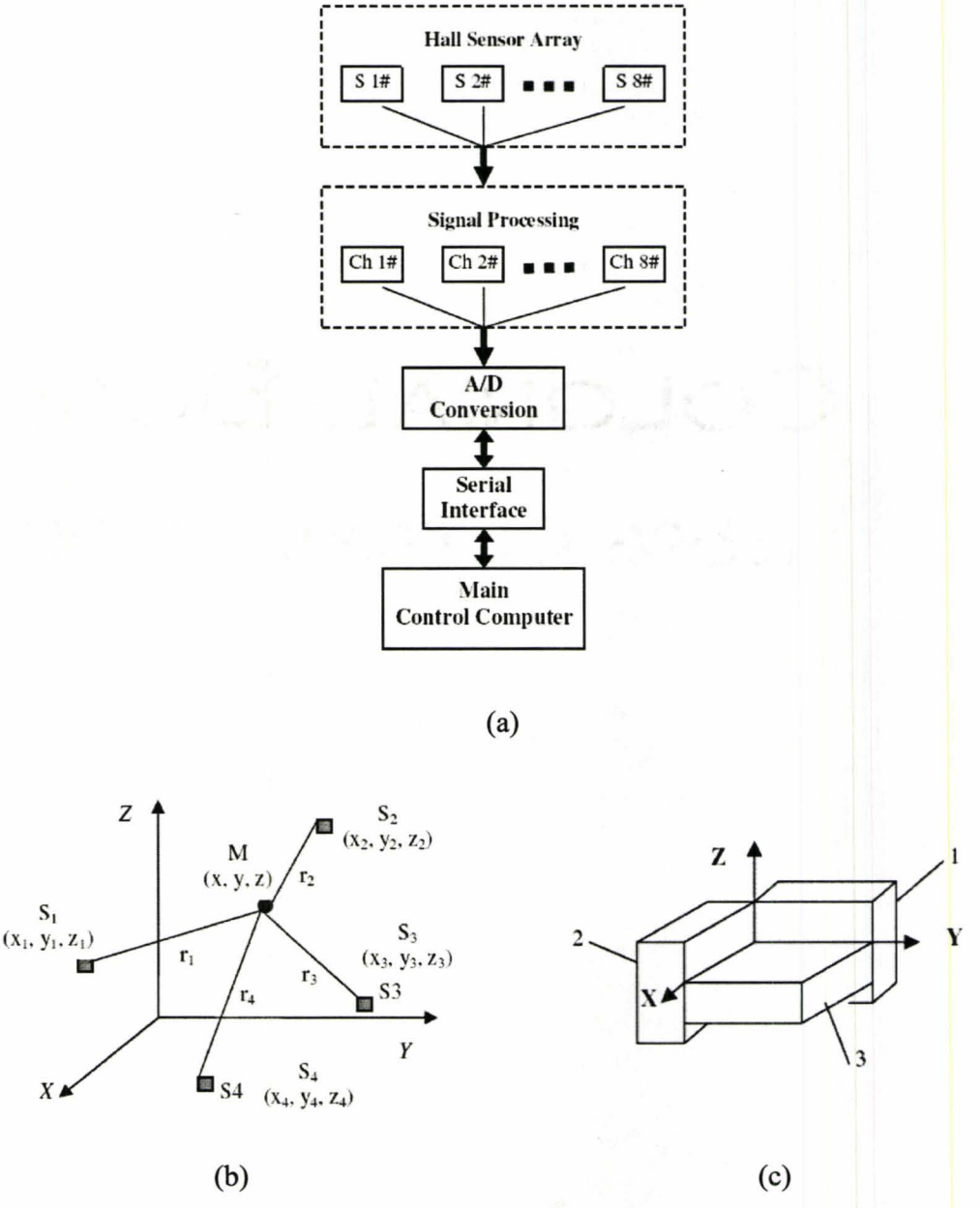

Fig 2.6: 3-DOF Magnetic Tracking system [19]. (a) Function blocks of position detecting system. (b) Magnetic based localization system. (c) Sketch of a Hall sensor for 3-dimentional magnetic field measurements.

DC pulsed excitation was reported in several applications. Hou et al. [19] designed a 3-DOF magnetic localization system utilizing a permanent magnet (Fig. 2.6). The permanent magnet can be inserted into miniature medical devices as a field generating element. Multiple Hall-effect sensors are used as field sensing elements. The magnetic position model is created by a curve fitting process using detected data. No energy is consumed for generating the magnetic field because of the utilization of permanent magnets.

E. B. Blood [20] proposed a differential MT algorithm, which can effectively remove the environmental noises from DC sources. The algorithm suggests taking additional measurements before each set of samples when no excitation is applied. In this case, the environmental magnetic signal is measured and subtracted from the total signal. Environmental interferences are removed and accurate measurements can be achieved.

2.4 MAGNETIC TRACKING FOR WIRELESS ENDOSCOPY APPLICATIONS

Our MT system approach is based on Faraday's induction law [21] (Fig. 2.7):

$$emf = -\frac{\partial \phi}{\partial t} \tag{2-1}$$

where emf is the electromotive force (induced voltage), ϕ is the magnetic flux, and t is time. We also utilize Biot-Savart's law [21] (Fig. 2.8).

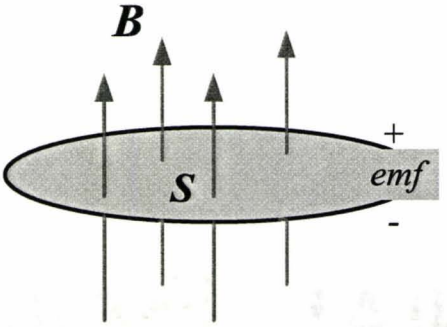

$$emf = -\frac{\partial \phi}{\partial t}$$

$$\phi = \int_{area} \boldsymbol{B} \cdot d\boldsymbol{s}$$

Fig 2.7: Faraday's induction law.

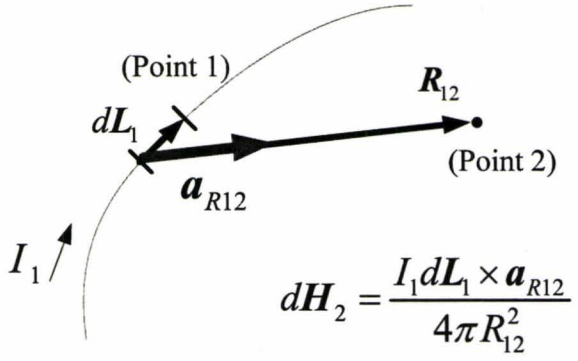

Fig 2.8: Biot-Savart's law illustration.

$$\boldsymbol{H} = \oint_c \frac{I d\boldsymbol{L} \times \boldsymbol{R}}{4\pi R^3} \tag{2-2}$$

where $\boldsymbol{H}$ is the magnetic field intensity, $\boldsymbol{R}$ is the vector from the source to the observation point, $d\boldsymbol{L}$ is the differential vector integration path, I is the current, and c is the integration path along the current source.

For a given position in 3-D space, the magnetic field generated by the source excitation can be calculated by Biot-Savart's law and the corresponding induced voltage (*emf*) can be calculated by Faraday's induction law.

An *emf* voltage can be produced by a time varying magnetic flux. The nonzero value of $\frac{\partial \phi}{\partial t}$ may result from any of the followings situations:

1. A time-varying magnetic flux density $\boldsymbol{B}$.
2. A time-varying vector area $\boldsymbol{S}$ of a closed path.
3. Relative motion between a steady magnetic flux and a closed path.
4. Any combination of the above.

For MT system, the "relative motion" is our main target. We would like to determine the relative motion in terms of position change from the induced *emf* voltage change.

2.4.1 Position and Orientation Determination

We assume a low frequency sinusoidal current excitation of the form:

$$I(t) = I_{am}\cos(2\pi ft) \tag{2-3}$$

where I_{am} is the amplitude of the AC current and f is the frequency of the AC current. By combining (2-1), (2-2) and (2-3), we have the following equations:

$$\boldsymbol{H}(t) = \cos(2\pi ft)\oint_c \frac{I_{am}d\boldsymbol{L}\times\boldsymbol{R}}{4\pi R^3} \tag{2-4}$$

$$emf = -\frac{\partial \phi}{\partial t} = -\int_s \left(\frac{\partial \boldsymbol{B}}{\partial t} \bullet d\boldsymbol{s} \right) \tag{2-5}$$

where $d\boldsymbol{s}$ is the differential vector area of the sensing element. The derivative of the magnetic field is given by

$$\frac{\partial \boldsymbol{B}}{\partial t} = -2\pi f \sin(2\pi ft)\boldsymbol{B}_{am}(x,y,z)\,. \tag{2-6}$$

Here, $\boldsymbol{B}_{am}$ is the amplitude vector of magnetic flux density which is given by (2-7)

$$\boldsymbol{B}_{am} = \mu \oint_c \frac{I_{am} d\boldsymbol{L} \times \boldsymbol{R}(x,y,z)}{4\pi R^3(x,y,z)} \tag{2-7}$$

$$emf(t) = 2\pi f \sin(2\pi ft) \int_s \boldsymbol{B}_{am}(x,y,z) \bullet d\boldsymbol{s}(\phi,\theta,\varphi) \tag{2-8}$$

$$emf_{am} = 2\pi f \int_s \boldsymbol{B}_{am}(x,y,z) \bullet d\boldsymbol{s}(\phi,\theta,\varphi) \tag{2-9}$$

where emf_{am} is the amplitude of electromotive force. In (2-9) x, y, z are the position parameters, $\phi \in [-\pi,\ \pi]$ is the azimuth rotation angle, $\theta \in [-\frac{\pi}{2},\ \frac{\pi}{2}]$ is the elevation rotation angle, and $\varphi \in [-\pi,\ \pi]$ is the roll rotation angle. In (2-9), we only have one equation with six unknowns for a general 6 DOF system. In this case, we have infinite number of solutions.

We can add more constrains and eliminate all the other unwanted possibilities by introducing multiple independent source excitations. Different source excitations lead to different integration path c in (2-4). As a result, each additional source excitation will have its own corresponding emf_{am} pair. We can have as many source excitations as

needed to satisfy our constraints. The source excitations are independent among themselves; so the resulting equations are independent as well.

Finally, position and orientation parameters can be solved from these nonlinear independent equations by a parameter extraction process (PE). To avoid the iterative trial-and-error process and the starting point dependence, we utilize ANN to carry out the computational task.

2.4.2 Sinusoidal Signal Measurement

For PE process, measurement of *emf* amplitude is required. Usually the experimental *emf* signal is very small and it is buried in noise because a strong current excitation is not allowed for safety reasons. How to measure the amplitude of an AC signal is important to us?

The amplitude of the sinusoidal signal can be measured accurately by a lock-in amplifier with phase sensitive detector (PSD) feature (Fig. 2.9). Lock-in measurements require a frequency reference. Typically, an experiment is excited at a fixed frequency using an oscillator and the lock-in amplifier detects the response from the experiment at the reference frequency.

Suppose our unknown sinusoidal signal has the following form:

$$V_{unknown}(t) = V_{sig} \sin(\omega_r t + \theta_{sig}) \qquad \text{(2-10) [22]}$$

where V_{sig} is the amplitude, ω_r is the frequency, and θ_{sig} is the phase of the unknown sinusoidal signal.

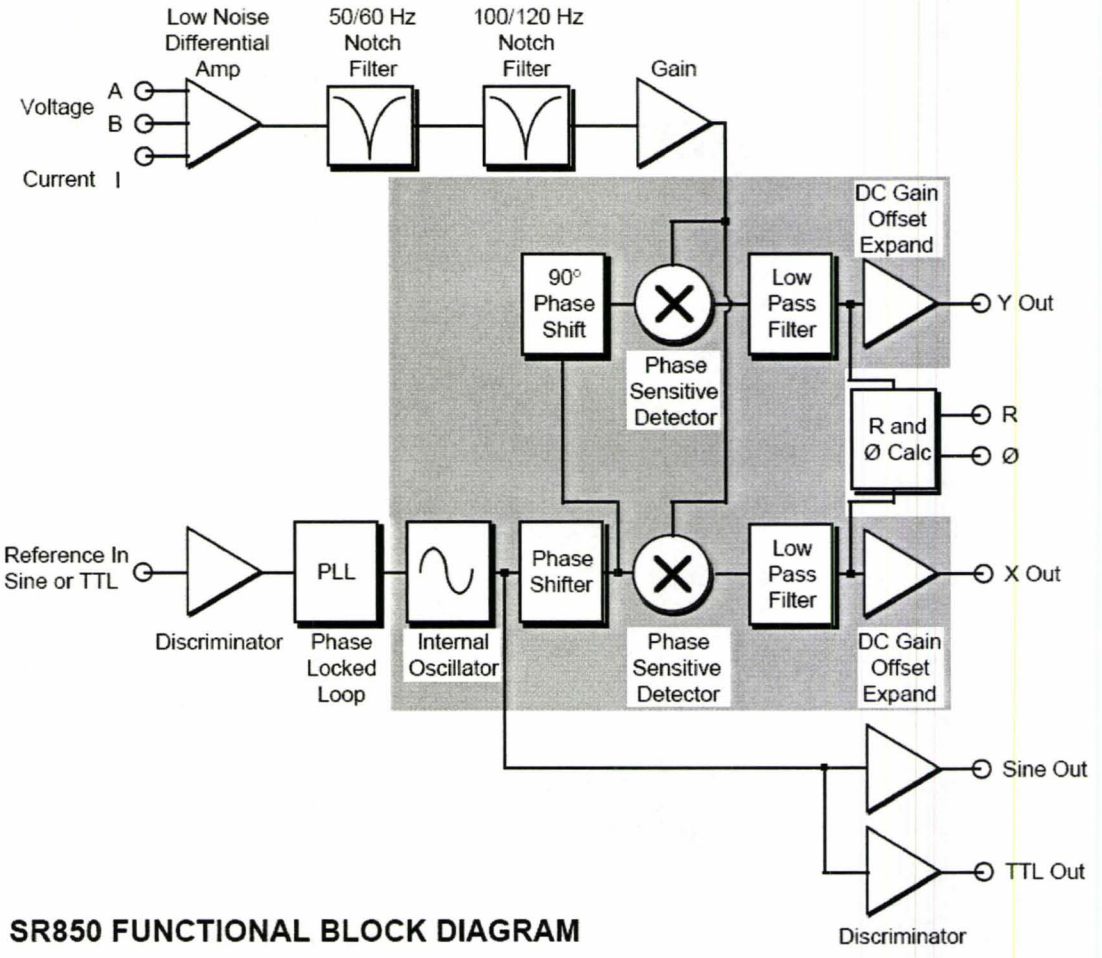

Figure 2.9: Functional block diagram of Lock-in Amplifier SR850 [22].

By providing the reference frequency, the lock-in amplifier generates its own lock-in reference sine wave of the form:

$$V_{Lock-in}(t) = V_L \sin(\omega_L t + \theta_{ref}) \qquad (2\text{-}11)\ [22]$$

The lock-in amplifier amplifies the signal and then multiplies it by the lock-in reference. The output of the PSD is simply the product of the two sine waves (2-12):

$$\begin{aligned} V_{PSD}(t) &= V_{sig}V_L \sin(\omega_r t + \theta_{sig})\sin(\omega_L t + \theta_{ref}) \\ &= \frac{1}{2}V_{sig}V_L \cos[(\omega_r - \omega_L)t + \theta_{sig} - \theta_{ref}] - \\ &\quad \frac{1}{2}V_{sig}V_L \cos[(\omega_r + \omega_L)t + \theta_{sig} + \theta_{ref}] \end{aligned} \quad \text{(2-12) [22]}$$

This output has two AC signals, one at the difference frequency $(\omega_r - \omega_L)$ and the other at the sum frequency $(\omega_r + \omega_L)$. The sum frequency component is filtered out by a low-pass filter. If $\omega_r = \omega_L$, the difference frequency component is a DC signal proportional to an unknown signal amplitude V_{sig}. In this case, the output of the PSD will be of the form:

$$V_{filtered\_PSD\_1} = \frac{1}{2}V_{sig}V_L \cos(\theta_{sig} - \theta_{ref}) \quad \text{(2-13) [22]}$$

In addition, the phase dependence can be eliminated by adding a second PSD. If we shift the phase of the lock-in reference θ_{ref} by 90 degrees, the resulting filtered PSD output will be of the form:

$$V_{filtered\_PSD\_2} = \frac{1}{2}V_{sig}V_L \sin(\theta_{sig} - \theta_{ref}) \quad \text{(2-14) [22]}$$

Combining (2-13) and (2-14), we have

$$V_{sig} = \frac{2}{V_L}\left[\left(V_{filtered\_PSD\_1}\right)^2 + \left(V_{filtered\_PSD\_2}\right)^2\right]^{\frac{1}{2}} \quad \text{(2-15)}$$

$$\theta_{sig} - \theta_{ref} = \tan^{-1}\left(\frac{V_{filtered\_PSD\_2}}{V_{filtered\_PSD\_1}}\right) \quad \text{(2-16) [22]}$$

TABLE 2.1:
MAGNETIC TRACKING TECHNIQUE COMPARISON

	DOF	signal processing	model formulation	model training
T. Nagaoka et al. [6]	5	PE trial-and-error	dipole approximation	NA
M. H. Bakr et al. [7]	2	straight computation	complete integration formula	ANN training
E. Paperno et al. [10]	6	straight computation	dipole approximation	NA
Hou et al. [19]	3	NA	dipole approximation curve fitting	NA
Our proposed method	6	straight computation	complete integration formula	ANN training

"NA" is defiend as not applicable.

In reality, lock-in reference is phased-locked to the signal reference ω_r such that $\omega_r = \omega_L$ and θ_{ref} is fixed. Noise signals at frequency ω_{noise} very close to the reference frequency ω_L will result in very slow varying AC outputs. Its attenuation depends on the bandwidth of the low-pass filter. A narrow bandwidth will remove noise sources very close to the reference frequency. Only the signal at the reference frequency results in a pure DC output and is unaffected by the low-pass filter.

Our proposed tracking technique uses complete integration formula for model development other than approximated model. In addition, we implement ANN to avoid the iterative trial-and-error process (TABLE 2.1).

2.5 CONCLUSION

In this chapter, we briefly review the basic concepts of MT systems. Such as its hardware assemblies, Degrees of Freedoms (DOF), reference coordinates frame and position an orientations parameters calculations. Various implementations are presented and its features are highlighted for comparison purposes. We present how to utilize Faraday's induction law and Biot-Savart's law to implement our own portable MT systems for wireless endoscope application. Detailed implementation for particular cases will be introduced in the following chapters.

REFERENCES

[1] J. S. Day, and G. A. Dumas, "Use of a MT device to determine lumbosacral moments during asymmetric lifting," *Journal of Biomechanics*, vol. 31, pp. 119-119(1), 1998.

[2] A. S. Edelstein, "MT Methods and Systems," U.S. Patent 6,675,123 B1, Jan. 2004.

[3] P. T. Anderson, G. L. Beauregard and C.D. Cherry, "MT System," U.S. Patent 7,096,148 B2, Aug. 2006.

[4] F. H. Rabb, "Remote Object and Orientation Locator," U.S. Patent 4,314,251, Feb. 1982

[5] M. Schneider, "Measuring Position and Orientation using Magnetic Fields," U.S. Patent 6,073,043, June. 2000

[6] T. Nagaoka and A. Uchiyma, "Development of a small wireless position sensor for medical capsule devices," IEEE EMBS, *International Conference*, pp. 2137-2140, Sept. 2004

[7] M. H. Bakr, K. Wang and M. J. Deen, "Accuracy Improvement of MT Systems Using ANNs and Space Mapping Modeling," *ACES Conference*, Niagara Falls, pp. 603-608, March 2008.

[8] NDI. (2008). *NDI Electromagnetic (EM) Tracking Technology*, Retrieved July 30, 2008, from http://www.ndigital.com/medical/technology-em.php

[9] Ascension Technology Corporation. (2008). *Tracking 3D World*, Retrieved July 30, 2008, from http://www.ascension-tech.com/index.htm

[10] E. Paperno, I. Sasada, and E. Leonovich, "A new method for magnetic position and orientation tracking," *IEEE Trans. Magn.*, vol. 37, pp. 1938-1940, July 2001.

[11] E. Paperno, and P. Keisar, "Three-Dimensional MT of Biaxial Sensors," *IEEE Trans. Magn.*, vol. 40, no. 3, pp. 1530-1536, May 2004.

[12] P. T. Anderson, G. L. Beauregard and C.D. Cherry, "MT System," U.S. Patent 6,774,624 B2, Aug. 2004.

[13] P. T. Anderson, G. L. Beauregard and C.D. Cherry, "MT System," U.S. Patent 0,184,285 A1, Oct. 2003.

[14] P. T. Anderson, G. L. Beauregard and C.D. Cherry, "MT System," U.S. Patent 0,165,297 A1, Jul. 2005.

[15] P. T. Anderson, G. L. Beauregard and C.D. Cherry, "MT System," U.S. Patent 6,980,921 B2, Dec. 2005.

[16] WIKIPEDIA, The Free Encyclopedia. (2008). *Flight dynamics*. Retrieved Aug 7, 2008, from http://en.wikipedia.org/wiki/Flight_dynamics

[17] M.H. Bakr, J.W. Bandler and N. Georgieva, "An aggressive approach to parameter extraction," *IEEE MTT-S Int. Microwave Symp. Dig.* (Anaheim, CA), pp. 261-264, 1999.

[18] J. S. Day, D. J. Murdoch and G. A. Dumas, "Calibration of position and angular data from a MT device," Journal of Biomechanics, vol. 33-8, pp.1039-1045, 2000.

[19] W. Hou, X. Zheng, and C. Peng, "Experimental Study of Magnetic-based Localization Model for Miniature Medical Device Placed Indwelling Human Body," *IEEE Conference*, Changhai, China, pp. 1309-1312, Sept. 1-4, 2005.

[20] E. B. Blood, "Device for Quantitatively Measuring the Relative Position and Orientation of Two Bodies in the Presence of Metals Utilizing Direct Current Magnetic Fields," U.S. Patent 4,849,692, Jul. 1989.

[21] W. H. Hayt and J.A. Buck, *Engineering Electromagnetics (6^{th} Ed)*. McGraw Hill, 2001.

[22] *DSP Lock-In Amplifier model SR850*, Stanford Research Systems, 1999.

CHAPTER 3

ARTIFICIAL NEURAL NETWORKS (ANN)

3.1 INTRODUCTION

Artificial Neural Networks (ANN) have emerged as a powerful technique for modeling general input and output relationships. It has been used in the area of remote sensing [1], biomedical [2], pattern recognition [3] and manufacturing [4]. Recently, ANN has been used more and more in the area of RF and microwave design [5]. They have been also used in different microwave applications such as automatic impedance matching [6] and microwave circuit analysis and optimization [7]-[8].

ANN models are more accurate than polynomial region models [9]-[10]. They also allow more dimensions than look-up table models [11] and also allow multiple outputs for a single model. ANN models are developed by utilizing sufficient training data (e.g. EM simulations or measurements). This data helps the ANN learn the underlying input/output mapping.

Several valuable features are offered by ANN [12]. First, no prior knowledge about input/output relationship is required for model development. Unknown relationships are inferred from the data provided for training. Therefore, inside ANN, the fitting function is represented by the network and does not have to be explicitly defined. Second, ANN can be generalized. They can respond correctly to new data that has not been used for model development. Third, ANN has the ability to model highly nonlinear input/output mappings. It has been shown that ANN are capable of forming an arbitrarily close approximation to any continuous nonlinear mapping [13].

ANN provides a general methodology for accurate and efficient EM-based model development in areas such as RF/microwave circuits, antennas and systems. These models are capable of providing similar accuracy to full-wave EM simulation and lead to accurate and efficient CAD.

3.2 ANN STRUCTURES

A neural network has at least two physical components: the processing elements and the connections between them. The processing elements are called neurons and the connections are called links.

Each neuron receives stimulus from neighbouring neurons connected to it, processes the information, and then produces the output. Neurons that receive stimuli from outside the networks are called the input neurons. Neurons whose outputs that are used externally are called the output neurons. Neurons that receive stimuli from other

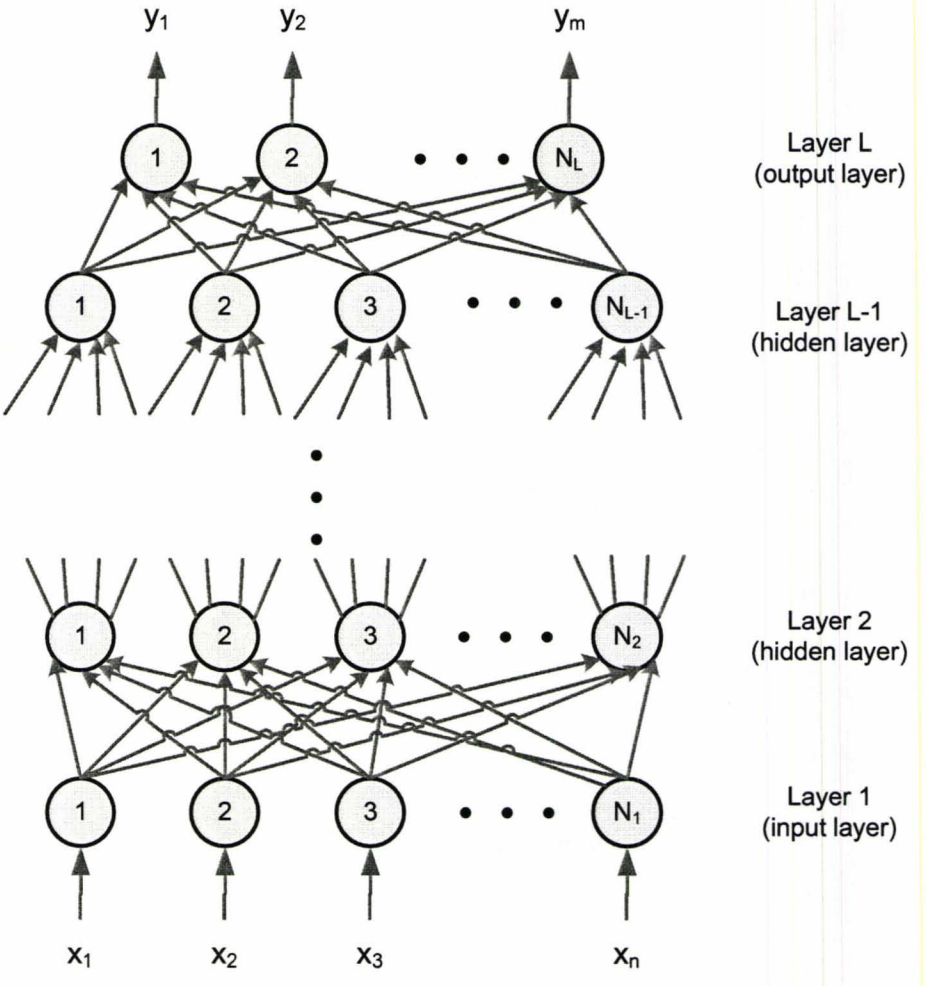

Fig 3.1: The structure of a Multilayer Perceptrons (MLP) [14].

neurons and whose outputs are stimuli for other neurons are called hidden neurons. The most popular type of ANN is Multilayer Perceptrons (MLP) shown in Fig. 3.1.

In a MLP, each link has a weight parameter and each neuron has its own activation function. The weight parameters and the user predefined activation functions are the internal model parameters for ANN models.

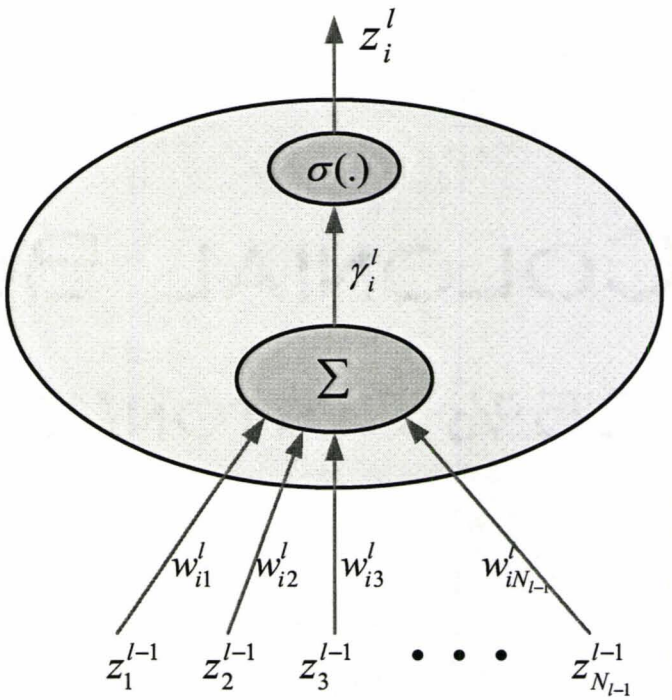

Fig 3.2: Information Processing by a Neuron [14].

3.3 INFORMATION PROCESSING

In a neural network, each neuron receives and processes inputs from other neurons with the exception of neurons at the input layer. The processed information is available at the neurons of the output layer. Consider one hidden neuron for example in Fig. 3.2. the quantities z_1^{l-1}, z_2^{l-1}, …, $z_{N_{l-1}}^{l-1}$ are the neurons output responses at the previous hidden layer with index (l-1). w_{i1}^l, w_{i2}^l, … , $w_{iN_{l-1}}^l$ are the weight parameters connecting current neuron i at layer l with all the neurons at previous hidden layer l-1. z_i^l is the output

response of current neuron i at layer l. This figure illustrates how the information is processed. Each input is first multiplied by its corresponding weight parameter, the sum of products (3-1) are passed through the current neuron activation function $\sigma(.)$ (3-2):

$$\gamma_i^l = \sum_{j=1}^{N_{l-1}} w_{ij}^l z_j^{l-1} \tag{3-1}$$

$$z_i^l = \sigma\left(\sum_{j=1}^{N_{l-1}} w_{ij}^l z_j^{l-1}\right) \tag{3-2}$$

3.3.1 Universal Approximation Theorem

To guarantee the existence of an ANN model for any particular application, the Universal Approximation Theorem has been proved [13], [15]. This theorem states that with finite number of hidden neurons, there always exists a 3-layer ANN that can approximate an arbitrary nonlinear, continuous, and multidimensional function with any desired accuracy. This theorem, however, does not specify the number of hidden neurons for a given problem. The precise number of hidden neurons required is still an open question.

3.3.2 Activation Functions

All the activation functions have to be bounded, continuous, monotonic, and continuously differentiable with respect to the weights $\boldsymbol{w}$ for optimization purposes.

The most commonly used activation function is the sigmoid function (Fig. 3.3). Other possible activations are the arc-tangent function (Fig. 3.4) and the hyperbolic-

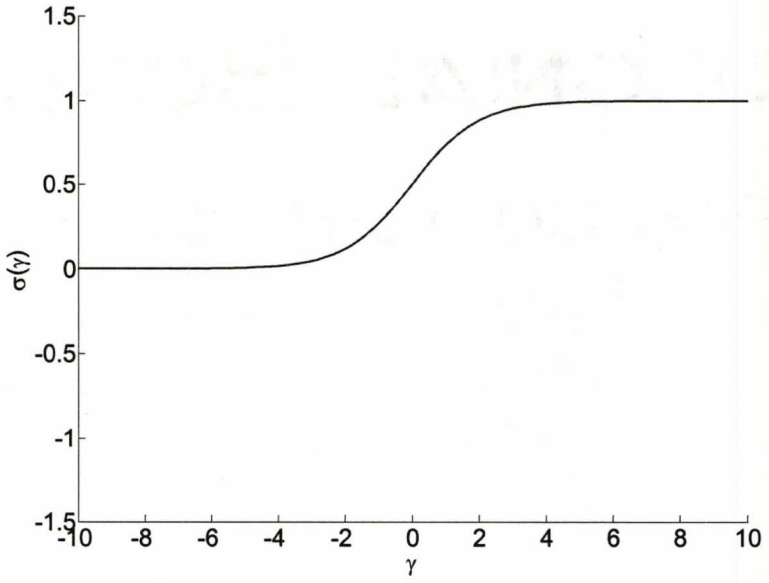

Fig 3.3: Sigmoid activation function. [14].

tangent function (Fig. 3.5). The mathematical expressions of these activation functions are given by:

$$\text{Sigmoid function}: \quad \sigma(\gamma) = \frac{1}{1+e^{-\gamma}} \tag{3-3}$$

$$\text{Arc-tangent function}: \quad \sigma(\gamma) = \left(\frac{2}{\pi}\right)\arctan(\gamma) \tag{3-4}$$

$$\text{Hyperbolic-tangent function}: \quad \sigma(\gamma) = \frac{e^{\gamma} - e^{-\gamma}}{e^{\gamma} + e^{-\gamma}} \tag{3-5}$$

After the activation functions are chosen, the weight parameters $\boldsymbol{w}$ have to be optimized to model the desired input/output relationship.

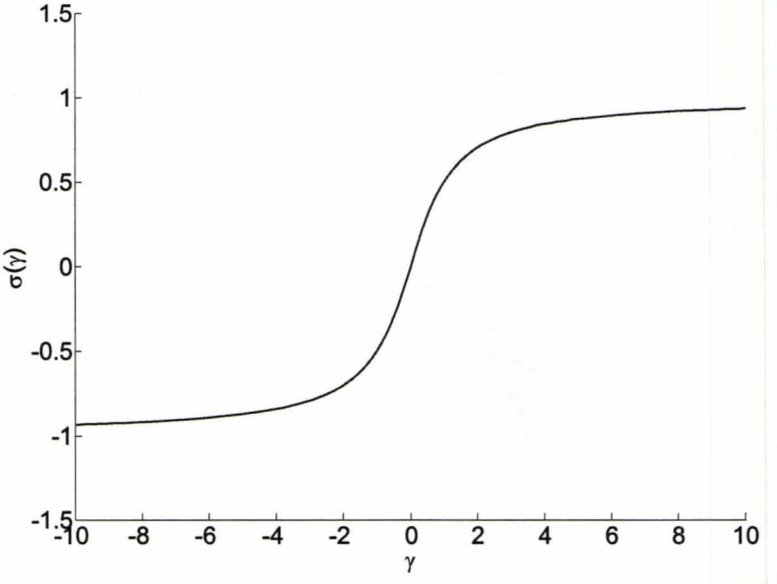

Fig 3.4: Arc-tangent activation function [14].

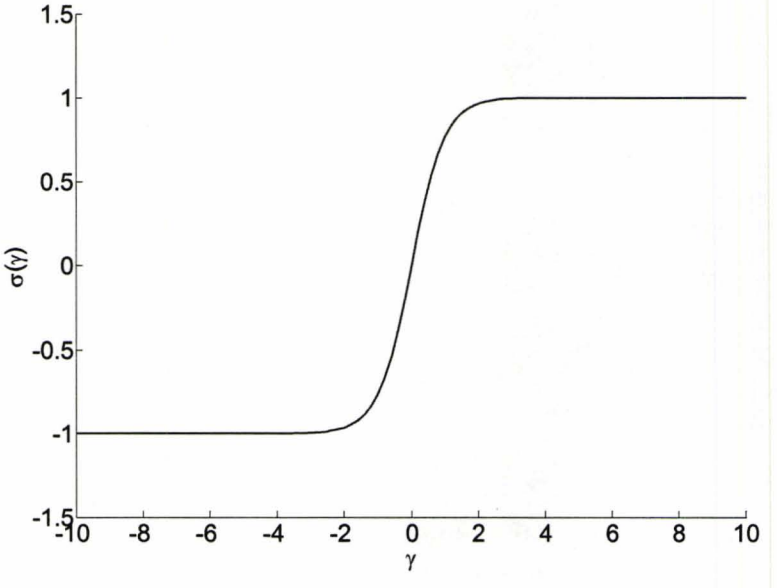

Fig 3.5: Hyperbolic-tangent activation function [14].

3.4 ANN MODEL DEVELOPMENT

The theoretical model can be expressed as:

$$\boldsymbol{d} = \boldsymbol{f}(\boldsymbol{x}) \tag{3-6}$$

where $\boldsymbol{x}$ is the vector of input parameters and $\boldsymbol{d}$ is the vector of output responses. The relation $\boldsymbol{f}$ can be highly nonlinear and multidimensional. The ANN model can be defined as:

$$\boldsymbol{y} = \boldsymbol{y}(\boldsymbol{x}, \boldsymbol{w}) \tag{3-7}$$

where $\boldsymbol{x}$ is the design parameters, $\boldsymbol{y}$ is the vector of the ANN output responses, and $\boldsymbol{w}$ is the vector of unknown weight parameters of the neural network.

The objective in ANN development is to find the optimal weight parameters $\boldsymbol{w}$ of neural networks so that $\boldsymbol{y} = \boldsymbol{y}(\boldsymbol{x}, \boldsymbol{w})$ closely approximates the original problem $\boldsymbol{d} = \boldsymbol{f}(\boldsymbol{x})$. This process is called ANN training (see Fig. 3.6).

3.4.1 Data Generation

The first step in ANN development is to collect the data for training and testing the ANN performance. The collected data is the input $\boldsymbol{x}_k$ and the corresponding desired output $\boldsymbol{d}_k$ pairs defined in (3-6) in the region of interest of input parameter space $[\boldsymbol{x}_{min}, \boldsymbol{x}_{max}]$.

Once the range of the input parameters is fixed, we need to choose the sampling strategy. Many strategies are used for sampling the input parameter space such as uniform

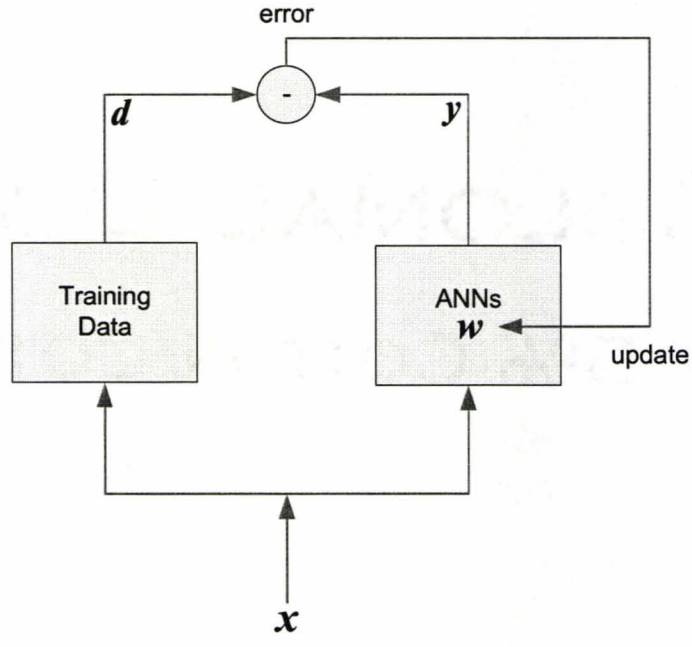

Fig 3.6: ANN training process [14].

gird distribution, nonuniform distribution, star distribution, and random distribution [16].

The training data set is used for weight parameters $\boldsymbol{w}$ optimization in the ANN development stage. The number of samples should be sufficient enough for the ANN to recognize the implicit input/output relationship.

Once the ANN is trained, the accuracy of the obtained model should be tested to verify whether the ANN model can respond accurately to the inputs which it never "saw" before. The testing data set is used for this purpose only and it is not involved in the optimal weights determination. Usually, the testing samples cover the same region as the training samples to check the ANN's "intuitive interpolation".

3.4.2 The ANN Training

The weight parameters $\boldsymbol{w}$ optimization process is called training. During the training process, ANN performance is evaluated by the difference between the desired output $\boldsymbol{d}_k$ and the ANN response $\boldsymbol{y}_k$ for all the training data. The difference is also called training error :

$$E_{Tr} = \frac{1}{2}\sum_{k\in Tr}\sum_{j=1}^{m}\left[y_j(\boldsymbol{x}_k, \boldsymbol{w}) - d_{jk}\right]^2 \tag{3-8}$$

where E_{Tr} is the total training error, m is the number of output responses. Here T_r is the training data index, d_{jk} is the jth element of $\boldsymbol{d}_k$, and $y_j(\boldsymbol{x}_k, \boldsymbol{w})$ is the jth ANN output approximating d_{jk}.

After initializing the weight parameters $\boldsymbol{w}$ with some small random numbers, $\boldsymbol{w}$ is updated along the negative gradient of E_{Tr} until E_{Tr} becomes small enough. A one update step is given by

$$\boldsymbol{w}_{next} = \boldsymbol{w}_{now} - \eta\frac{\partial E_{Tr}}{\partial \boldsymbol{w}} \tag{3-9}$$

where η is called the learning rate of the ANN.

Training methods based on gradient information $\frac{\partial E_{Tr}}{\partial \boldsymbol{w}}$ as in (3-9) are called gradient-based techniques. Gradient-based training techniques include Conjugate-Gradient [17] training method, Quasi-Newton [18]-[19] training method, Levenberg-

Marquardt [20]-[21], and Gauss-Newton [20] training methods. Non gradient-based training techniques are also used, such as the Simplex method [22].

3.4.3 Over-Learning and Under-Learning

The normalized training error is given by

$$\hat{E}_{Tr}(\boldsymbol{w}) = \frac{1}{size(T_r) \times m} \sum_{k \in Tr} \sum_{j=1}^{m} \left[\left| \frac{y_j(\boldsymbol{x}_k, \boldsymbol{w}) - d_{jk}}{d_{max,j} - d_{min,j}} \right|^p \right]^{\frac{1}{p}} \tag{3-10}$$

Over-learning (3-11) is when the training error $\hat{E}_{Tr}$ is small and testing error is large. This is the case where the ANN "memorizes" the training data but cannot generalize well enough. The reasons could be that too many hidden neurons are used or the training data is insufficient. Too many hidden neurons give the ANN too much degree of freedom in input/output relationship. We need in this case to remove some hidden neurons or add more training samples.

$$\begin{cases} \hat{E}_{Tr} \approx \mathbf{0} \\ \hat{E}_{Te} \gg \hat{E}_{Tr} \end{cases} \tag{3-11}$$

Under-learning (3-12) is when training and testing errors are both large. This is the case when the ANN cannot even learn from the training data. The reason could be insufficient hidden neurons or that training process stops at a local minimum. In this case, we need to add more neurons or perturb the current weight parameters $\boldsymbol{w}$.

$$\begin{cases} \hat{E}_{Tr} \gg \mathbf{0} \\ \hat{E}_{Te} \gg \mathbf{0} \end{cases} \tag{3-12}$$

Good learning is when both training and testing error are small and close to each other. In this case, the ANN learns from the training data and generalizes well:

$$\hat{E}_{Tr} \approx \hat{E}_{Te} \approx \mathbf{0} \tag{3-13}$$

3.5 AUTOMATED ANN MODEL GENERATOR

NeuroModeler V1.5 [23] is a user-friendly software which can generate ANN model automatically. The program is developed by Q. J. Zhang and F. Wang with contributions from members of Prof. Zhang's research team in Carleton University.

NeuroModeler is a tool set for ANN model development for circuit and systems design. The generated models are generic, multidimensional and highly nonlinear. These models are much enhanced in terms of speed, accuracy, generality and adaptability compared to conventional modeling methods. ***NeuroModeler*** provides a new type of solutions for modeling problems in various engineering tasks.

There are only 4 major steps involved to train the ANN and generate a user specific ANN model:

Step 1 Get the training and testing data files ready for ANN.

Step 2 Define ANN model from the main menu (Fig. 3.7) by pressing <New Neural Model> (Fig. 3.8). Select ANN structure, number of hidden layers, number of input and output.

Step 3 Train the ANN by pressing <Train Neural Model> from main menu (Fig. 3.7). Various training methods are available (Fig. 3.9). After the training data set is selected, ANN training can be started. Training error will be shown when the training process is done.

Step 4 Testing the ANN model by pressing <Test Neural Model> from main menu (Fig. 3.7). After the testing data set is selected, the ANN testing process can be started (Fig. 3.10). Average and worst case error will be shown when the computation is finished. If the error is too large, go back to *Step 3* for further training.

The 4 major steps above are the minimum user interactions in ANN model generation. Other than the default setting, advanced users can select optional settings such as activation functions, ANN structures, training methods and its corresponding training parameters. More advanced users can use ***NeuroModeler***'s simulator drivers for automatically generating data sets with different simulation tools.

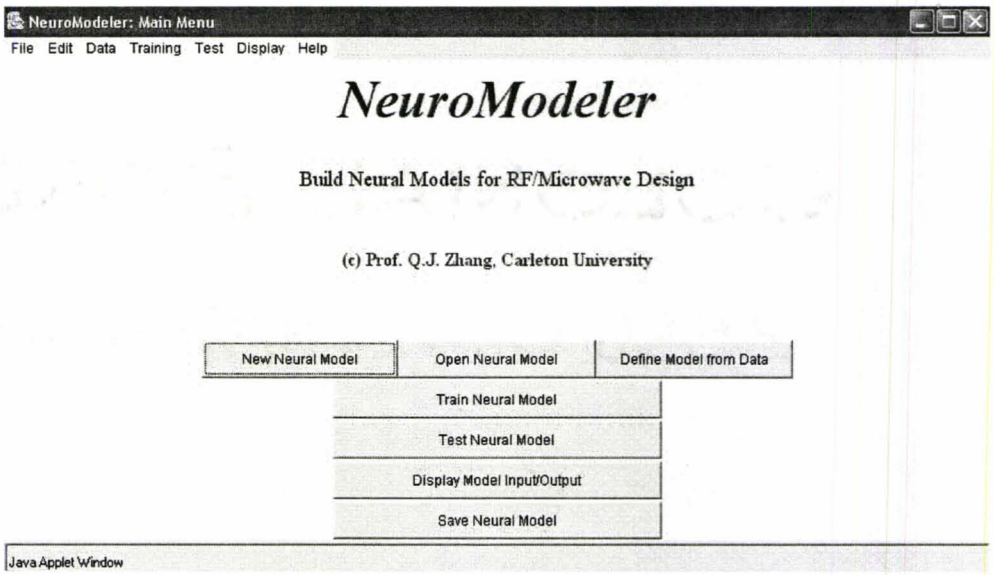

Fig 3.7: *NeuroModel* main menu.

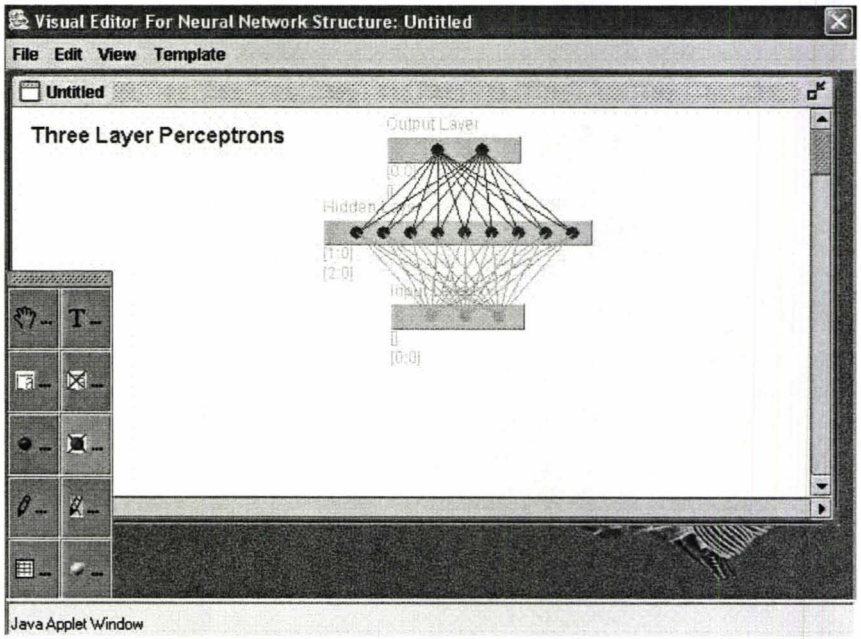

Fig 3.8: ANN model setup.

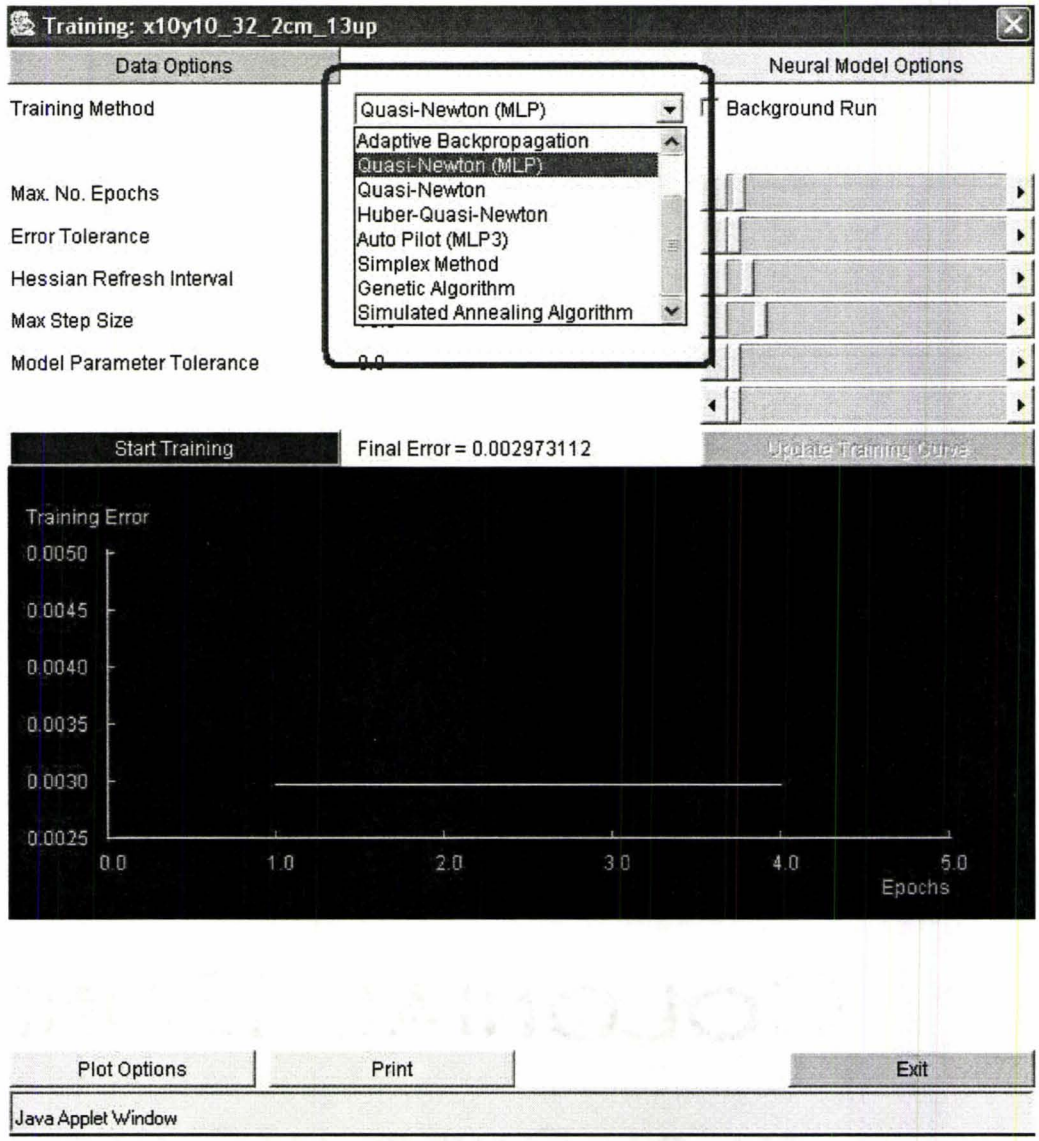

Fig 3.9: *NeuroModel* training methods selection.

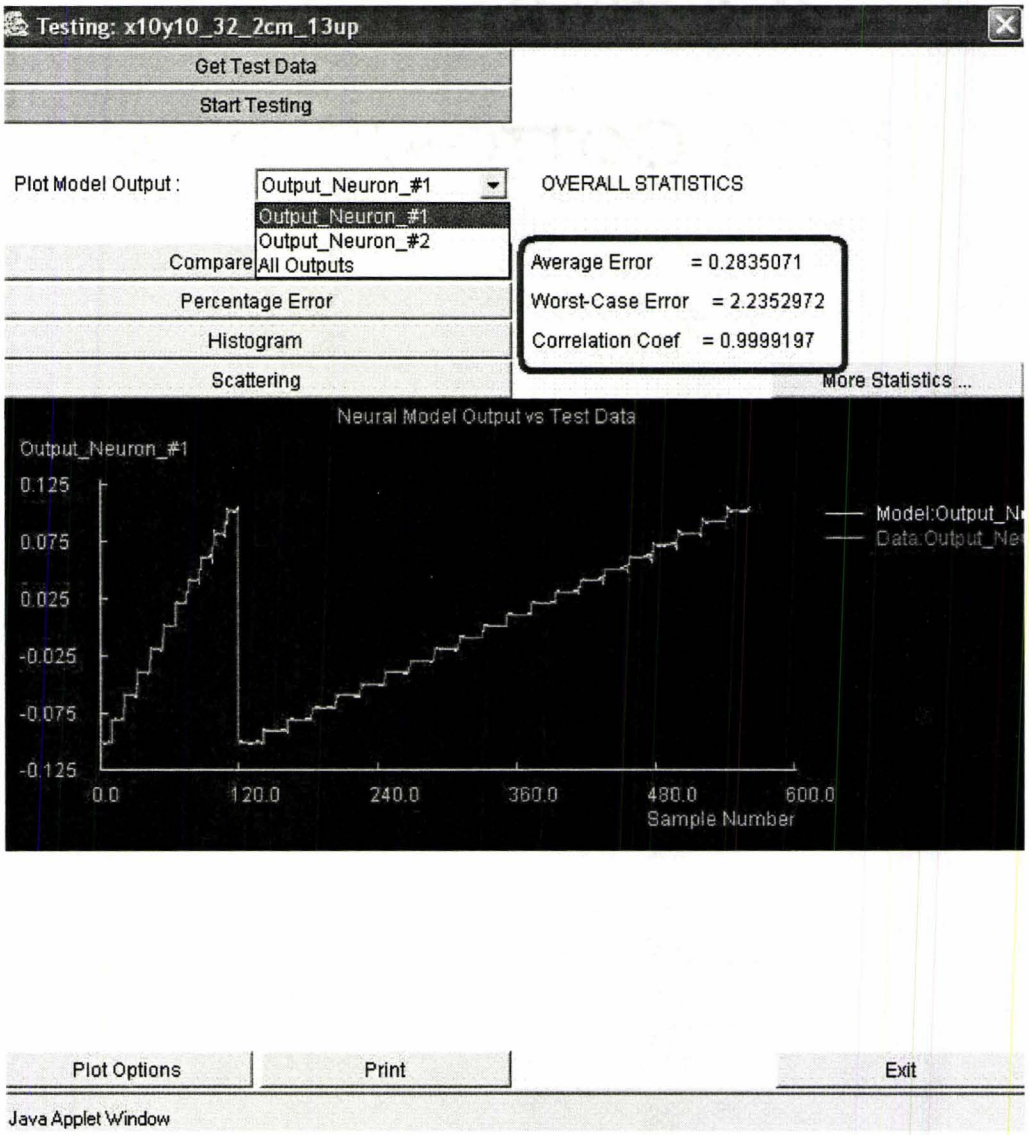

Fig 3.10: *NeuroModel* testing statistics.

3.6 CONCLUSIONS

In this chapter, we briefly reviewed the concept of Artificial Neural Networks (ANN), including their structures, information propagation and the development of ANN models. The existence of accurate ANN model for any complex problems is guaranteed according to the Universal Approximation Theorem [13], [15]. The mathematical formulation for ANN training process is presented. ***NeuroModeler*** [23] is introduced for automated ANN model generation.

REFERENCES

[1] K. Goita, Gonzalez-Rubio, R., Benie, G. B. Royer, A., "Literature Review of Artificial Neural Networks and Knowledge Based Systems for Image Analysis and Interpretation of Data in Remote Sensing," *Canadian Journal of Electrical and Computer Engineering*, vol. 19, no. 2, pp. 53-61, 1994.

[2] T. Alvager, T. J. Smith, and F. Vijai, "The Use of Artificial Neural Networks in Biomedical Technologies: An Introduction," *Biomedical Instrumentation and Technology*, vol. 28, no. 4, pp. 315-322, 1994.

[3] Y. G. Smetanin, "Neural Networks as Systems for Pattern Recognition: A Review," *Pattern Recognition and Image Analysis*, vol. 5, no. 2, pp. 254-293, 1995.

[4] R. Rajagopalan, and P. Rajagopalan, "Applications of Neural Networks in Manufacturing." *Proceeding of the Twenty-ninth Hawaii International Conference on System Sciences*, vol. 2, pp. 447-453, 1996.

[5] Q. J. Zhang, and G. L. Creech (Guest Editors), *International Journal of RF and Microwave Computer-Aided Engineering*, Special Issue on Applications of Artificial Neural Networks to RF and Microwave Design, vol. 9, NY: Wiley, 1999.

[6] M. Vai, and S. Prasad., "Automatic Impedance Matching with a Neural Network," *IEEE Microwave and Guided Wave Letters*, vol. 3, no. 10, Oct. pp. 353-354, 1993.

[7] A. H. Zaabab, Q. J. Zhang, and M. Nakhla, "Analysis and Optimization of Microwave Circuits and Devices Using Neural Network Models," *MTT-S Int. Microwave Symp. Dig.*, pp. 393-396, 1994.

[8] V. B. Litovski, J. I. Radjenovic, Z. M. Mrcarica, and S. Lj. Milenkovic, "MOS Transistor Modeling Using Neural Network," *Electronics Letters*, vol. 28, no. 18, pp. 1766-1768, 1992.

[9] G. R. Finnie, G. E. Wittig, and J. M. Desharnais. "A Comparison of Software Effort Estimation Techniques: Using Function Points with Neural Nwteorks, Case-Base Reasoning, and Regression Models," *Journal of Systems and Software*, vol. 39, no. 3, pp. 281-290, Mar. 1997.

[10] A. E. Smith, and A. K. Mason, "Cost Estimation Predictive Modeling: Regression versus Neural Network," Engineering Economist, vol. 42, no. 2, pp. 137-160, Feb. 1997.

[11] Q. J. Zhang, F. Wang, and M. S. Nakhla, "Optimization of High-Speed VLSI Interconnects: A Review," *Int. J. of Microwave and Millimeter Wave CAE*, vol. &, pp. 83-107, 1997.

[12] C. M. Bishop, *Neural Networks for Patern Recognition*. New York: Oxford University Press Inc., 1996.

[13] K. Hornik, M. Stinchcombe, and H. White, "Multi-layered Feed-Forward Neural Networks are Universal Approximations," *Neural Networks*, vol. 2, 1990, pp. 259-266.

[14] Q. J. Zhang, K. C. Gupta and V. K. Devabhaktuni, "Artificial neural networks for RF and microwave design: from theory to practice," *IEEE Trans. Microwave Theory Tech.*, vol. 51, pp. 1339-1350, March 2003.

[15] G. Cybenko, "Approximation by Superpositions of a Sigmoidal Function," *Math. Control Signals Systems*, vol. 2, pp. 303-314, 1989.

[16] Q. J. Zhang, K. C. Gupta. *Neural Networks: For RF and Microwave Design*. Boston: Artech House, 2000.

[17] M. F. Moller, "A Scaled Conjugate Gradient Algorithm for Fast Supervised Learning," *Neural Networks*, vol. 6, pp. 525-533, 1993.

[18] T. R. Cuthbert, "Quasi-Newton Methods and Constrains," In *Optimization using Personal Computers*, NY: John Wiley & Sons, pp. 234-314, 1987.

[19] C. G. Broyden, "Quasi-Newton Methods and their Application to Function Minimization," *Math. Comp.* Vol. 21, pp. 368-381, 1967.

[20] A. J. Shepherd, "Second-Order Optimization Methods," In *Second-Order Methods for Neural Networks*, London: Springer-Verlag, pp. 43-72, 1997.

[21] S. Kollias, and D. Anastassiou, "An Adaptive Least Squares Algorithm for the Efficient Training of Artificial Neural Networks," *IEEE Trans. Circuit and Systems*, vol. 36, pp. 1092-1101, 1989.

[22] J. A. Nelder, and R. Mead, "A Simplex Method for Function Minimization," *Computer Journal*, vol. 7, pp. 308-313, 1965.

[23] ***NeuroModeler*** Ver. 1.5, Carleton University., 1125 Colonel By Drive, Ottawa, Canada, K1S 5B6.

[24] S. Haykin. *Neural Networks: A Comprehensive Foundation (2nd Ed)*. Prentice Hall, 1999.

CHAPTER 4

SPACE MAPPING MODELLING AND OPTIMIZATION

4.1 INTRODUCTION

Engineers have been using optimization techniques with Computer Aided Design (CAD) in the area of RF and Microwave design for decades [1]. The objective is to determine the set of optimal design parameters that satisfies the design specification.

Traditional gradient-based optimization techniques [2]-[3] utilize simulated responses and available derivatives in determining optimal design parameters values. Circuit-theoretic-based Computer Aided Design (CAD) tools are fast in terms of computational time. The available analytical solutions and/or exact derivatives accelerate the optimization convergence. Electromagnetic (EM) simulators have to be exploited in the optimization process. The higher the accuracy of simulation, the more "expensive" direct optimization is expected to be. For complex problems, the cost is impractical in terms of simulation time and memory requirements. Alternative design schemes

combining the accuracy of EM solvers and the speed of circuit-theory based simulators are highly desirable.

Space Mapping (SM) approach, originally introduced by Bandler *et al.* [4]-[5] in 1994, addresses the optimization problem of time intensive models. It is a fundamental new theory for optimization utilizing parameter transformation. Its fundamental concept is to utilize a "coarse" model in the optimization process while calling the time intensive "fine" model only sparingly.

SM has been proved to be a powerful concept in modeling and optimization. Many variations of the SM approach are developed [6]-[11]. Its applications include antenna design [12]-[13], RF circuit optimization [14], microwave filter design [15]-[16], vehicle crashworthiness [17], yield analysis [18], and system calibration [19].

4.2 THE SPACE MAPPING APPROACH

SM assumes the existence of a coarse model and a fine model for the same problem. The coarse model is usually relatively fast in terms of the computational time but less accurate. The fine model is usually CPU intensive but very accurate.

SM intelligently links the companion coarse and fine models with different complexity together. It establishes a mapping between coarse model and fine model parameters to match the responses of both models (Fig. 4.1), such that the accuracy and computational speed are achieved simultaneously.

Typical design parameters for EM problems are the physical geometry and

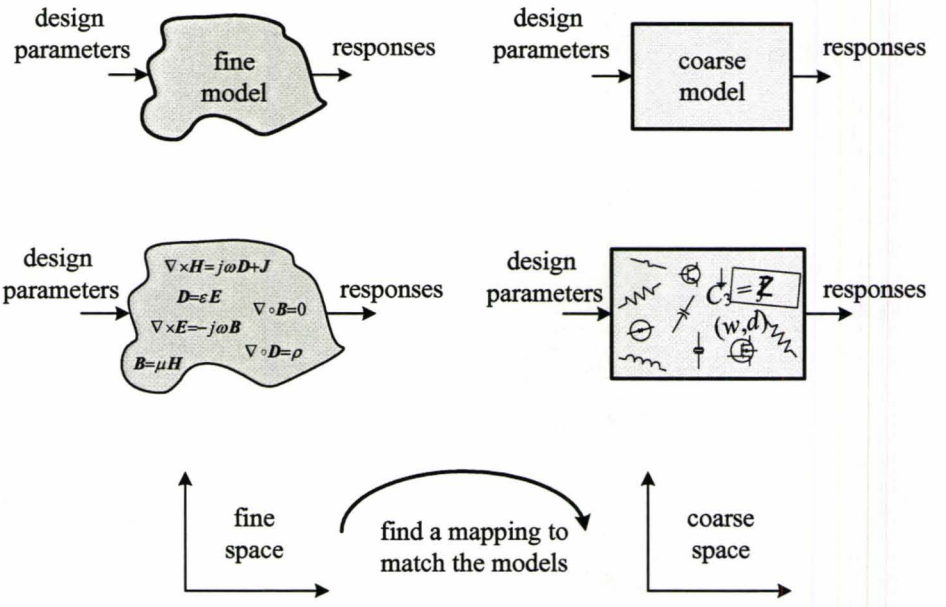

Fig 4.1: Linking companion coarse (empirical) and fine (EM) models through a mapping [10].

material parameters of a filter, an antenna or the value of electronic devices in the circuit board. Typical responses are time domain waveform, *S*-parameters or other responses. In the design process, we try to determine the design parameters which satisfy the design specifications imposed on the structure responses.

4.2.1 Space Mapping Construction

Throughout the construction of SM, a suitable "surrogate" model is created. The "surrogate" model is faster than the time intensive fine model and it is at least as accurate as the underlying coarse model. SM approach updates the "surrogate" mode to better approximate the fine model.

In effect, this approach is equivalent to correcting the error in the surrogate model responses throughout the region of interest to match the corresponding fine model responses. More importantly, we avoid the time consuming fine model evaluations and achieve accuracy similar to that of the fine model at the same time.

Mathematically, we denote the coarse model

$$\boldsymbol{R}_c = \boldsymbol{R}_c(\boldsymbol{x}_c) \tag{4-1}$$

where $\boldsymbol{x}_c$ is the coarse model input design parameters and $\boldsymbol{R}_c$ is the coarse model responses. The fine model is denoted by

$$\boldsymbol{R}_f = \boldsymbol{R}_f(\boldsymbol{x}_f) \tag{4-2}$$

where $\boldsymbol{x}_f$ is the fine model input design parameters and $\boldsymbol{R}_f$ is the fine model responses. The surrogate model used to replace the fine model is given by

$$\boldsymbol{R}_s(\boldsymbol{x}) = \boldsymbol{A} \cdot \boldsymbol{R}_c(\boldsymbol{B} \cdot \boldsymbol{x} + \boldsymbol{c}, \boldsymbol{x}_p) + \boldsymbol{d} \tag{4-3}$$

where $\boldsymbol{A}$, $\boldsymbol{B}$, $\boldsymbol{c}$, $\boldsymbol{d}$ and $\boldsymbol{x}_p$ are the model parameters. $\boldsymbol{x}_p$ is the vector of preassigned parameters and $\boldsymbol{R}_s$ is the surrogate model responses.

Here, model parameters are used to adjust the surrogate model to match the fine model responses, such that $\boldsymbol{R}_s \approx \boldsymbol{R}_f$ within the region of interest. The mapping is carried out through Parameter Extraction (PE) process as shown in (4-4).

$$(\boldsymbol{A}, \boldsymbol{B}, \boldsymbol{c}, \boldsymbol{d}, \boldsymbol{x}_p) = \arg \min_{(\boldsymbol{A}, \boldsymbol{B}, \boldsymbol{c}, \boldsymbol{d}, \boldsymbol{x}_p)} \left\{ \left\| \boldsymbol{R}_s(\boldsymbol{x}) - \boldsymbol{R}_f(\boldsymbol{x}) \right\| \right\} \tag{4-4}$$

The PE step is crucial to the success of SM. It is an optimization process that

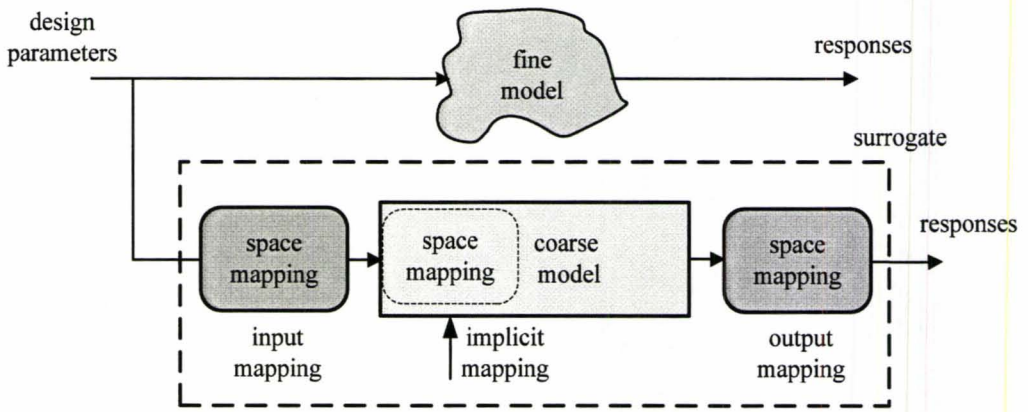

Fig 4.2: Space Mapping concept [11].

extracts model parameters of the surrogate model (4-4) to match the fine model responses ($\boldsymbol{R}_s \approx \boldsymbol{R}_f$). Inadequate response data in PE process may lead to nonunique solutions. Sufficient data to overdetermine a solution should be sought. During PE process, model parameters $(\boldsymbol{A}, \boldsymbol{B}, \boldsymbol{c}, \boldsymbol{d}, \boldsymbol{x}_p)$ are the optimizable parameters and the design parameters $\boldsymbol{x}$ are treated as constants.

Depending on the selected model parameters used for surrogate model in (4-3), different types of SM are defined and used. They include Input SM, Output SM (OSM), Implicit SM (ISM) and Tuning SM (TSM). In addition, any combination of these can be applied (Fig. 4.2).

4.2.2 Input Space Mapping

Input SM (4-5, 4-6 and Fig. 4.3) aims at adjusting the misalignment of input

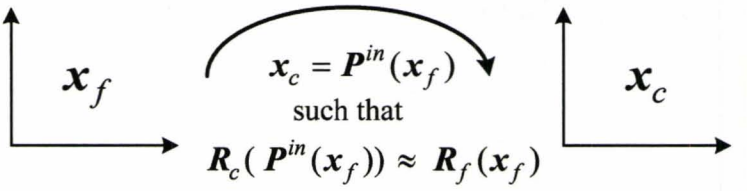

Fig 4.3: Input Space Mapping concept [10].

parameters between the coarse model and the fine model. It affects the accuracy of responses indirectly. Usually it is used in the early stage of the process (Fig. 4.2) and is given by:

$$R_s(x) = R_c(B \cdot x + c) \tag{4-5}$$

$$(B, c) = \arg \min_{(B,c)} \left\{ \left\| R_s(x) - R_f(x) \right\| \right\} \tag{4-6}$$

The mapping relationship P^{in} is established in the input parameter space between the coarse model input parameters x_c and fine model input parameters x_f such that the response of the coarse model R_c is close enough to the response of fine model R_f. The accuracy of the coarse model response is improved by mapping x_f to x_c before coarse model was evaluated.

4.2.3 Output Space Mapping (OSM)

OSM [8], [10], [20]-[21] is illustrated in Fig. 4.4. The objective of OSM is to eliminate the residue misalignment between fine model and surrogate model responses. It affects the accuracy of the responses directly and it is usually used in the final stage of the

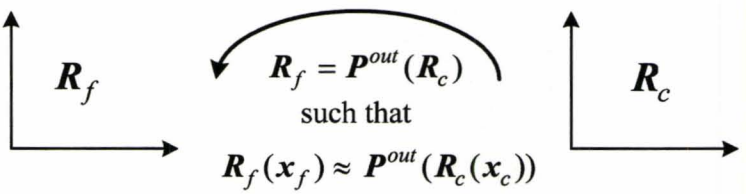

Fig 4.4: Output Space Mapping concept [10].

process (Fig. 4.2). It is given by the following equations:

$$R_s(x) = A \cdot R_c(x) + d \tag{4-7}$$

$$(A, d) = \arg \min_{(A,d)} \left\{ \left\| R_s(x) - R_f(x) \right\| \right\} \tag{4-8}$$

The mapping relationship P^{out} directly maps the coarse model response R_c to the fine model response R_f (Fig. 4.4). The accuracy of the coarse model is thus improved by mapping R_c to R_f after the coarse model was evaluated.

4.2.4 Implicit Space Mapping (ISM)

ISM [8], [20], [22]-[23] (4-9, 4-10 and Fig. 4.5) is another variation of the SM concept that exploiting the idea of preassigned parameters [24]. It is given by:

$$R_s(x) = R_c(x, x_p) \tag{4-9}$$

$$x_p = \arg \min_{x_p} \left\{ \left\| R_s(x) - R_f(x) \right\| \right\} \tag{4-10}$$

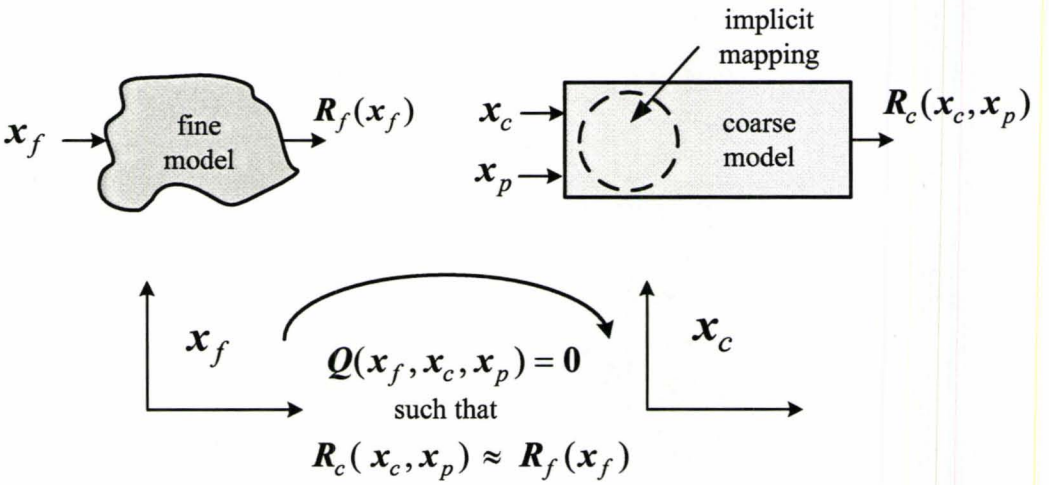

Fig 4.5: Implicit Space Mapping concept [10].

The preassigned parameters x_p are extracted to match the fine model and surrogate model response. It is usually used in the middle stage of the process (Fig. 4.2). These preassigned parameters are usually non-optimizable in traditional optimization process. Typical examples of preassigned parameters include the dielectric constant and substrate height.

4.2.5 Tuning Space Mapping (TSM)

TSM [25]-[27] (4-12 and Fig. 4.6) is the most recently developed SM method. It integrates the tuning concept into SM. In TSM, the surrogate model is replaced by a so-called "tuning model", which is constructed by introducing into the fine model circuit theory-based components (tuning components). The characteristic parameters of the components are chosen to be "tuning parameters".

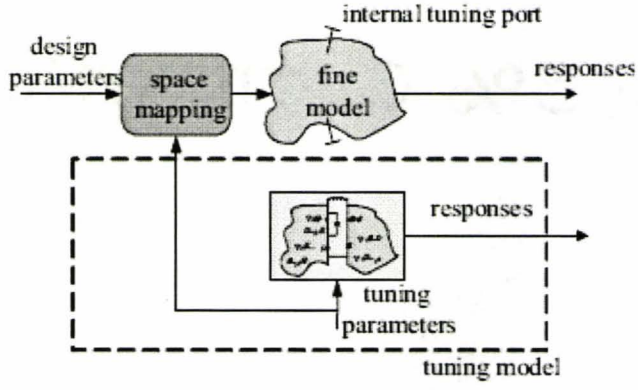

Fig 4.6: Tuning Space Mapping concept [25].

Tuning parameters $\boldsymbol{x}_t$ are adjusted by a PE process (4-12) to match the fine model responses ($\boldsymbol{R}_t \approx \boldsymbol{R}_f$). The PE process is given by:

$$\boldsymbol{x}_t = \arg \min_{\boldsymbol{x}_t} \left\{ \left\| \boldsymbol{R}_t(\boldsymbol{x}_t) - \boldsymbol{R}_f(\boldsymbol{x}) \right\| \right\} \tag{4-12}$$

where $\boldsymbol{x}_t$ is the tuning parameters and $\boldsymbol{R}_t$ is the tuning model responses

4.3 SPACE MAPPING FRAMEWORK

The SM concept has two main applications: SM optimization for design purposes and SM modeling for simulation purposes.

In SM optimization, only the final optimal design parameters are of interest. In this case, model parameters are updated at each iteration to match the current surrogate model response with fine model. The matching between surrogate model and fine model

is only valid for the current iteration evaluated at the current design parameters. The model parameters are "dynamic" quantities. The updated surrogate model at the current iteration is then used to predict the new set of design parameters for the next iteration. SM optimization features fast computational time and convergence in a few iterations.

In SM modeling, the model parameters are extracted only once at the final stage to match the surrogate model responses with the fine model within a region of interest. The matching between the surrogate model and the fine model is valid with all the set of design parameters evaluations in the region of interest.

The surrogate model parameters are optimized through PE to match the responses at the preselected sets of "base points". Other sets of "test points" are used to evaluate the performance of surrogate model in terms of accuracy.

The "optimized" surrogate model then replaces the fine model for simulation purposes. SM modeling features fast simulation time and acceptable accurate responses in the region of interest.

4.3.1 Space Mapping Optimization

Generally, the framework for SM optimization has the followings steps [28] as in Fig. 4.7:

Step 1 Define fine mode and coarse models. Choose a mapping method such as Input SM, OSM , ISM, TSM or combination of these for surrogate model.

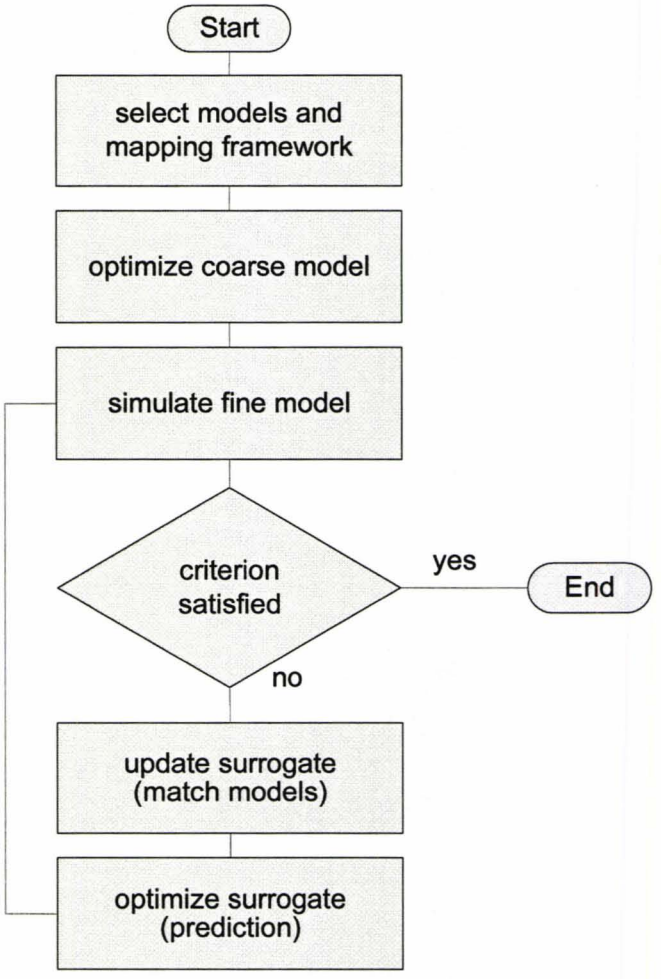

Fig 4.7: Space Mapping Optimization flow chart [11].

Step 2 Surrogate model optimization. Here, design parameters are variables and model parameters are constants.

Step 3 Fine model evaluation with optimal surrogate model design parameters.

Step 4 Terminate if responses meet design specifications.

Step 5 Parameters extraction is carried out to match responses between surrogate model and fine model. Here, design parameters are constants and model parameters are variables.

Step 6 Surrogate model (re)optimization with updated model parameters from *Step 5* to determine the new set of design parameters. Then go to *Step 3*. Here, design parameters are variables and model parameters are constants.

4.3.2 Space Mapping Modeling

Usually, the framework for SM modeling has the followings steps [28] as in Fig. 4.8:

Step 1 Define fine model and coarse model. Chose a mapping approach such as ISM, OSM, ISM or combination of these for surrogate model.

Step 2 Generate the base points and multiple test points.

Step 3 Simulate the fine model at all the base points.

Step 4 Match the surrogate to the fine model through PE using all the base points simultaneously. Here, the design parameters are constants and the model parameters are variables.

Step 5 Test the SM-based surrogate model at the test points.

Step 6 If necessary, interpolate the surrogate responses for arbitrary values.

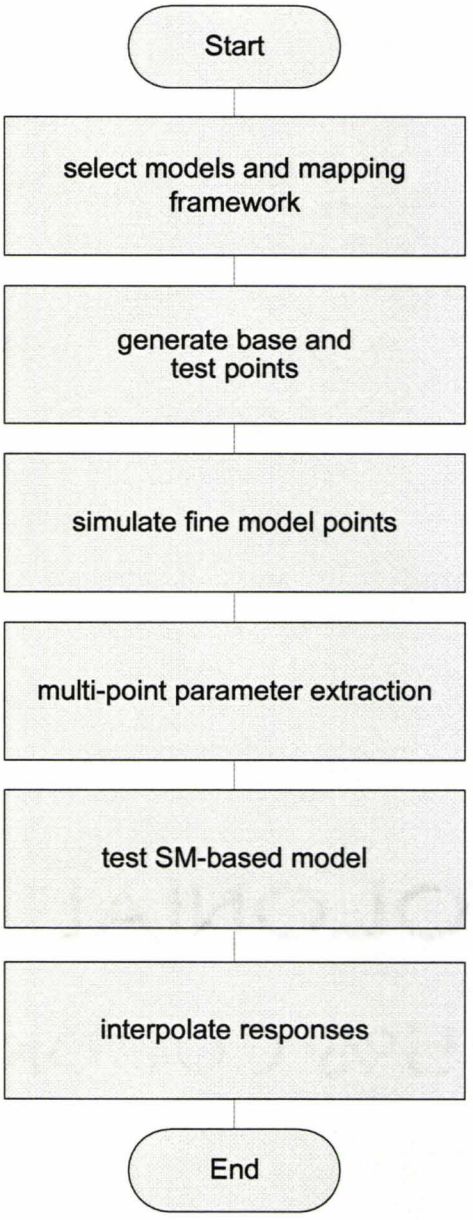

Fig 4.8: Space Mapping Modeling flow chart [11].

4.5 CONCLUSIONS

In this chapter, we briefly review the concept of Space Mapping (SM) and its framework for optimization and modeling. We discussed different mapping methods in SM to match surrogate model responses with fine model. The Parameter Extraction (PE) step is the key to establish the mapping and updating surrogate model. The surrogate model is then utilized in predicting new designs in the case of SM optimization. It is used as a substitute of the time intensive fine model in the case of SM modeling. The framework for SM optimization and SM modeling is present step by step.

REFERENCES

[1] M. B. Steer, J. W. Bandler, and C. M. Snowden., "Computer-aided design of RF and microwave circuits and systems," *IEEE Trans. Microwave Theory Tech.*, vol. 50. pp. 966-1005, Mar. 2002.

[2] J. W. Bandler and S. H. Chen, "Circuit optimization: The state of art," *IEEE Trans. Microwave Theory Tech.*, vol. 36, pp. 424-443, Feb. 1988.

[3] J. W. Bandler, "Computer optimization of microwave circuits." Proc European Microwave Conf., Stockholm, Sweden, pp. B8/S: 1-S: 8, Aug. 1971.

[4] J. W. Bandler, R. M. Biernacki, S. H. Chen, P. A. Grobelny, and R. H. Hemmers, "Space mapping technique for electromagnetic optimization," *IEEE Trans. Microwave Theory Tech.*, vol. 42, pp. 2536-2544, Dec. 1994.

[5] J. W. Bandler, R. M. Biernacki, S. H. Chen, R. H. Hemmers. And K. Madsen, "Electromagnetic optimization exploiting aggressive space mapping," *IEEE Trans. Microwave Theory Tech.*, vol. 43, pp. 2874-2882, Dec. 1995.

[6] S. Koziel and J.W. Bandler, "Controlling convergence of space –mapping algorithms for engineering optimization," *Int. Symp. Systems and Electronics, URSI ISSSE 2007*, Montreal, Canada, pp. 21-23, July.-Aug. 2007.

[7] K. Madsen and J. Sondergaard, "Convergence of hybrid space mapping algorithms," *Optimization and Engineering*, vol. 5, no. 2, pp. 145-156, Jun. 2004.

[8] M. H. Bakr, *Advances in Space Mapping Thechnology Exploiting Implicit Space Mapping and Output Space Mapping*, Ph.D. Thesis, Department of Electrical and Computer Engineering, McMaster University, 2000.

[9] S. Koziel, J. W. Bandler, and K. Madsen, "Towards a rigorous formulation of space mapping technique for engineering design," P*roc. Int. Symp. Circuits, Syst., ISCAS*, Kobe, Japan, pp. 5605-56-8, May 2005.

[10] J. W. Bandler, Q. S Cheng, S. A Dakroury, A. S Mohamed, M. H. Bakr, K. Madsen and J. Sondergaard, "Space mapping: the state of the art," *IEEE Trans. Microwave Theory and Tech.,* vol. 52, no. 1, pp 337-361, Jan. 2004.

[11] J. W. Bandler, Q. S. Cheng, S. Koziel, and K. Madsen, "Why space mapping works," *Second Int. Workshop on Surrogate Modeling and Space Mapping for Engineering Optimization, SMSMEO-06*, Lyngby, Denmark, Nov. 2006.

[12] J. Zhu, J. W. Bandler, N. K. Nikolova, and S. Koziel, "Antenna design through space mapping optimization," *IEEE MTT-S Int. Microwave Symp.*, San Francisco, CA, pp. 1605-1608, Jun. 2006.

[13] J. Zhu, J. W. Bandler, N. K. Nikolova, and S. Koziel, "Antenna optimization through space mapping," *IEEE Trans. Antennas Propag.*, vol. 55, no. 3, pp. 651-658, Mar. 2007.

[14] W. Yu and J. W. Bandler, "Optimization of spiral inductor on silicon using space mapping," *IEEE MTT-S Int. Microwave Symp.*, San Francisco, CA, pp. 1085-1088, Jun. 2006.

[15] S. Amari, C. LeDrew, and W. Menzel, "Space-mapping optimization of planar coupled-resonator microwave filters," *IEEE Trans. Microwave Theory Tech.*, vol. 54, no. 5, pp. 2153–2159, May 2006.

[16] M. A. Ismail, D. Smith, A. Panariello, Y. Wang, and M. Yu, "EM-based design of large-scale dielectric-resonator filters and multiplexers by space mapping," *IEEE Trans. Microwave Theory Tech.*, vol. 52, no. 3, pp. 386–392, Jan. 2004.

[17] M. Redhe and L. Nilsson, "Using space mapping and surrogate models to optimize vehicle crashworthiness design," *9th AIAA/ISSMO Multidisciplinary Analysis and Optimization Symp.*, Atlanta, GA, Paper AIAA-2002-5536, Sep. 2002.

[18] J. W. Bandler, J. E. Rayas-Sánchez, and Q. J. Zhang, "Yield-driven electromagnetic optimization via space mapping-based neuromodels," *Int. J. RF Microwave Computer-Aided Eng.*, vol. 12, pp. 79–89, 2002.

[19] M. H. Bakr, K. Wang and M. J. Deen, "Accuracy Improvement of Magnetic Tracking Systems Using ANNs and Space Mapping Modeling," *ACES Conference*, Niagara Falls, pp. 603-608, March 2008.

[20] J. W. Bandler, Q. S. Cheng, D. H. Gebre-Mariam, K. Madsen, F. Pedersen, and J. Søndergaard, "EM-based surrogate modeling and design exploiting implicit, frequency and output space mappings," *IEEE MTT-S Int. Microwave Symp. Dig.*, Philadelphia, PA, pp. 1003–1006, Jun. 2003.

[21] S. Koziel, J. W. Bandler, and K. Madsen, "A space-mapping framework for engineering optimization—theory and implementation," *IEEE Trans. Microwave Theory Tech.*, vol. 54, no. 10, pp. 3721–3730, Oct. 2006.

[22] J. W. Bandler, Q. S. Cheng, N. K. Nikolova, and M. A. Ismail, "Implicit space mapping optimization exploiting preassigned parameters," *IEEE Trans. Microwave Theory Tech.*, vol. 52, no. 1, pp. 378–385, Jan. 2004.

[23] Q. S. Cheng, J. W. Bandler, and J. E. Rayas-Sánchez, "Tuning-aided implicit space mapping," *Int. J. RF Microwave Computer-Aided Engineering,* vol.18, no. 5, pp. 445-453, Sept. 2008.

[24] J. W. Bandler, M. A. Ismail, and J. E. Rayas-Sánchez, "Expanded space mapping EM-based design framework exploiting preassigned parameters," *IEEE Trans. Circuits Syst. I*, vol. 49, pp. 1833–1838, Dec. 2002.

[25] J. Meng, S. Koziel, J. W. Bandler, M. H. Bakr, and Q. S. Cheng, "Tuning space mapping: a novel technique for engineering optimization," *IEEE MTT-S Int. Microwave Symp. Dig.*, Atlanta, GA, Jun. 2008

[26] S. Koziel, J. Meng, J. W. Bandler, M. H. Bakr, and Q. S. Cheng, "Accelerated microwave design optimization with tuning space mapping," *IEEE Trans. Microwave Theory Tech.*, submitted, May 2008.

[27] J. Meng, *Microwave Circuit Optimization Exploiting Tuning Space Mapping*, MASc Thesis, Department of Electrical and Computer Engineering, McMaster University, 2008.

[28] J. W. Bandler, and Q. S. Cheng, "New developments in space mapping CAD technology," *China-Japan Joint Microwave Conference*, Chengdu, China, pp. 1–4, Aug. 2006.

CHAPTER 5

2-D PORTABLE MAGNETIC TRACKING SYSTEMS (2 DOF)

5.1 INTRODUCTION

Ingestible medical devices such as wireless endoscopes are finding increasing use in diagnosing and monitoring the gastrointestinal tract. It has a camera fitted inside a pill for diagnostics purposes. Commercial ingestible imaging devices are available [1]-[5].

The imaging devices can tell us the existence of the problem source. However, it cannot accurately tell us the location of the problem. If we would like to monitor the recovery status, accurate position information is required to be correlated with observation images.

Most of these devices utilize low-frequency magnetic fields for position and orientation determination [6] - [15]. Because the magnetic field penetrates the body without attenuation or change, the tracking may be continuous. In addition, the field is not

limited by line-of-sight, which is usually required for optical tracking and ultrasonic tracking [16].

The objective of our work is to build a portable Magnetic Tracking System (MTS) for real time position and orientation detection. Our target is to build the user friendly MTS such that the signal source can be around the human body comfortably (probably a "jacket") and the sensor can be fitted inside a "pill" for real time position detection.

We design the geometrical shape of the field generator so that the field generating elements can be easily fitted around human body without affecting the patients' regular activities. We make the field sensing elements as small as possible to be put inside the capsule. For real-time position detection, we utilize Artificial Neural Networks (ANN). To improve the accuracy of the MTS, we utilize Space Mapping (SM) Modeling.

5.2 2-D PORTABLE MAGNETIC TRACKING MPLEMENTATION

To simplify the problem itself, we start our MTS implementation from a 2-D case. For 2-D MTS, we use three primary coils as field generator and one secondary coil as field sensor. We fix the orientation of the secondary coil at $\boldsymbol{n}_s = [0 \quad 0 \quad 1]^T$ and the observation plane at $z = 0.6$ cm. As a result, we only have 2 unknowns to be determined, which are the x and y coordinates of the field sensor.

The design specifications of our system are as follows:

1. A portable magnetic tracking system that does not affect the patients' regular activities.

2. Real-time position tracking.

3. Small sized sensor which can be built inside a "pill".

4. Worst case position error of 10.0 mm.

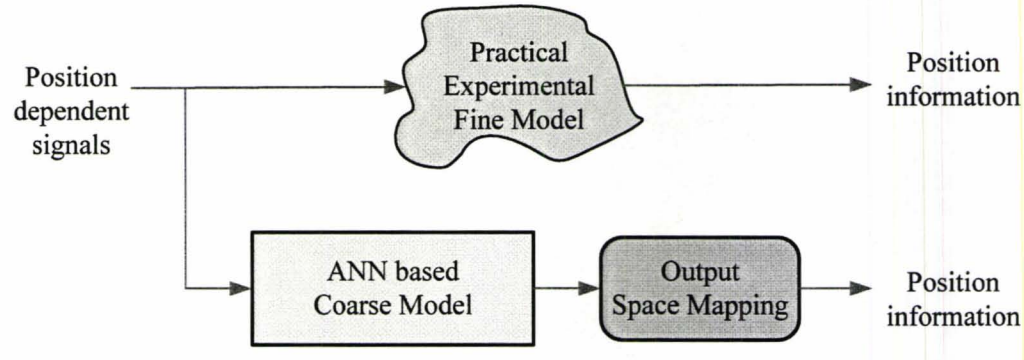

Fig 5.1: Magnetic Tracking exploiting ANN and SM modeling [17].

The block diagram for the overall MTS is shown in Fig 5.1. The time intensive fine model is replaced by SM modeling, which includes an ANN based coarse model for fast computational time and a SM model for accuracy improvement.

5.2.1 Mathematical Formulation

We calculate the magnetic flux by a simple dot product instead of integration over the sensor's vector area because the size of the field sensor is relatively small. For the 2-D special case, we have (5-3). Here we reproduce the equations (5-1 and 5-2) from Chapter 2 for convenience.

$$\boldsymbol{B}_{am} = \mu \oint_{c} \frac{I_{am} d\boldsymbol{L} \times \boldsymbol{R}(x,y,z)}{4\pi R^3(x,y,z)} \tag{5-1}$$

$$emf_{am} = 2\pi f \int_{s} \boldsymbol{B}_{am}(x,y,z) \bullet d\boldsymbol{s}(\phi,\theta,\varphi) \tag{5-2}$$

$$emf_{am} \approx 2\pi f B_{am\_z}(x,y) S \tag{5-3}$$

where B_{am_z} is the z component of the magnetic flux density $\boldsymbol{B}_{am}$.

To determine the positions uniquely from the nonlinear equation (5-3), we create an overdetermined system of 3 equations with 2 unknowns (5-4). By adding 1 additional independent equation, we eliminate situations where two completely different positions have the same $\boldsymbol{emf}_{am}$ signals. More independent equations correspond to more constraints in the solution space.

$$\boldsymbol{emf}_{am} = \begin{bmatrix} emf_{am\_1} \\ emf_{am\_2} \\ emf_{am\_3} \end{bmatrix} = \begin{bmatrix} 2\pi f_1 B^{c_1}_{am\_z}(x,y,I_{am\_1}) S \\ 2\pi f_2 B^{c_2}_{am\_z}(x,y,I_{am\_2}) S \\ 2\pi f_3 B^{c_3}_{am\_z}(x,y,I_{am\_3}) S \end{bmatrix} \tag{5-4}$$

where f_i is the excitation frequency of source i, $B^{c_i}_{am\_z}$ is the z component of the magnetic flux density due to the excitation current source at c_i (5-1), I_{am_i} is the amplitude of the AC current source i.

Finally, the position can be determined by a parameter extraction (PE) process, which iteratively updates $\boldsymbol{x} = \begin{bmatrix} x & y \end{bmatrix}^T$ to match the observation vector $\boldsymbol{emf}^{ob}_{am}$:

$$\boldsymbol{x}^* = \arg\left\{ \min_{\boldsymbol{x}} \left\| \underbrace{\boldsymbol{emf}^{ob}_{am}}_{\substack{\text{given observation} \\ \text{at unknown position}}} - \boldsymbol{emf}_{am}(\boldsymbol{x}) \right\|^2 \right\} \tag{5-5}$$

TABLE 5.1:
EXPERIMENTAL SETUP OF 2-D TRACKING SYSTEMS

	field generator			field sensor
	coil #1	coil #2	coil #3	
excitation frequency	1 kHz	2.5 kHz	5 kHz	N/A
Number of turns	19	18	17	100
wire type	AWG 26	AWG 26	AWG 26	AWG 30

5.2.2 Field Generator

For the field generating elements, we use 3 primary coils around the side of a 12-faced cylinder (Fig. 5.2). Different spatial configurations represent different excitation source as in (5-1 and 5-4). Different excitation source means different line integral path (5-1) for magnetic flux density $\boldsymbol{B}$ calculation. The number of turns for each coil is 19, 18 and 17 (TABLE 5.1).

There are two main purposes of selecting this geometrical shape of the field generator (Fig. 5.2). The first one is to fit the patient's body around his stomach and allow him to move around with the portable system. The second reason is to create a unique magnetic field value for each point in the region of interest. The more distinct the field distribution, the more independent the equations (5-4) become and the more likely we can eliminate the possibility of multiple solutions. In addition, distinct field values will result in relatively high *emf* sensitivities with respect to position changes.

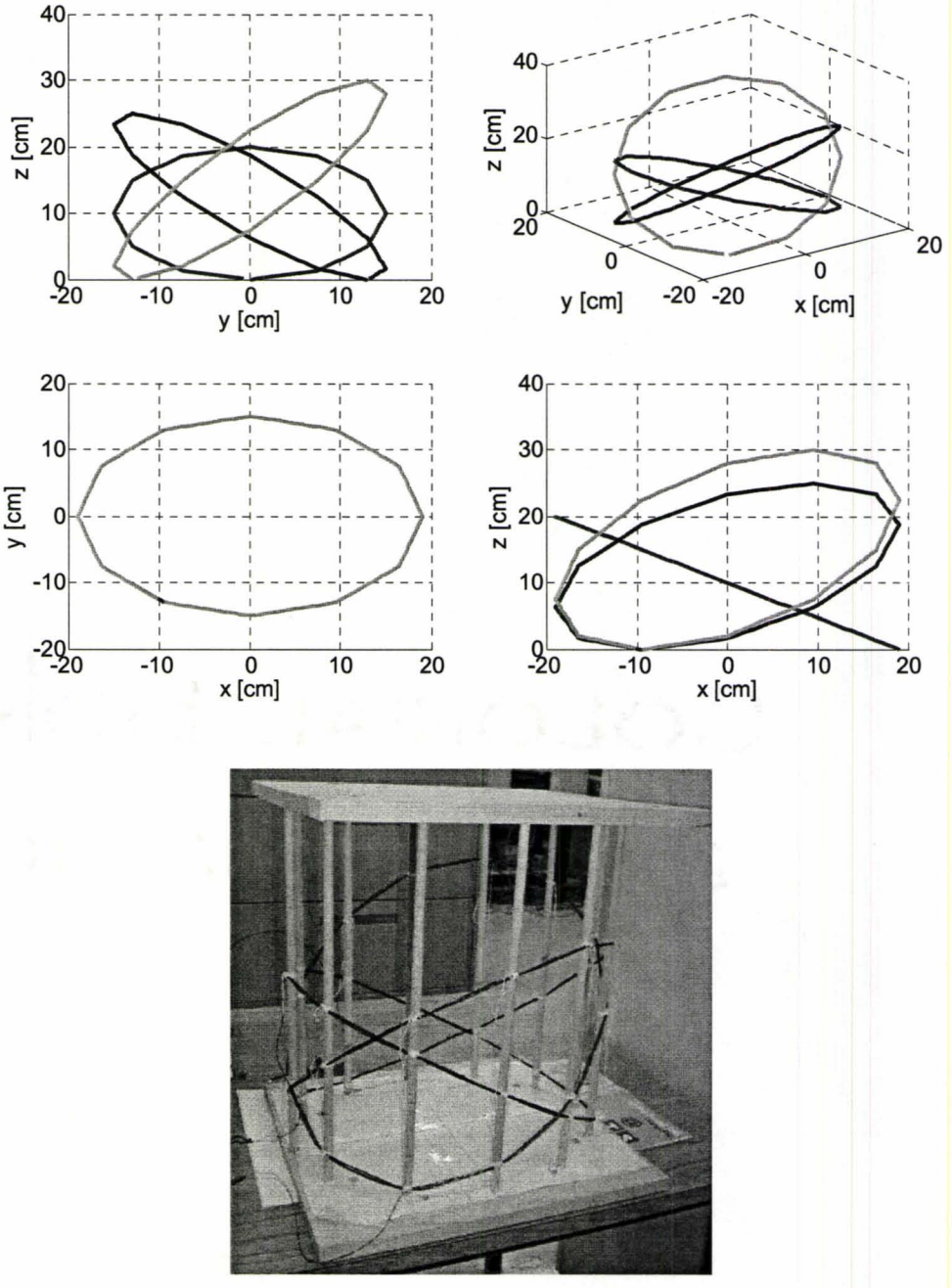

Fig 5.2: Field generator's spatial configuration.

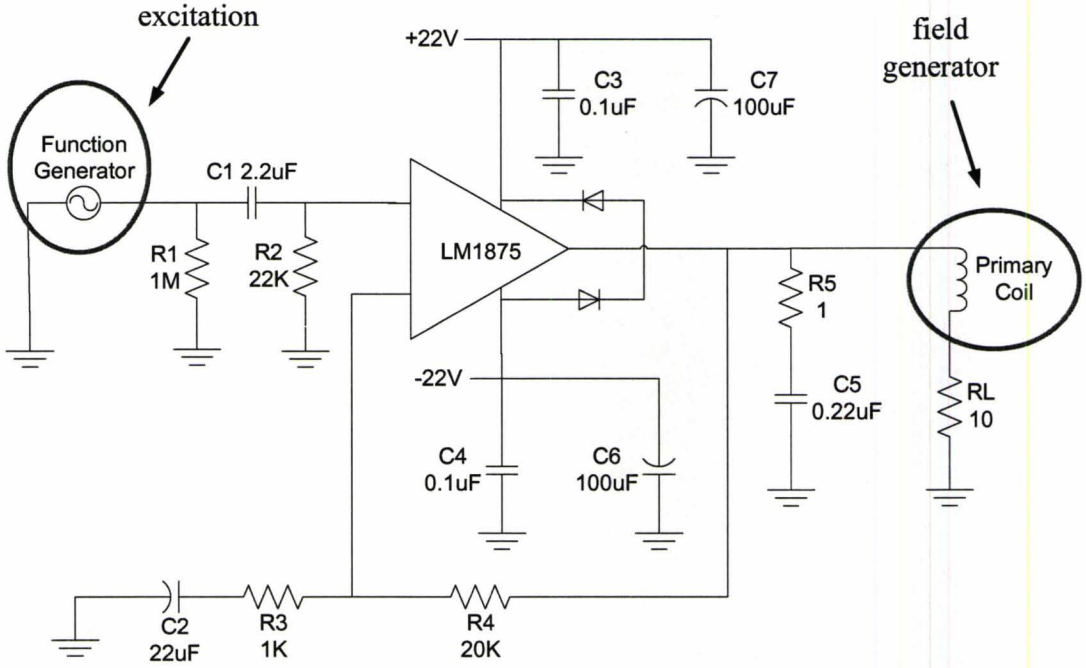

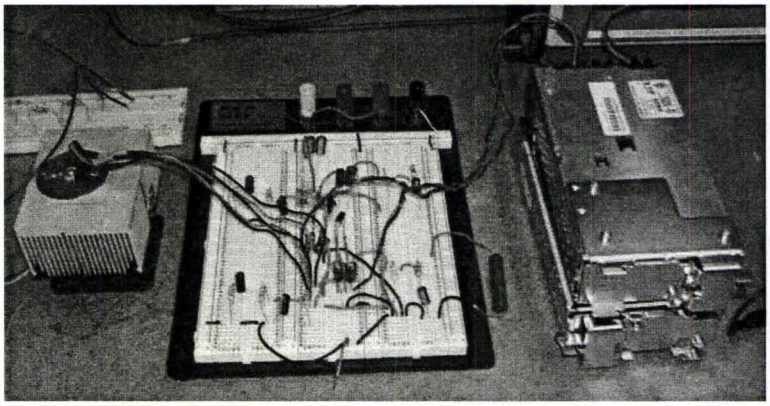

Fig 5.3: The power amplifier circuit used to excite the primary coils. Small adaptation of the audio amplifier in [18].

We excite the primary coils with pure sinusoidal currents by a function generator (Hewlett-Packard 3311A). Each coil has its own frequency to enable the separation of the

excitation source and the corresponding emf_{am} pairs by filtering. Because of the limited number of measurement instruments, we cannot measure 3 independent emf_{am} signals simultaneously. Instead, we excite the primary coils one by one and measure its corresponding emf_{am} signal. We arbitrarily choose the frequencies 1.0 kHz, 2.5 kHz and 5.0 kHz for the primary coils (TABLE 5.1).

To have sufficient current excitation for each coil, we utilize a 20 Watts Audio Power Amplifier in the overall circuit (Fig. 5.3).

5.2.3 Field Sensor

For the field sensor, we use a small-size circular loop of copper wire with 0.64 cm in radius and 100 turns (Fig. 5.4 and TABLE 5.1). The induced emf_{am_i} signal is measured using a Lock-in Amplifier SR850 (Stanford Research Systems Fig. 5.5). We measure different excitation ($\boldsymbol{B}_{am}^{c_i}$) and observation (emf_{am_i}) pairs by changing excitation coils and reference frequency input for the Lock-in Amplifier.

5.2.4 Signal Processing Unit Exploiting ANN

Our signal processing unit is a MatLab [20] based program that extracts the position parameters from $\boldsymbol{emf}_{am}$. This PE process has to be carried out iteratively and repeatedly for each set of measurements $\boldsymbol{emf}_{am}^{ob}$.

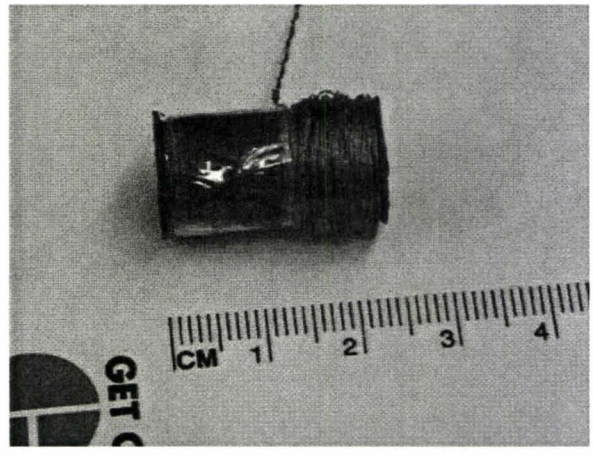

Fig 5.4: Field sensor for 2-D Magnetic Tracking Systems.

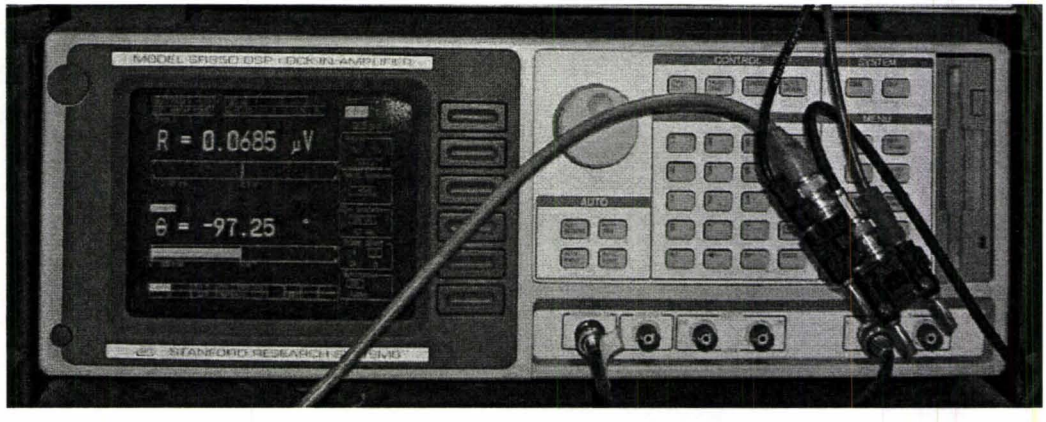

Fig 5.5: Lock-in Amplifier SR850 [19].

$$\boldsymbol{emf}_{am} = \begin{bmatrix} emf_{am\_1} \\ emf_{am\_2} \\ emf_{am\_3} \end{bmatrix} \longrightarrow \boxed{\text{Artificial Neural Networks}} \longrightarrow \begin{bmatrix} x \\ y \end{bmatrix}$$

Fig 5.6: The Artificial Neural Networks (ANN) model.

To avoid this time-consuming PE process and to achieve real-time position detection, we train an ANN [21]-[22] to model the mapping between $\boldsymbol{emf}_{am}$ and its corresponding position parameters $\begin{bmatrix} x & y \end{bmatrix}^T$ (see Fig. 5.6).

This ANN is trained through analytical computer simulations exploiting (eqn. 5-1 to 5-4). The region of interest is fixed at:

$$\begin{cases} x \in [-10\ cm \quad +10\ cm] \\ y \in [-10\ cm \quad +10\ cm] \\ z = 0.6\ cm \end{cases} \tag{5-6}$$

The training data set is on a $2.0\ cm \times 2.0\ cm$ mesh grid uniformly spread over the observation plane (5-6) and the testing data set is on a $1.0\ cm \times 1.0\ cm$ mesh grid (Fig. 5.7). Each 2-D position $\begin{bmatrix} x & y \end{bmatrix}^T$ in the training data set is correlated with its corresponding $\boldsymbol{emf}_{am}$ signal through the training process, such that the ANN should be able to tell us the position $\begin{bmatrix} x & y \end{bmatrix}^T$ as soon as the corresponding $\boldsymbol{emf}_{am}$ signal is given to it. The testing data set is used to evaluate the performance of the ANN model. An ANN model is good only when it is able to give the correct position when the corresponding signal from the testing data set is given.

ANN is trained by the software ***NeuroModeler*** [23]. Three-layer ANN structure is used (Fig. 5.8). The training options are in TABLE 5.2.

We start with a small number of hidden neurons (2 in our case) and keep adding hidden neurons to achieve the best ANN performance. The number of hidden neurons is

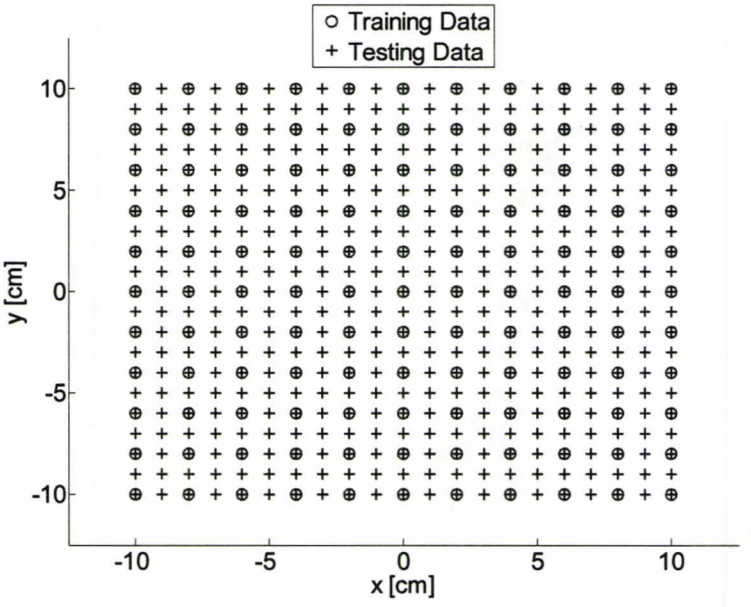

Fig 5.7: ANN training and testing data set.

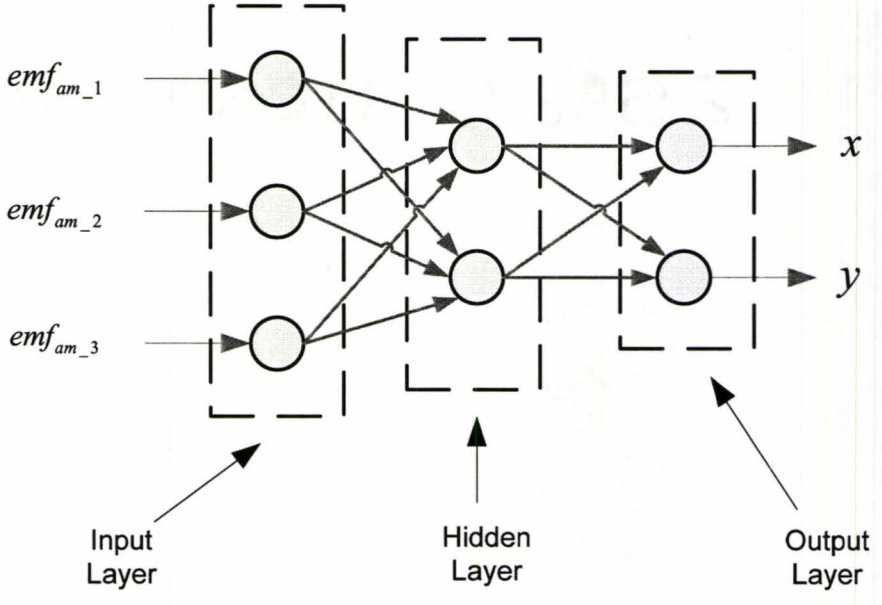

Fig 5.8: ANN structure applied for the 2-D Magnetic Tracking System.

TABLE 5.2:
ANN MODEL TRAINING OPTIONS

Training Method	Quasi-Newton (MLP)
Max. No. Epochs	494
Error Tolerance	0.0
Hessian Refresh Interval	500
Max Step Size	10.0
Model Parameter Tolerance	0.0

proportional to the complexity of the problem itself. Since the quantitative relationship between the number of hidden neurons and the complexity of the problem is not available.

By observing the error plots vs. the number of hidden neurons (Fig. 5.9 ~ Fig. 5.10), we found that good ANN model performance is obtained when the number of hidden neurons is greater than 15 and we decide to use 17 hidden neurons for our 2-D MTS.

After training the ANN with the theoretical input-output pairs, ANN is able to recognize the patterns and output the position accurately (Fig. 5.11 ~ Fig. 5.12 and TABLE 5.3). Here, we used 1 hidden layer with 17 hidden neurons for this ANN.

The circles in Fig 5.11 are the desired positions that we expect ANN to output for the given $\boldsymbol{emf}_{am}$ signals. The crosses are the position responses from the ANN model for

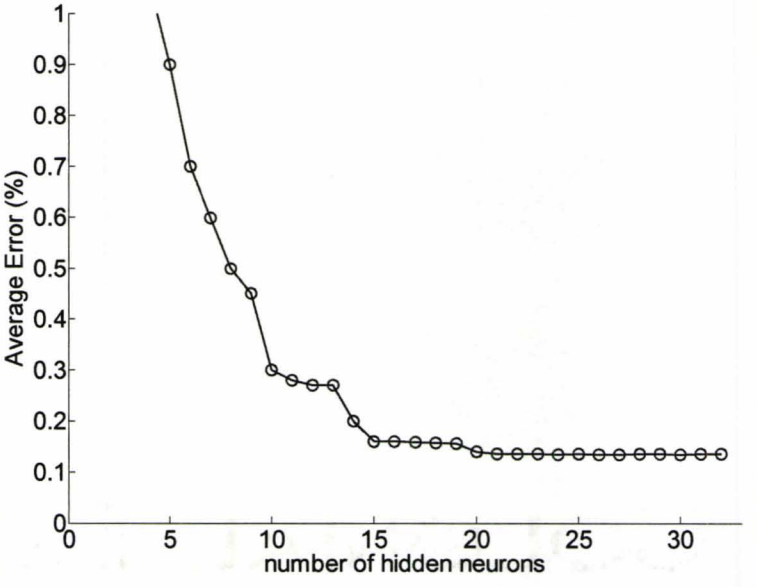

Fig 5.9: Average ANN training error.

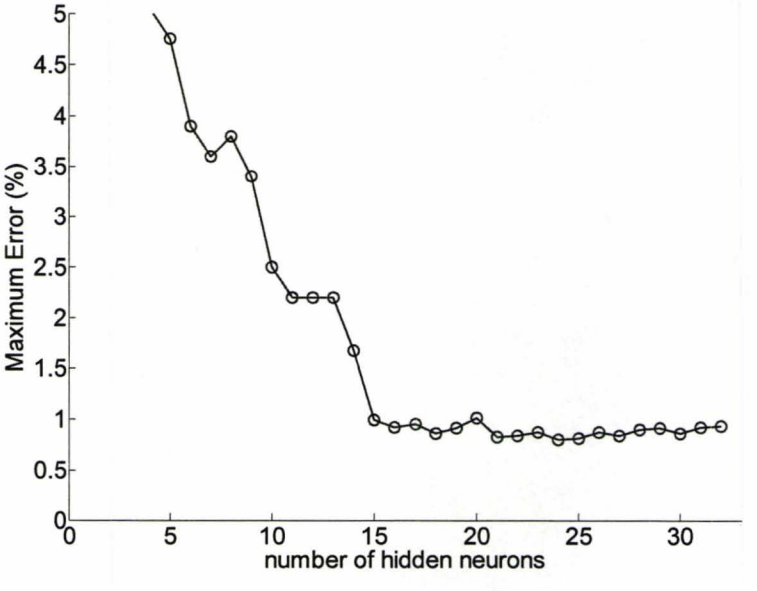

Fig 5.10: Maximum ANN training error.

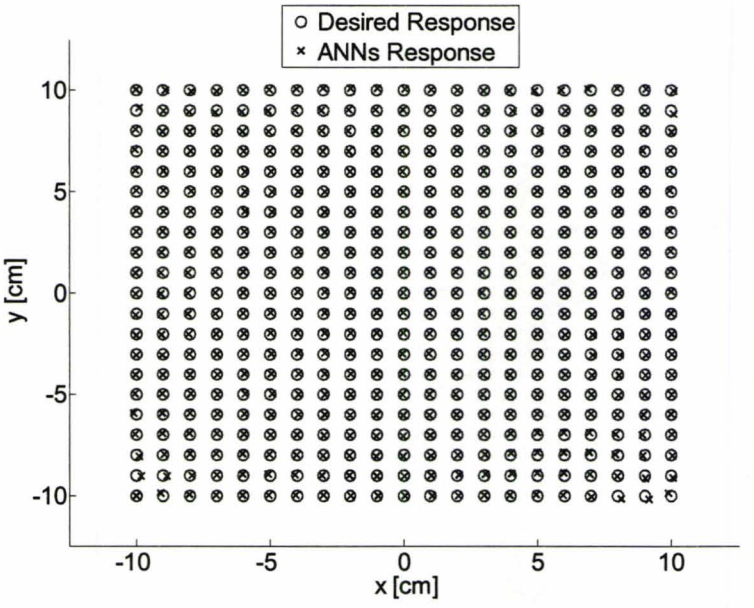

Fig 5.11: ANN response with theoretical $\boldsymbol{emf}_{am}$ input.

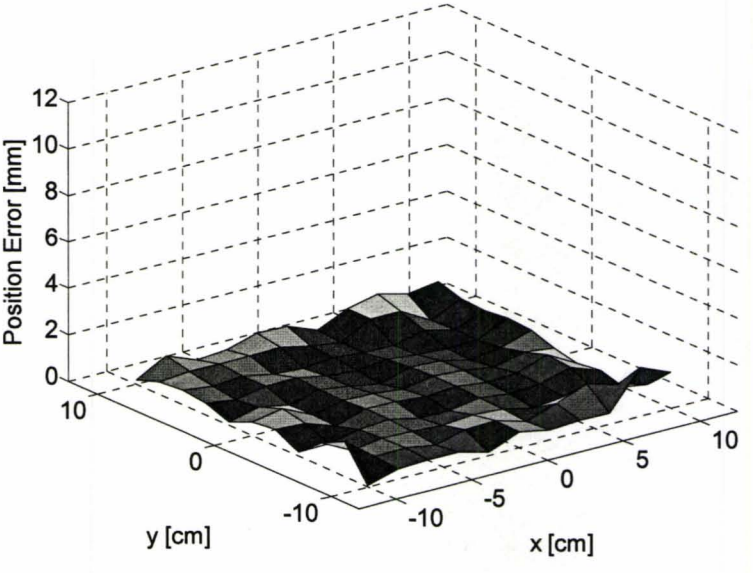

Fig 5.12: Position error surface of ANN output with theoretical $\boldsymbol{emf}_{am}$ input.

TABLE 5.3:
STATISTICAL POSITION ERROR

	ANN response
Number of points	441
Mean [mm]	0.5
Max [mm]	2.3
Standard deviation [mm]	0.3
Range [mm]	2.3

Position error is defined as the l_2 norm of the difference between exact position and the ANN output position.

the same $\boldsymbol{emf}_{am}$ signals. The position match is good for our 2-D MTS application. The position error is not zero (TABLE 5.3). The error surface plot is shown in Fig 5.12.

Experimentally, we measure the position defined signal $\boldsymbol{emf}_{am}^{ob}$. The average relative error is 2.56 % with maximum error of 9.69 % taking the theoretical $\boldsymbol{emf}_{am}$ as reference. The error is mainly caused by the environmental interferences from nearby conducting materials. The magnetic field induces currents in the conducting materials. The induced currents generate their own magnetic field which affects the original magnetic field in return.

Because of the measurements errors in $\boldsymbol{emf}_{am}^{ob}$, the position responses from the ANN model have some offset with the actual positions (Fig 5.13 ~ Fig 5.14).

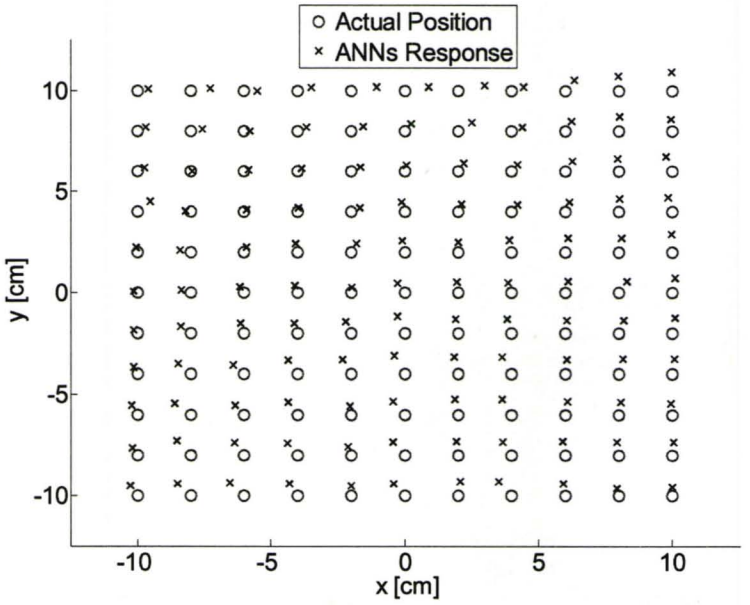

Fig 5.13: ANN response with experimental $\boldsymbol{emf}_{am}^{ob}$ input.

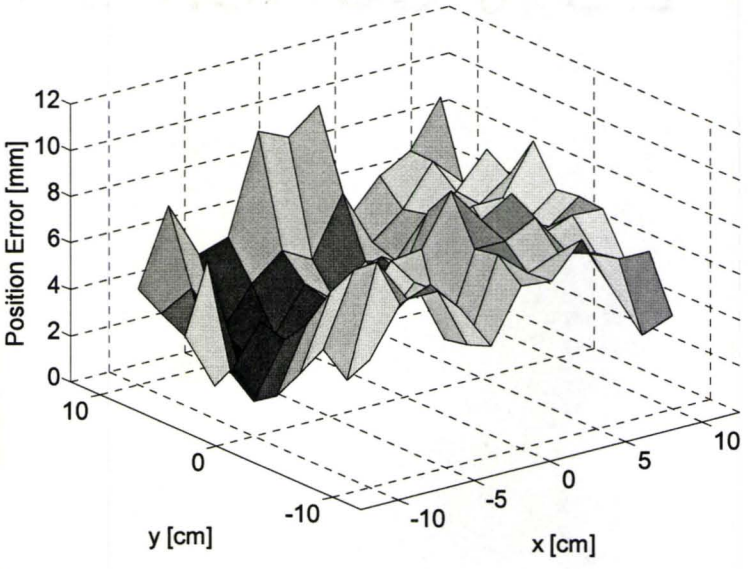

Fig 5.14: Position error surface of ANN output with experimental $\boldsymbol{emf}_{am}^{ob}$ input.

TABLE 5.4:
EXPERIMENTALLY STATISTICAL POSITION ERROR

	ANN response
Number of points	121
Mean [mm]	5.6
Max [mm]	10.1
Standard deviation [mm]	2.0
Range [mm]	9.6

Position error is defined as the l_2 norm of the difference between exact position and the ANN output position.

The circles in Fig 5.13 show the actual positions where we put the sensor and where we record the corresponding signal $\boldsymbol{emf}_{am}^{ob}$. The crosses denote the position responses from the ANN model with the experimental signal $\boldsymbol{emf}_{am}^{ob}$ as input. The position error is relatively large (TABLE 5.4). The error surface plot is shown in Fig 5.14.

5.2.5 System Calibration Exploiting SM Modeling

To correct the position offset, we utilize a system calibration exploiting SM concept. The trained ANN represents a course model as in Fig 5.1. It predicts the correct position accurately only with theoretical $\boldsymbol{emf}_{am}$ inputs. In reality, the measured $\boldsymbol{emf}_{am}^{ob}$ values do not match closely to the theoretical values $\boldsymbol{emf}_{am}$ due to the interference of other magnetic sources, the presence of nearby conducting materials, or the inaccuracies in modeling the primary coils and the secondary coils. In order to make accurate

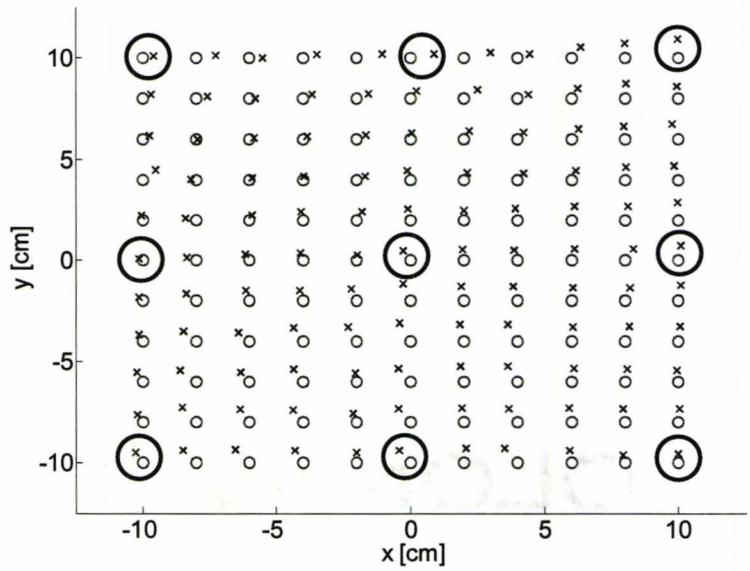

Fig 5.15: Selected calibration points as labeled with big black circle.

measurements, we put the tracking system far away from other magnetic sources. We also keep the geometrical shape of the built magnetic field system as close as possible to the configurations used in the ideal magnetic field simulations.

We apply system calibration by mapping the ANN output position to the actual position. We utilize minimum mapping parameters for position calibration. A simple linear output mapping (5-7) is assumed between the actual position and the ANN's predicted position. We also utilize minimum points to find the mapping parameters. We select 9 points out of 121 for mapping parameters determination (see Fig. 5.15):

$$\begin{bmatrix} x \\ y \end{bmatrix}_{\text{actual position}} = \begin{bmatrix} a_{11} & a_{12} \\ a_{21} & a_{22} \end{bmatrix} \begin{bmatrix} x \\ y \end{bmatrix}_{\text{ANNs response}} + \begin{bmatrix} b_{11} \\ b_{21} \end{bmatrix} \tag{5-7}$$

TABLE 5.5:
PARAMETER EXTRACTION OPTIONS

options	values
optimization functions	lsqnonlin
options.MaxIter	500
options.MaxFunEvals	2000
options.TolFun	10^{-6}
options.TolX	10^{-8}
options.DiffMaxChange	10^{-1}
options.DiffMinChange	10^{-8}

After carrying out the PE process, we optimize the mapping parameters and establish the position calibration formula (5-8).

$$\begin{bmatrix} x \\ y \end{bmatrix}_{\text{actual position}} = \begin{bmatrix} 0.9989 & -0.0321 \\ -0.0231 & 1.0048 \end{bmatrix} \begin{bmatrix} x \\ y \end{bmatrix}_{\text{ANNs response}} + \begin{bmatrix} -0.0001 \\ -0.0043 \end{bmatrix} \tag{5-8}$$

It should be noted that the positions x and y are in centimetres.

This PE is implemented in MatLab [20] with the options shown in TABLE 5.5. The starting point is shown in (5-9). The objective function is defined as in (5-10 and 5-11) for the entire selected sample points (9 points in this case).

$$\begin{bmatrix} a_{11} & a_{12} \\ a_{21} & a_{22} \end{bmatrix} = \begin{bmatrix} 1 & 0 \\ 0 & 1 \end{bmatrix} \text{ and } \begin{bmatrix} b_{11} \\ b_{21} \end{bmatrix} = \begin{bmatrix} 0 \\ 0 \end{bmatrix} \tag{5-9}$$

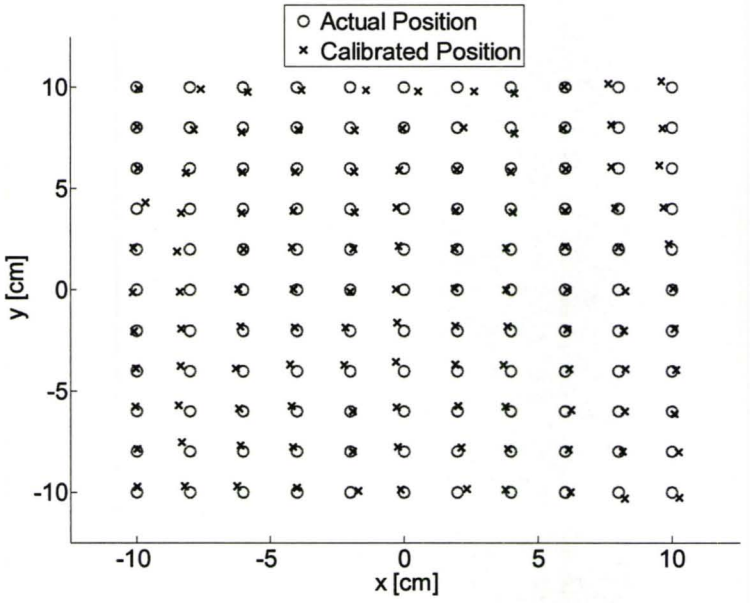

Fig 5.16: ANN response with after position calibration.

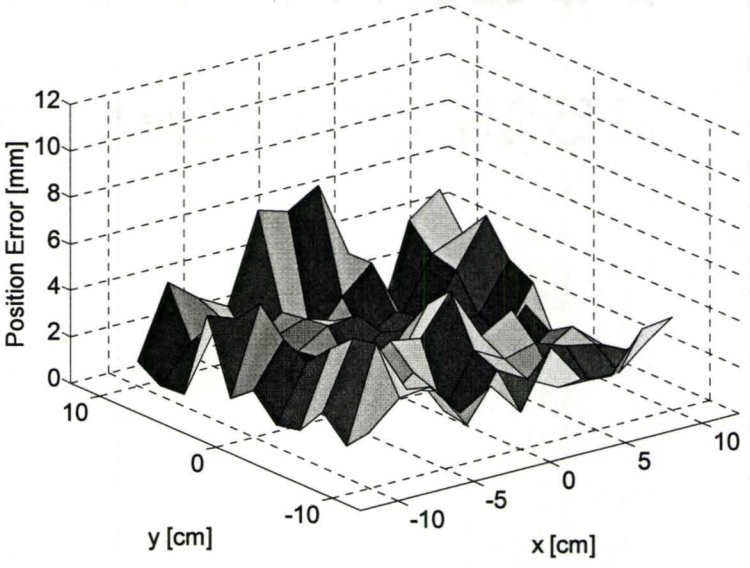

Fig 5.17: Position error surface plot after position calibration.

TABLE 5.6:
STATISTICAL POSITION ERROR COMPARISON

	before calibration	after calibration
Number of points	121	121
Mean [mm]	5.6	2.5
Max [mm]	10.1	6.6
Standard deviation [mm]	2.0	1.4
Range [mm]	9.6	6.5

Position error is defined as the l_2 norm of the difference between exact position and the ANN output position.

$$f(a_{11},a_{12},b_{11}) = \sum_{i=1}^{9}\left(\begin{bmatrix} a_{11} & a_{12} \end{bmatrix} \times \begin{bmatrix} x_i \\ y_i \end{bmatrix}_{ANN} + b_{11} - [x_i]_{actual} \right)^2 \tag{5-10}$$

$$f(a_{21},a_{22},b_{21}) = \sum_{i=1}^{9}\left(\begin{bmatrix} a_{21} & a_{22} \end{bmatrix} \times \begin{bmatrix} x_i \\ y_i \end{bmatrix}_{ANN} + b_{21} - [y_i]_{actual} \right)^2 \tag{5-11}$$

Finally, we apply this calibration formula (5-8) for the rest of position responses obtained from the ANN. We can see that the accuracy is improved statistically and graphically (Fig. 5.16 and Fig. 5.17 and TABLE 5.6).

5.3 EFFICIENCY OF 2-D PORTABLE MAGNETIC TRACKING SYSTEMS

The unique feature of our 2-D MTS is the utilization of both ANN and SM modeling. ANN significantly improves the computational time of position determination, which is the most time-consuming part in the system. SM modeling improves the accuracy of the position responses.

5.3.1 Artificial Neural Networks

For real-time position tracking application, we apply ANN model as our Signal Processing Unit. The functionality of the ANN model is the PE process of position information $[x \quad y]^T$ from the experimental signal $\boldsymbol{emf}_{am}^{ob}$ (5-5).

By comparing our ANN model implementing the PE with the traditional PE process we have the following observations:

Pros:

1. Extremely fast in terms of computational time.
2. Starting point independent.
3. Global minimum convergence.
4. Straight computation, no iterative process.

Cons:

1. Requires time consuming training process (TABLE 5.7).
2. Accuracy is guaranteed only in the region of interest.

TABLE 5.7:
COMPUTATIONAL TIME COMPARISON

	PE	ANN
Number of samples	121	121
Computational time	16 min	0.8 sec
number of local minimum	2	NA
Training time	NA	8 min

"NA" is defined as not applicable.

After the training process is completed, the ANN is a continuous model in the region of interest. The inputs for the ANN are the position-dependent signals $\boldsymbol{emf}_{am}^{ob}$ from the field sensor and the output is the 2-D position $[x \quad y]^T$ of the field sensor relative to the field generator.

The computational times for both the ANN model and traditional PE are shown in TABLE 5.7. The PE options are shown in TABLE 5.8. ANN is suitable for real-time computational tasks applications because of its short computational time. The only thing we have to sacrifice is the ANN training process which can be time-consuming. However, once the ANN is trained, we can use it without the need for further training.

5.3.2 Space Mapping Modeling

To improve the accuracy of the MTS, we applied ANN based coarse model and Output SM (Fig. 5.1 and 5-7).

TABLE 5.8:
2-D POSITION EXTRACTION OPTIONS

options	values
optimization functions	fmincon
lower bound [cm]	[-19 -15]
upper bound [cm]	[19 15]
objective function	$\left\|\boldsymbol{emf}_{am}^{ob} - \boldsymbol{emf}_{am}\right\|^2$
options.MaxFunEvals	500
options.TolX	10^{-8}

Our coarse model is the PE of the 2-D position from the $\boldsymbol{emf}_{am}$ signals (5-5) based on the ideal case of Faraday's induction law. Our fine model is the PE based on the practical case of Faraday's induction law. It takes into account the environmental interferences mostly caused by nearby conducting materials and manufacturing error of the setup, which are complicated to model mathematically.

To achieve fast and accurate position tracking simultaneously, we utilize ANN based coarse model with Output SM instead of complex fine model development. As a result, we avoid the time consuming fine model development and achieve the same degree of accuracy of position responses.

Here, the position calibration is dependent on the surrounding environment. We have to re-calibrate the system when the environment is changed. In addition, the geometrical shapes of the field generating elements have to be fixed without any twisting.

If the field generators are deformed, the resulting position responses will no longer be valid. Also, the position determination is based on the relative geometrical shapes between field generator and field sensor. Changes in the geometrical shape cause changes in the relationship between the position and its corresponding signals. Further, if the reference coordinate frame is deformed, then the position responses may be erroneous because there is no reference frame.

5.4 2-D MECHANICAL IMPLEMENTATIONS

Please refer to Chapter 6 section 6.4 for the details of the mechanical implementations, such as how to select the number of turns, the excitation frequency and the geometrical shapes. The effect of heterogeneous medium is discussed as well.

5.5 CONCLUSION

We present, for the first time, a portable MTS exploiting ANN and SM modeling.

We design a suitable geometry configuration for field generator and field sensor such that patients can carry the MTS during the examination without affecting their regular activities. Under this design constraint, we optimize the shape of the field generating elements of the field generator in order to achieve signals of high sensitivity with respect to position change.

A MatLab [20] program is developed to model the electromagnetic field distribution and the resulting induced signal. PE is implemented in MatLab Optimization Toolbox to verify the mathematical algorithm of position tracking.

We apply an ANN model to do the computational task for real-time position tracking, which is traditionally done by an iterative PE process. We utilize SM modeling for system calibration to improve the accuracy of position responses. We combine the ANN and SM modeling to achieve fast computational time and accurate position determination simultaneously so that we avoid the time consuming complex fine model development. Very good match of position responses is obtained between our calculated position and the actual position.

REFERENCES

[1] Given Image, Israel. (n.d). *Overview of Capsule Endoscopy*. Retrieved July 29, 2008, from http://www.givenimaging.com/en-us/Patients/Pages/pagePatient.aspx

[2] Olympus Corp, Japan. (2008). *EndoCapsule*. Retrieved July 29, 2008, from http://www.nano-tera.ch/nanoterawiki/EndoCapsule

[3] RF System Lab, Japan. (n.d). *The Next Generation Capsule Endoscope: Sayaka*. Retrieved July 29, 2008, from http://www.rfamerica.com/sayaka/index.html

[4] Intro Medic KIST, Korea. (2008). *MicoCam*. Retrieved July 29, 2008, from http://www.nano-tera.ch/nanoterawiki/MicroCam

[5] Jinshan Science & Technology, China. (2008). *OMOM*. Retrieved July 29, 2008, from http://www.nano-tera.ch/nanoterawiki/OMOM

[6] T. Nagaoka and A. Uchiyma, "Development of a small wireless position sensor for medical capsule devices," IEEE EMBS, *International Conference*, pp. 2137-2140, Sept. 2004.

[7] W. Hou, X. Zheng, and C. Peng, "Experimental Study of Magnetic-based Localization Model for Miniature Medical Device Placed Indwelling Human Body," *IEEE Conference*, Changhai, China, pp. 1309-1312, Sept 1-4, 2005.

[8] E. Paperno, I. Sasada, and E. Leonovich, "A new method for magnetic position and orientation tracking," *IEEE Trans. Magn.*, vol. 37, pp. 1938-1940, July 2001.

[9] E. Paperno, and P. Keisar, "Three-Dimensional Magnetic Tracking of Biaxial Sensors," *IEEE Trans. Magn.*, vol. 40, no. 3, pp. 1530-1536, May 2004.

[10] M. H. Bakr, K. Wang and M. J. Deen, "Accuracy Improvement of Magnetic Tracking Systems Using ANNs and Space Mapping Modeling," *ACES Conference*, Niagara Falls, pp. 603-608, March 2008.

[11] NDI. (2008). *NDI Electromagnetic (EM) Tracking Technology*, Retrieved July 30, 2008, from http://www.ndigital.com/medical/technology-em.php

[12] Ascension Technology Corporation. (2008). *Tracking 3D World*, Retrieved July 30, 2008, from http://www.ascension-tech.com/index.htm

[13] M. Schneider, "Measuring Position and Orientation using Magnetic Fields," U.S. Patent 6,073,043, June. 2000.

[14] F. H. Rabb, "Remote Object and Orientation Locator," U.S. Patent 4,314,251, Feb. 1982.

[15] A. S. Edelstein, "Magnetic Tracking Methods and Systems," U.S. Patent 6,675,123 B1, Jan. 2004.

[16] P. T. Anderson, G. L. Beauregard and C. D. Cherry, "Magnetic Tracking System," U.S. Patent 7,096,148 B2, Aug. 2006.

[17] J. W. Bandler, Q. S. Cheng, S. Koziel, and K. Madsen, "Why space mapping works," *Second Int. Workshop on Surrogate Modeling and Space Mapping for Engineering Optimization, SMSMEO-06*, Lyngby, Denmark, Nov. 2006.

[18] National Semiconductor Products. (2008). LM1875 – 20-W Audio Power Amplifier. Retrieved August 14, 2008, from: http://www.national.com/mpf/LM/LM1875.html

[19] *DSP Lock-In Amplifier model SR850*, Stanford Research Systems, 1999.

[20] MatLab ver. 7.1, The MathWorks Inc, 3 Apple Hill Drive, Natick, MA 01760-2098, USA, 1994, http://www.mathworks.com/

[21] Q. J. Zhang, K. C. Gupta. *Neural Networks: For RF and Microwave Design*. Boston: Artech House, 2000.

[22] S. Haykin. *Neural Networks: A Comprehensive Foundation (2nd Ed)*. Prentice Hall, 1999.

[23] ***NeuroModeler*** Ver. 1.5, Carleton University., 1125 Colonel By Drive, Ottawa, Canada, K1S 5B6.

CHAPTER 6

3-D PORTABLE MAGNETIC TRACKING SYSTEMS (6 DOF)

6.1 INTRODUCTION

Ingestible medical devices such as wireless endoscopes are finding increasing use in monitoring gastrointestinal track. It has an imaging device fitted inside a pill for diagnostics purposes. Commercial ingestible imaging devices are available [1]-[5].

With the aid of the imaging device, we can determine the existence of the problem source. However, it cannot tell us the accurate location of the problem. Position is required to be correlated with images for monitoring the recovery status.

Most of these devices utilize magnetic field for position and orientation (P&O) determination [6] - [15]. Since the magnetic field penetrates the body without attenuation or change, then the tracking may be continuous. Furthermore, the field is not limited by line-of-sight, which usually required for Optical tracking and Ultrasonic tracking [16].

The motivation of our work is to build a portable Magnetic Tracking System (MTS) for real-time P&O tracking. Our target is to build the user friendly MTS such that the signal source can be around the human body like a "jacket" and the sensor can be fitted inside a "pill" for real time P&O detection.

We design the geometrical shape of the field generating elements such that it can be easily fitted around human body without affecting the patients' regular activities. We also design the small sized field sensing elements to be put inside the capsule. For real-time and accurate P&O detection, we utilize Artificial Neural Networks (ANN) do the computational tasks and utilize Space Mapping (SM) modeling to improve the accuracy of P&O determination.

6.2 3-D PORTABLE MAGNETIC TRACKING IMPLMENTATION

For 3-D MTS, we use 6 primary coils for the field generator and 3 orthogonal secondary coils centered at the same origin for the field sensor. We have 6 unknowns to be determined for the general 6 degrees-of-freedom (6DOF) object, which are 3 position parameters and 3 orientations parameters.

Our design specifications for the 3D tracking system are as follows:

1. A portable magnetic tracking system that does not affect the patient's regular activities.
2. Real-time position tracking.
3. Small sized sensor which can be built inside a "pill".

4. Worst case position error of 10.0 mm and worst case orientation error within 15 deg.

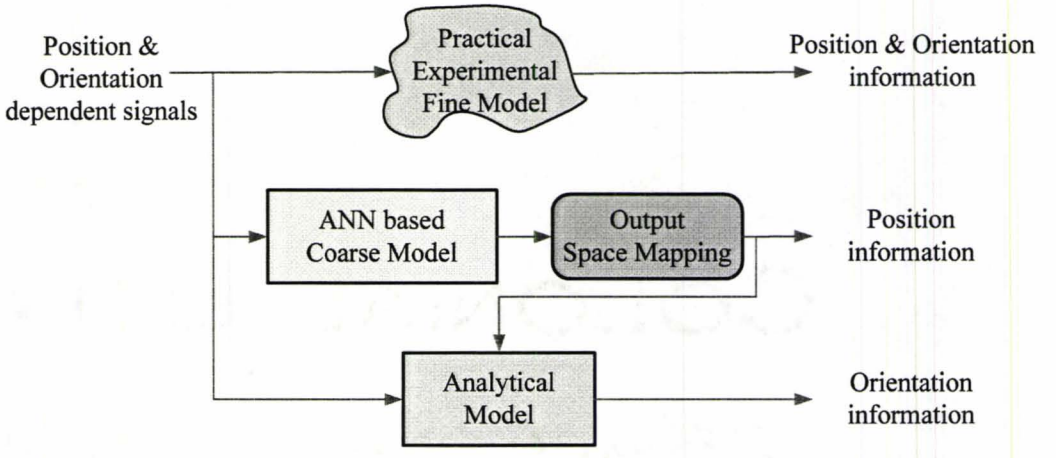

Fig 6.1: Magnetic Tracking Exploiting ANN and SM modeling [17].

The block diagram for the overall MTS is shown in Fig 6.1. The time intensive fine model is replaced by the SM modeling, which includes an ANN- based coarse model for fast computational time and a SM model for accuracy improvement.

6.2.1 Mathematical Formulation

We calculate the magnetic flux by simple dot product instead of integration over vector area because the size of the field sensor is relatively small. For the 3-D case we have (6-1). Here we reproduce the equations (6-1 ~ 6-2) from Chapter 2 for convenience.

$$\boldsymbol{B}_{am} = \mu \oint_{c} \frac{I_{am} d\boldsymbol{L} \times \boldsymbol{R}(x,y,z)}{4\pi R^3(x,y,z)} \tag{6-1}$$

$$emf_{am} = 2\pi f \int_{s} \boldsymbol{B}_{am}(x,y,z) \bullet d\boldsymbol{s}(\phi,\theta,\varphi) \tag{6-2}$$

$$emf_{am} = 2\pi f \boldsymbol{B}_{am}(x,y,z) \bullet \boldsymbol{S}(\phi,\theta,\varphi) \tag{6-3}$$

To solve for the 6 unknown position parameters in a general 6 DOF system, we can follow the same algorithm as shown in 2-D case with minor modifications. We use 3 orthogonal field sensing elements at the same center. In this particular case, we can solve the position and orientation parameters separately, because the magnitude of the $\boldsymbol{B}_{am}$ is independent of orientation parameters.

6.2.1.1 Position Determination

The mathematical relationship between position parameters and the magnitude of magnetic flux density is shown in (6-4).

$$\left\| \boldsymbol{B}_{am}^{c_i}(x,y,z) \right\| = \left[\left(\frac{emf_{am\_x}^{i}}{2\pi f_i I_{am\_i} S_x} \right)^2 + \left(\frac{emf_{am\_y}^{i}}{2\pi f_i I_{am\_i} S_y} \right)^2 + \left(\frac{emf_{am\_z}^{i}}{2\pi f_i I_{am\_i} S_z} \right)^2 \right]^{\frac{1}{2}} \tag{6-4}$$

where $\boldsymbol{B}_{am}^{c_i}$ is the amplitude vector of magnetic flux density due to excitation source c_i (6-1), $emf_{am\_j}^{i}$ is the amplitude of electromotive force measured at sensor number j due to excitation source i, S_j is the area of sensor number j.

To uniquely solve the nonlinear equation (6-4), we create an overdetermined system of 6 independent equations with 3 unknowns as in (6-5). The reason is the same as

our 2-D implementation. By adding 3 additional independent equations, we eliminate the situations such that 2 completely different positions have the same $\boldsymbol{B}_{am}^{mag}$ signals:

$$\boldsymbol{B}_{am}^{mag} = \left[\left\| \boldsymbol{B}_{am}^{c_1} \right\| \quad \left\| \boldsymbol{B}_{am}^{c_2} \right\| \quad \left\| \boldsymbol{B}_{am}^{c_3} \right\| \quad \left\| \boldsymbol{B}_{am}^{c_4} \right\| \quad \left\| \boldsymbol{B}_{am}^{c_5} \right\| \quad \left\| \boldsymbol{B}_{am}^{c_6} \right\| \right]^T \tag{6-5}$$

where $\left\| \boldsymbol{B}_{am}^{c_i} \right\|$ is defined in (6-4)

The position can be determined by a parameter extraction (PE) process, which iteratively update x, y and z to match the observation vector $\boldsymbol{B}_{am}^{mag\_ob}$ (6-6):

$$\boldsymbol{x}^* = \arg\left\{ \min_{\boldsymbol{x}} \left\| \underbrace{\boldsymbol{B}_{am}^{mag\_ob}}_{\substack{\text{given observation} \\ \text{at unknown position}}} - \boldsymbol{B}_{am}^{mag}(\boldsymbol{x}) \right\|^2 \right\} \tag{6-6}$$

$$\text{where } \boldsymbol{x} = \begin{bmatrix} x & y & z \end{bmatrix}^T$$

6.2.1.2 Orientation Determination

Once we have determined the position parameters of the field sensor, orientation can be determined analytically. At a given position, we assume that our field sensor has an arbitrary orientation with normal vector:

$$\begin{bmatrix} \boldsymbol{n}_x & \boldsymbol{n}_y & \boldsymbol{n}_z \end{bmatrix} = \begin{bmatrix} a_{11} & a_{12} & a_{13} \\ a_{21} & a_{22} & a_{23} \\ a_{31} & a_{32} & a_{33} \end{bmatrix} \tag{6-7}$$

Based on the excitation and observation pairs, we have the following equations:

$$\underbrace{\boldsymbol{B}_1^a}_{\substack{\text{excitation}\\ \text{source\#1}}} \cdot \underbrace{\boldsymbol{n}_x}_{\text{sensor coil } x} = \underbrace{B_{1x}^m}_{\substack{\text{measurement}\\ \text{at coil } x}} \tag{6-8}$$

$$\begin{bmatrix} B_{1x}^a & B_{1y}^a & B_{1z}^a \\ B_{3x}^a & B_{3y}^a & B_{3z}^a \\ B_{5x}^a & B_{5y}^a & B_{5z}^a \end{bmatrix} \begin{bmatrix} a_{11} \\ a_{21} \\ a_{31} \end{bmatrix} = \begin{bmatrix} B_{1x}^m \\ B_{3x}^m \\ B_{5x}^m \end{bmatrix} \tag{6-9}$$

$$\boldsymbol{n}_x = \begin{bmatrix} a_{11} \\ a_{21} \\ a_{31} \end{bmatrix} = \begin{bmatrix} B_{1x}^a & B_{1y}^a & B_{1z}^a \\ B_{3x}^a & B_{3y}^a & B_{3z}^a \\ B_{5x}^a & B_{5y}^a & B_{5z}^a \end{bmatrix}^{-1} \begin{bmatrix} B_{1x}^m \\ B_{3x}^m \\ B_{5x}^m \end{bmatrix} \tag{6-10}$$

where superscript '*a*' denotes the analytical value at the given position, the superscript '*m*' denotes the measurement value at the given position, and the subscripts 1, 2, 3 denote the source excitation due to different primary coils. Also, in (6-10), the subscripts *x*, *y*, *z* denote the value obtained from different labeled sensor coils. The normal vectors $\boldsymbol{n}_y$ and $\boldsymbol{n}_z$ can be determined by the same procedure as in (6-8) ~ (6-10). Here some elements in (6-7) are redundant since the column vectors in orientation matrix (6-7) must be an orthonormal set.

Without assuming the orthonormality of (6-7), we solve each 1 of the 9 elements independently to avoid the accumulation of error from previous calculations. More importantly, we can use the interrelated dependency to check whether our calculations are accurate or not. More details on this approach will be presented later in details with examples.

TABLE 6.1:
SETUP OF 3-D TRACKING SYSTEMS

	field generator	field sensor
	coil #1 ~ #6	coil #X ~ #Z
excitation frequency	2 kHz	NA
number of turns	21	100
wire type	AWG 24	AWG 34

"NA" is defined as not applicable.

6.2.2 Field Generator

For field generating elements, we use 6 primary coils around the side of a cylinder (Fig. 6.2). Different spatial configurations represent different excitation sources as in (6-1 and 6-4). Different excitation source means different line integral path (6-1) for magnetic flux density $\boldsymbol{B}$ calculation. The number of turns for each coil is shown in TABLE 6.1.

Similar to the 2D magnetic tracking system, we aim at satisfying two main purposes of selecting this field generator geometry (Fig. 6.2). The first purpose is to fit around the patient's stomach area. The second purpose is to create a unique magnetic at each point in the region of interest. The more distinct the field distribution, the more independent the equations (6-5) become. This will likely improve the uniqueness of the obtained solution. In addition, the distinct field distribution will result in relatively high signal sensitivities with respect to position change. The higher the sensitivities, the better ANN model performance. More details will be given in the following section.

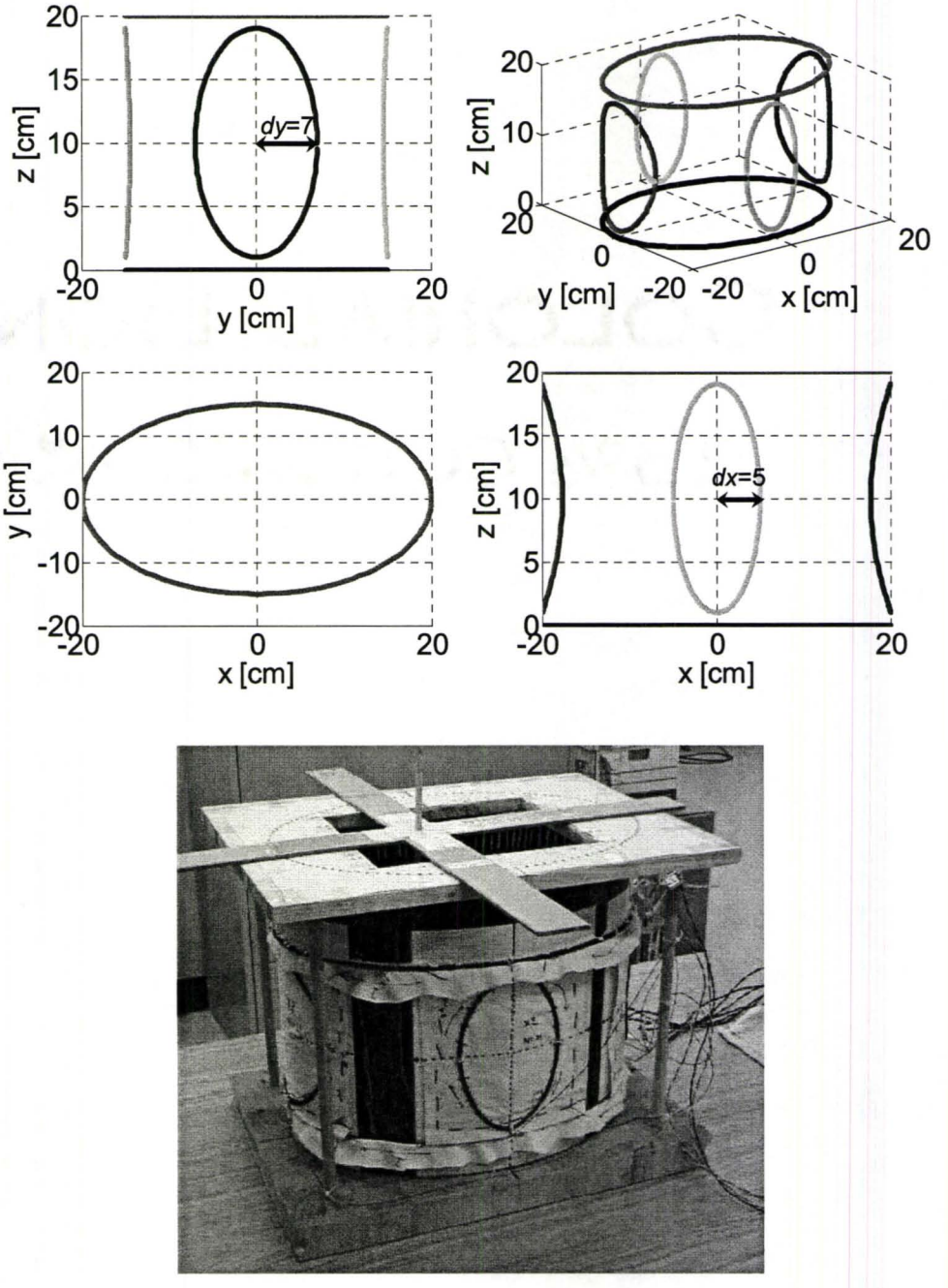

Fig 6.2: Field generator's spatial configuration.

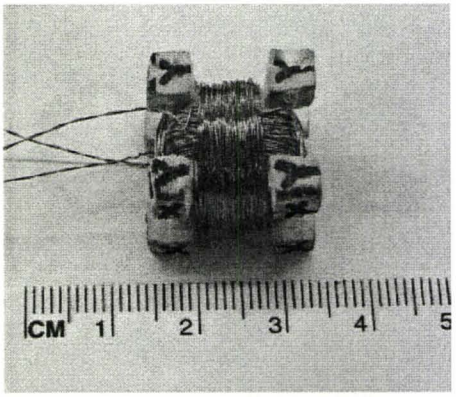

Fig 6.3: Field sensor for 3-D Magnetic Tracking Systems.

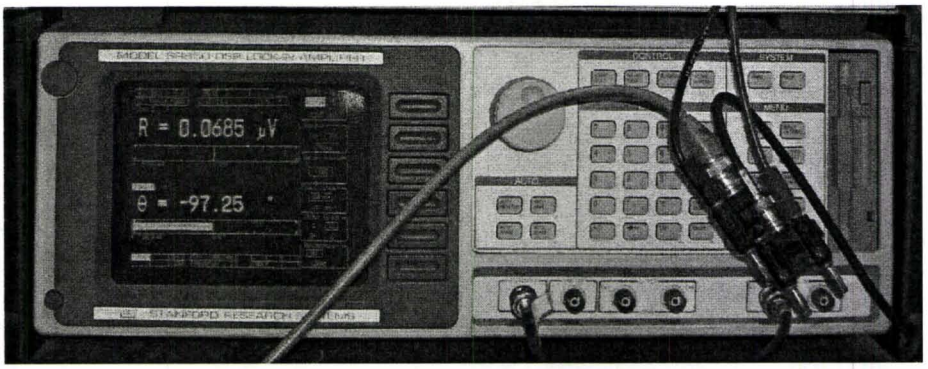

Fig 6.4: Lock-in Amplifier SR850 [18].

Fig 6.5: Digital Multimeter 3478A [19].

We excite the primary coils with pure sinusoidal current using a function generator (Hewlett-Packard 3325B). Each coil can have its own frequency to enable the separation of the excitation $\boldsymbol{B}_{am}^{c_i}$ and the corresponding $emf_{am\_j}^{i}$ pairs by filtering. Because of the limited quantities of instruments, we cannot measure 18 independent emf_{am} signals simultaneously. Instead, we excite the primary coils one by one and measure its corresponding emf_{am} signal. We arbitrarily choose frequency 2.0 kHz and 21 turns for all the primary coils (TABLE 6.1).

6.2.3 Field Sensor

For our field sensor, we use 3 orthogonal squared loops with side length of 1.2 cm and 100 turns (Fig. 6.3 and TABLE 6.1). The induced $emf_{am\_j}^{i}$ signal is measured by Lock-in Amplifier SR850 [18] (Stanford Research Systems Fig. 6.4). The AC excitation current amplitude is measured by a Digital Multimeter 3478A [19] (Hewlett-Packard Fig. 6.5). We measure different excitation ($\boldsymbol{B}_{am}^{c_i}$) and observation ($emf_{am\_j}^{i}$) pairs by changing excitation coils and sensor coils input for the lock-in amplifier. We utilize 2 rotary swatches to control which field generating element to be excited and which sensing element to be used for corresponding signal measurement (Figs. 6.6, 6.7).

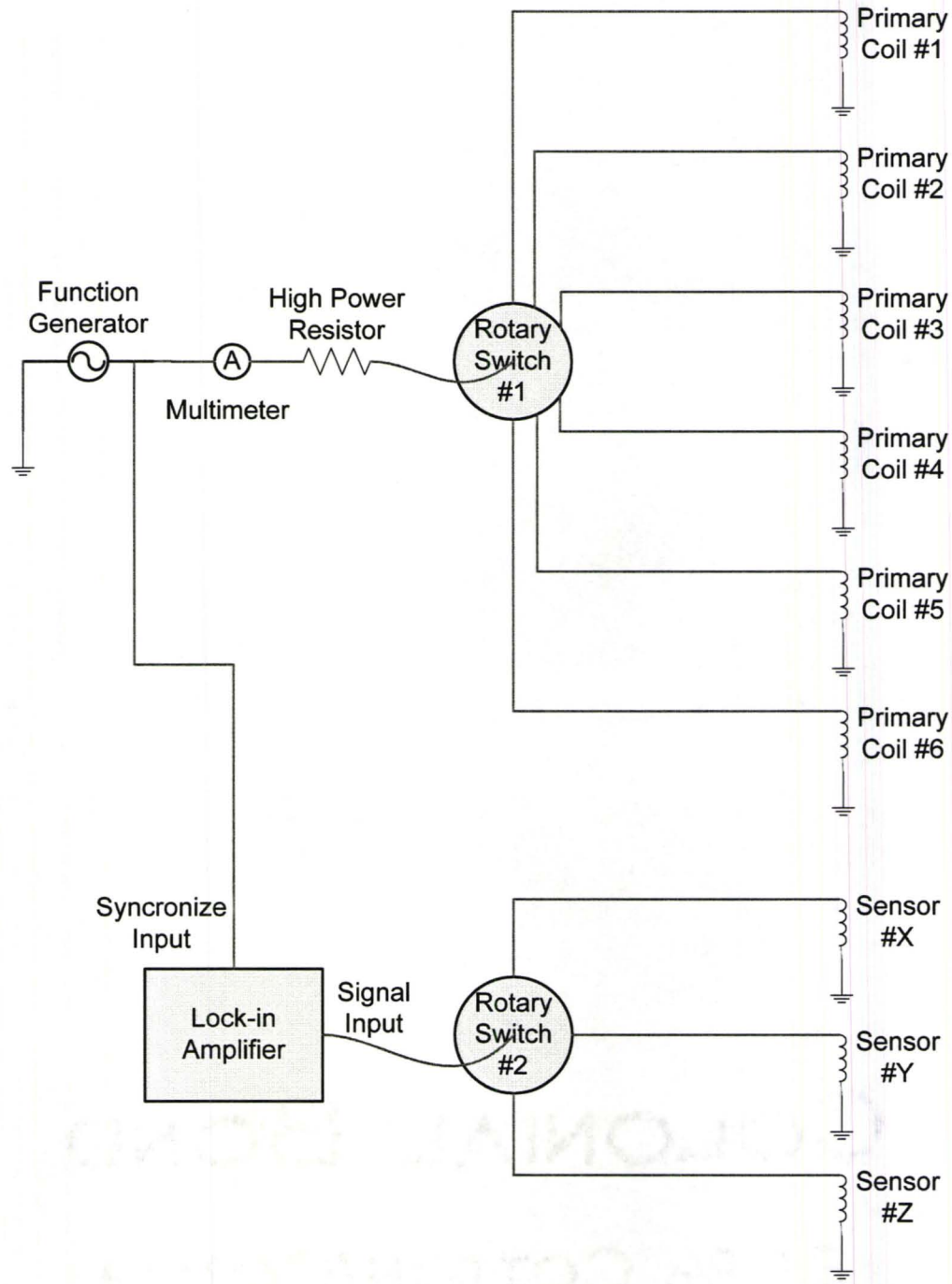

Fig 6.6: The overall experimental setup for the 3D magnetic tracking system.

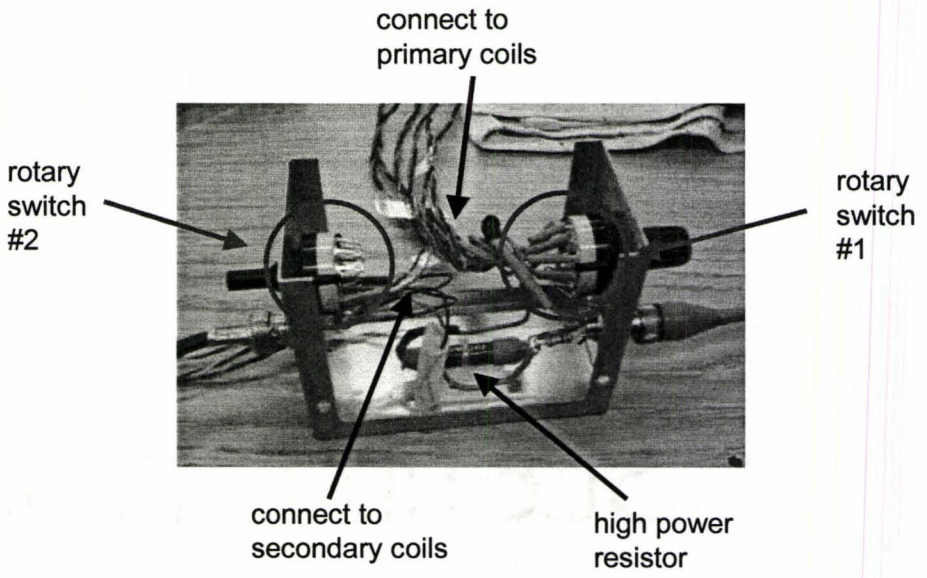

Fig 6.7: Excitation and observation pair control circuit.

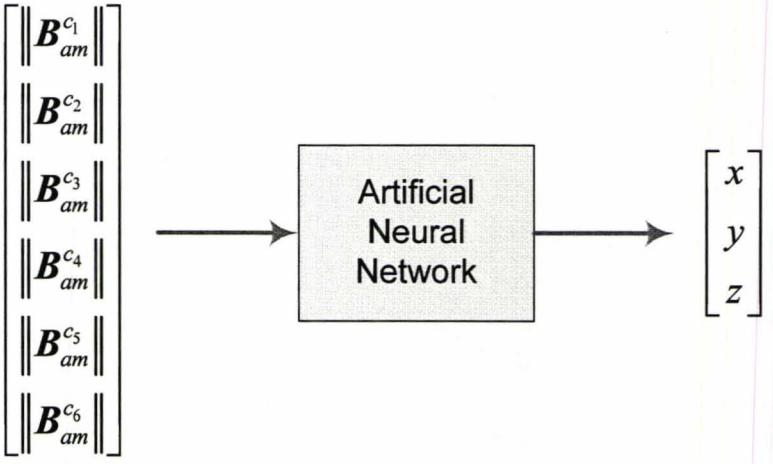

Fig 6.8: The Artificial Neural Network (ANN) model.

6.2.4 Signal Processing Unit Exploiting ANN

Our signal processing is a MatLab [20] based program that extracts the position parameters using $\boldsymbol{B}_{am}^{mag}$ (6-5). This PE process is carried out iteratively for each set of measurements $\boldsymbol{B}_{am}^{mag}$.

To avoid this time consuming PE process and achieve real-time position detection, we train an ANN [21]-[22] to model the mapping between $\boldsymbol{B}_{am}^{mag}$ and its corresponding position parameters $[x\ y\ z]$ (see Fig. 6.8).

This ANN is trained through analytical computer simulations exploiting (6-1 ~ 6-6). The region of interest is fixed at:

$$\begin{cases} x \in [-10\ cm \quad +10\ cm] \\ y \in [-10\ cm \quad +10\ cm] \\ z \in [0\ cm \quad +20\ cm] \end{cases} \tag{6-11}$$

The training data set is a $2.0\ cm \times 2.0\ cm \times 2.0\ cm$ mesh grid uniformly spread over the observation region (6-11) and testing data set is a $1.0\ cm \times 1.0\ cm \times 1.0\ cm$ mesh grid (Fig. 6.9). The 3-D training and testing data set is a 3-D version of Fig. 6.9 in the region of interest (6-11), which is reproduced from Chapter 5 for convenience.

Each 3-D position $\begin{bmatrix} x & y & z \end{bmatrix}^T$ in the training data set is correlated with its corresponding $\boldsymbol{B}_{am}^{mag}$ input through the training process. The ANN should be able to determine the correct output $\begin{bmatrix} x & y & z \end{bmatrix}^T$ when the corresponding $\boldsymbol{B}_{am}^{mag}$ signal is presented at the ANN input. Testing data set is used to evaluate the performance of the

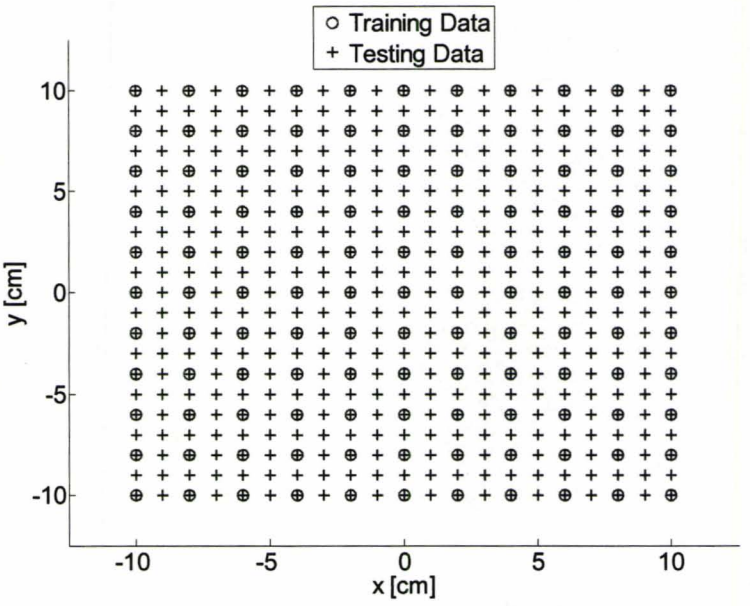

Fig 6.9: ANN training and testing data set (2-D version).

ANN model. An ANN model is good only when it is able to give correct position when corresponding signal from testing data set is given.

In this experiment, the ANN is trained using the software ***NeuroModeler*** [23]. A three layers ANN structure is used (Fig. 6.10). The training options are given in TABLE 6.2.

We start with a small number of hidden neurons (2 in our case) and keep adding hidden neurons to achieve the best ANN performance. The number of hidden neurons is proportional to the complexity of the problem.

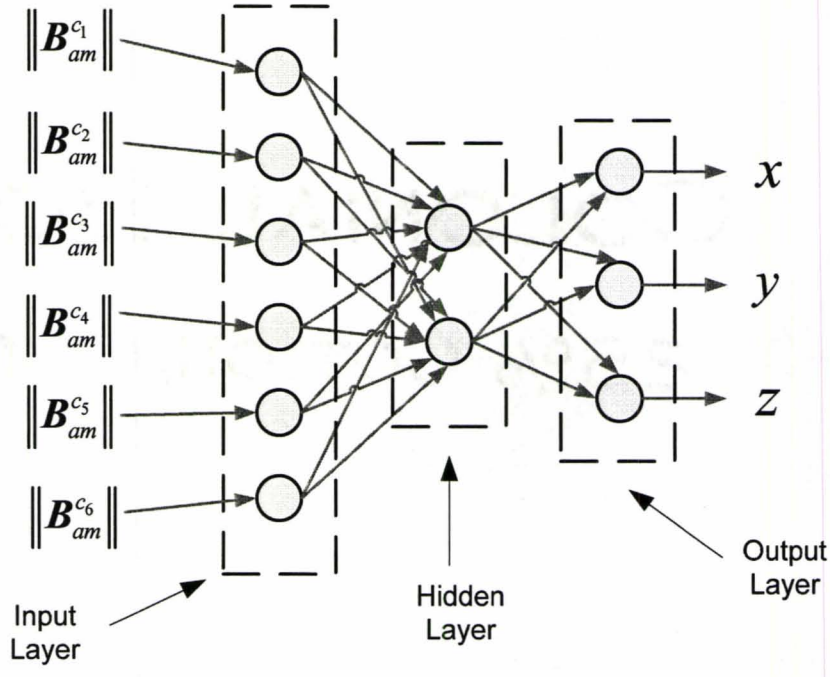

Fig 6.10: The ANN structure used for 3-D magnetic tracking system.

TABLE 6.2:
ANN MODEL TRAINGING OPTIONS

Training Method	Quasi-Newton (MLP)
Max. No. Epochs	494
Error Tolerance	0.0
Hessian Refresh Interval	500
Max Step Size	10.0
Model Parameter Tolerance	0.0

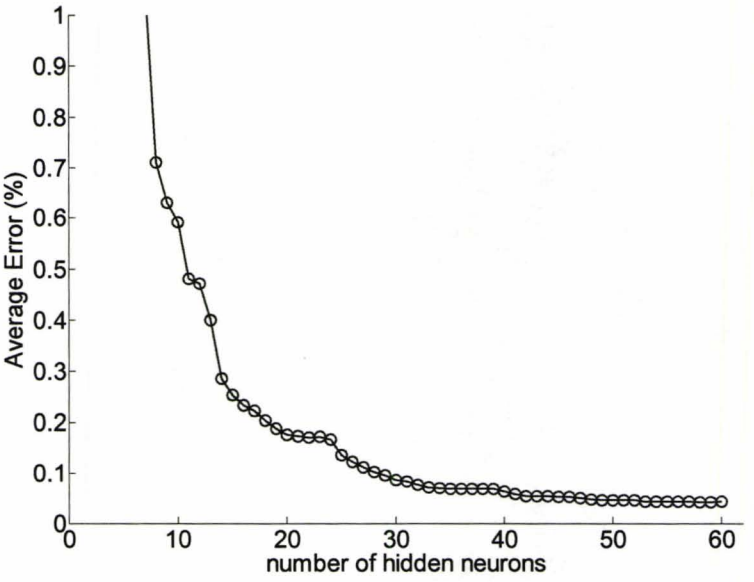

Fig 6.11: Average ANN training error.

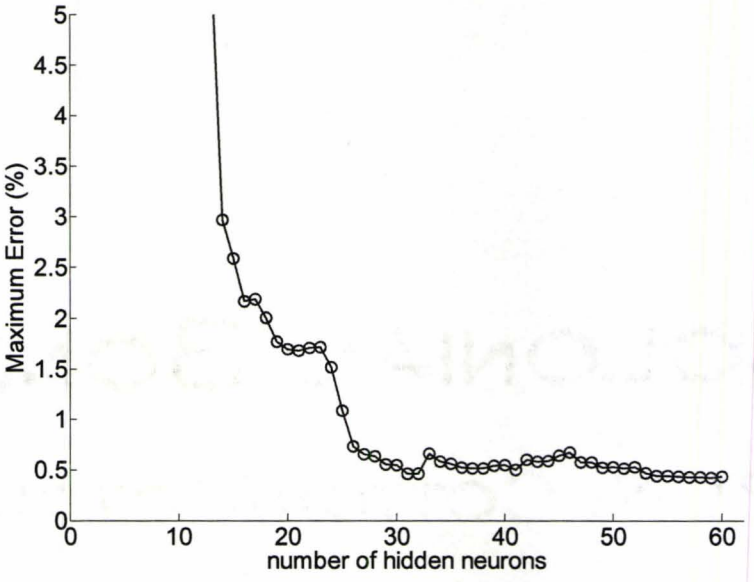

Fig 6.12: Maximum ANN training error.

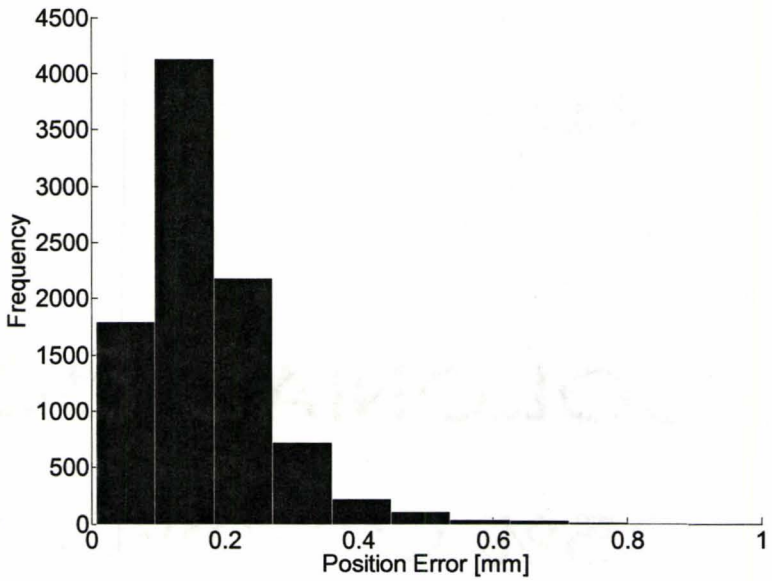

Fig 6.13: Position error histogram of ANN with theoretical $\boldsymbol{B}_{am}^{mag}$ input.

TABLE 6.3:
STATISTICAL POSITION ERROR

	ANN response
Number of points	9261
Mean [mm]	0.2
Max [mm]	0.9
Standard deviation [mm]	0.1
Range [mm]	0.9

Position error is defined as the l_2 norm of the difference between exact position and the ANN output position.

TABLE 6.4:
POSITION ERROR COMPARISON FOR DIFFERENT GEOMETRICAL SHAPES

geometrical shape	number of hidden neurons	mean [mm]	max [mm]	standard deviation	range
$dx = 14$ and $dy = 9$	26	0.38	4.49	0.27	4.48
$dx = 14$ and $dy = 5$	56	0.14	1.56	0.10	1.55
$dx = 12$ and $dy = 5$	21	0.71	3.07	0.39	3.05
$dx = 10$ and $dy = 5$	47	0.32	2.56	0.22	2.58
$dx = 7$ and $dy = 5$	52	0.26	2.08	0.17	2.07
$dx = 5$ and $dy = 5$	51	0.30	1.10	0.15	1.09
$dx = 5$ and $dy = 7$	**59**	**0.17**	**0.89**	**0.10**	**0.88**
$dx = 5$ and $dy = 9$	39	0.23	0.93	0.13	0.93

Position error is defined as the l_2 norm of the difference between exact position and the ANN output position.

By observing the error plots vs. number of hidden neurons (Fig. 6.11 to Fig. 6.12), we conclude that a good ANN model performance is obtained when the number of hidden neurons is greater than 53. We thus decide to use 59 hidden neurons for our 3-D MTS.

After training the ANN with the theoretical input-output pairs, the ANN is able to recognize the patterns and output the position accurately (Fig. 6.13 and TABLE 6.3).

The position error histogram (Fig. 6.13) shows that the majority position error is less than 0.5 mm and the maximum error is around 0.8 mm. Good position match is obtained theoretically.

For different geometrical shapes (*dx* and *dy* in Fig. 6.2) of the field generating elements, the best ANN model performance we can get is different (TABLE 6.4). The geometry parameters in bold are selected for our 3-D implementation. The number of samples is 9261 for all the cases.

Experimentally, we measure the position defined signal $\boldsymbol{B}_{am}^{mag\_ob}$. The average relative error is 8.37 % with maximum error of 28.95 % taking the theoretical $\boldsymbol{B}_{am}^{mag}$ as reference. The error is mainly caused by the environmental interferences from nearby conducting materials. The magnetic field induces the current in the conducting materials. The induced current generates its own magnetic field which affects the original magnetic field in return.

Because of the measurements errors in $\boldsymbol{B}_{am}^{mag\_ob}$, the position responses from the ANN model have relatively large errors (Fig 6.14 and TABLE 6.5). The position error histogram (Fig 6.14) shows that the majority error is centered around 25 mm and the maximum error is around 50 mm.

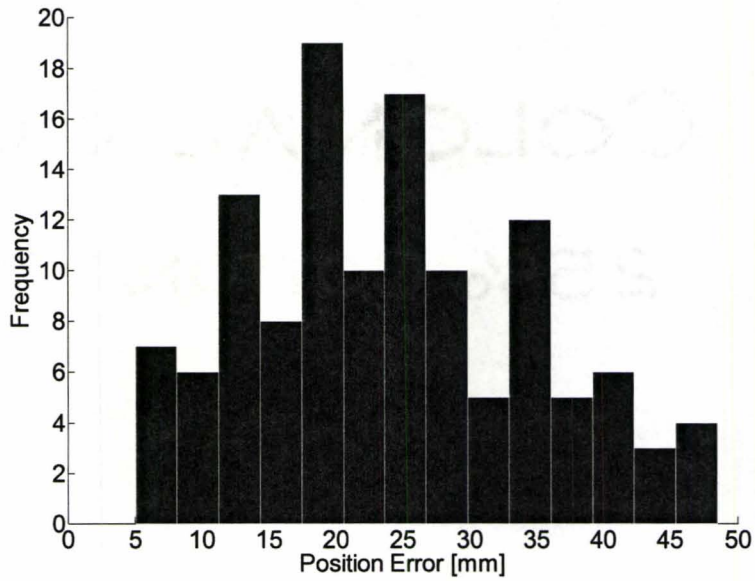

Fig 6.14: Position error histogram of ANN with experimental $\boldsymbol{B}_{am}^{mag\_ob}$ input.

TABLE 6.5:
EXPERIMENTAL STATISTICAL POSITION ERROR

	ANN response
Number of points	125
Mean [mm]	24.1
Max [mm]	48.5
Standard deviation [mm]	10.6
Range [mm]	43.5

Position error is defined as the l_2 norm of the difference between exact position and the ANN output position.

6.2.5 System Calibration Exploiting SM Modeling

To improve the accuracy of the position responses, we utilize system calibration exploiting the SM concept. The trained ANN represents a course model as in Fig. 6.1. It predicts the correct position accurately only using theoretical $\boldsymbol{B}_{am}^{mag}$ inputs. In reality, measured $\boldsymbol{B}_{am}^{mag\_ob}$ values do not match the theoretical values $\boldsymbol{B}_{am}^{mag}$ due to the interference of other magnetic sources, the presence of nearby conducting materials, or the inaccuracies in modeling the primary coils and the secondary coils. To make accurate measurements, we put the tracking system far away from other magnetic sources and keep the geometrical shape of the built magnetic field system as close as possible to the configurations used in the ideal magnetic field simulations.

6.2.5.1 Position Calibration

To correct the position offset, we apply system calibration by mapping the ANN output position to the actual position. We utilize minimum mapping parameters for position calibration. A simple linear output mapping (6-12) is assumed between the actual position and the ANN's predicted position.

$$\begin{bmatrix} x \\ y \\ z \end{bmatrix}_{\text{actual position}} = \begin{bmatrix} a_{11} & a_{12} & a_{13} \\ a_{21} & a_{22} & a_{23} \\ a_{31} & a_{32} & a_{33} \end{bmatrix} \begin{bmatrix} x \\ y \\ z \end{bmatrix}_{\text{ANNs response}} + \begin{bmatrix} b_{11} \\ b_{21} \\ b_{31} \end{bmatrix} \tag{6-12}$$

We also utilize minimum points to find the mapping parameters. We select 27 points out of 125 for mapping parameters determination (Fig. 6.15). The selected samples

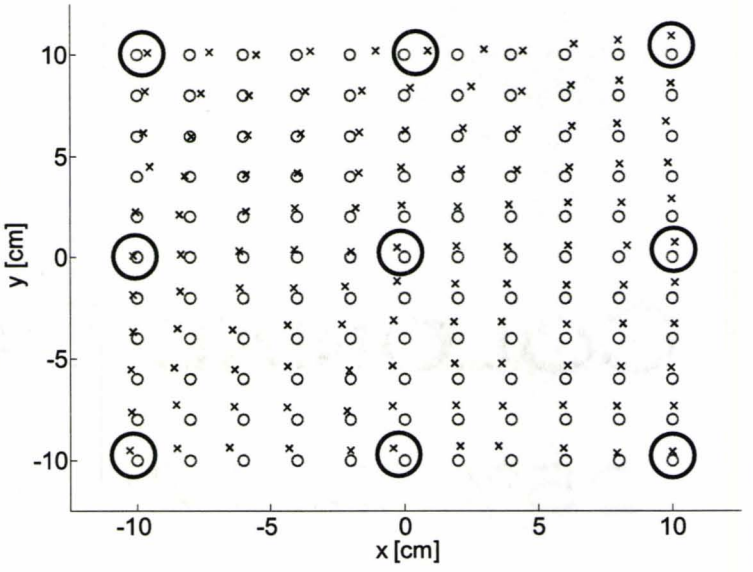

Fig 6.15: Selected calibration points as labeled with big black circle (2-D version).

TABLE 6.6:
PARAMETER EXTRACTION OPTIONS

options	values
optimization functions	fminimax
options.MaxIter	500
options.MaxFunEvals	2000
options.TolFun	10^{-6}
options.TolX	10^{-8}
options.DiffMaxChange	10^{-1}
options.DiffMinChange	10^{-8}

are the 3-D version of Fig. 6.15 in the region of interest (6-11), which is reproduced from Chapter 5 for convenience.

After carrying out the PE process, we optimize the mapping parameters and establish the position calibration formula (6-13).

$$\begin{bmatrix} x \\ y \\ z \end{bmatrix}_{\text{actual position}} = \begin{bmatrix} 0.9685 & -0.0082 & -0.0340 \\ -0.0167 & 0.9087 & -0.0404 \\ -0.0253 & -0.0152 & 0.7876 \end{bmatrix} \begin{bmatrix} x \\ y \\ z \end{bmatrix}_{\text{ANNs response}} + \begin{bmatrix} 1.1686 \\ 0.5651 \\ 1.0935 \end{bmatrix} \tag{6-13}$$

It should be noted that the positions x, y and z are in centimetres.

This PE is implemented in a MatLab [20] with the options shown in TABLE 6.6. The starting point is shown in (6-14). The objective function is defined as (6-15 to 6-17) for all the sample points (27 points in this case).

$$\begin{bmatrix} a_{11} & a_{12} & a_{13} \\ a_{21} & a_{22} & a_{23} \\ a_{31} & a_{32} & a_{33} \end{bmatrix} = \begin{bmatrix} 1 & 0 & 0 \\ 0 & 1 & 0 \\ 0 & 0 & 1 \end{bmatrix} \text{ and } \begin{bmatrix} b_{11} \\ b_{21} \\ b_{31} \end{bmatrix} = \begin{bmatrix} 0 \\ 0 \\ 0 \end{bmatrix} \tag{6-14}$$

$$f(a_{11}, a_{12}, a_{13}, b_{11}) = \begin{bmatrix} \left| \begin{bmatrix} a_{11} & a_{12} & a_{13} \end{bmatrix} \times \begin{bmatrix} x_1 \\ y_1 \\ z_1 \end{bmatrix}_{ANN} + b_{11} - [x_1]_{actual} \right| \\ \left| \begin{bmatrix} a_{11} & a_{12} & a_{13} \end{bmatrix} \times \begin{bmatrix} x_2 \\ y_2 \\ z_2 \end{bmatrix}_{ANN} + b_{11} - [x_2]_{actual} \right| \\ \vdots \\ \left| \begin{bmatrix} a_{11} & a_{12} & a_{13} \end{bmatrix} \times \begin{bmatrix} x_{27} \\ y_{27} \\ z_{27} \end{bmatrix}_{ANN} + b_{11} - [x_{27}]_{actual} \right| \end{bmatrix} \tag{6-15}$$

$$f(a_{21},a_{22},a_{23},b_{21})=\begin{bmatrix}\left|\begin{bmatrix}a_{21} & a_{22} & a_{23}\end{bmatrix}\times\begin{bmatrix}x_1\\y_1\\z_1\end{bmatrix}_{ANN}+b_{21}-[y_1]_{actual}\right|\\ \left|\begin{bmatrix}a_{21} & a_{22} & a_{23}\end{bmatrix}\times\begin{bmatrix}x_2\\y_2\\z_2\end{bmatrix}_{ANN}+b_{21}-[y_2]_{actual}\right|\\ \vdots\\ \left|\begin{bmatrix}a_{21} & a_{22} & a_{23}\end{bmatrix}\times\begin{bmatrix}x_{27}\\y_{27}\\z_{27}\end{bmatrix}_{ANN}+b_{21}-[y_{27}]_{actual}\right|\end{bmatrix} \tag{6-16}$$

$$f(a_{31},a_{32},a_{33},b_{31})=\begin{bmatrix}\left|\begin{bmatrix}a_{31} & a_{32} & a_{33}\end{bmatrix}\times\begin{bmatrix}x_1\\y_1\\z_1\end{bmatrix}_{ANN}+b_{31}-[z_1]_{actual}\right|\\ \left|\begin{bmatrix}a_{31} & a_{32} & a_{33}\end{bmatrix}\times\begin{bmatrix}x_2\\y_2\\z_2\end{bmatrix}_{ANN}+b_{31}-[z_2]_{actual}\right|\\ \vdots\\ \left|\begin{bmatrix}a_{31} & a_{32} & a_{33}\end{bmatrix}\times\begin{bmatrix}x_{27}\\y_{27}\\z_{27}\end{bmatrix}_{ANN}+b_{31}-[z_{27}]_{actual}\right|\end{bmatrix} \tag{6-17}$$

Finally, we apply this calibration formula for the rest of position responses obtained from the ANN. We can see that the accuracy is improved statistically and graphically (Fig. 6.16 and TABLE 6.7).

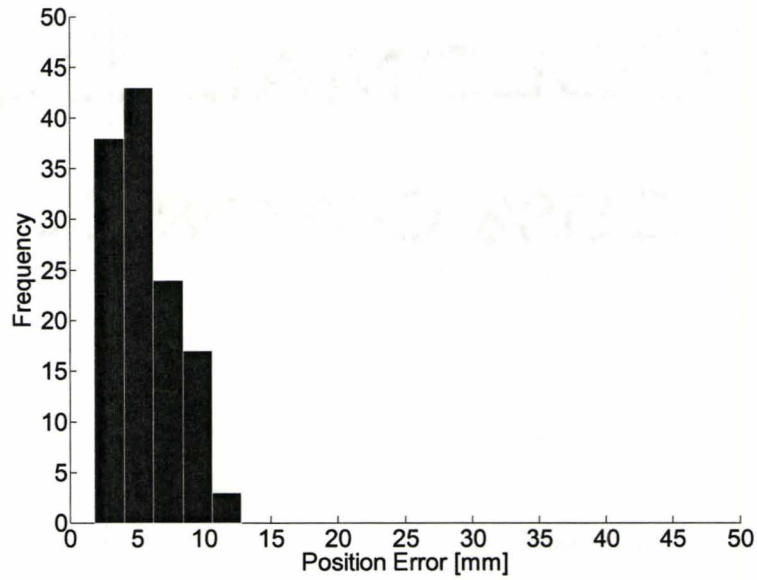

Fig 6.16: Position error histogram after position calibration.

TABLE 6.7:
STATISTICAL POSITION ERROR COMPARISON

	before calibration	after calibration
Number of points	125	125
Mean [mm]	24.1	5.6
Max [mm]	48.5	12.8
Standard deviation [mm]	10.6	2.4
Range [mm]	43.5	10.9

Position error is defined as the l_2 norm of the difference between exact position and the ANN output position.

6.2.5.2 Orientation Calibration

Take analytical calculation of $\boldsymbol{n}_x$ for example (6-10), originally analytical B_{ij}^a is calculated at the given position before position calibration is applied. In addition, the accuracy of the orientation vector $\boldsymbol{n}_x$ is affected by the magnitude $\left\|\boldsymbol{B}_i^m\right\|$ from experiments. In order to improve the accuracy of the orientation determination, we take the calibrated position for B_{ij}^a calculation with adjusted coefficient of B_{ij}^m as in (6-18). The results are shown in Fig. 6.17 ~ Fig. 6.18 and error is defined in (6-19).

$$\boldsymbol{n}_x^m = \begin{bmatrix} a_{11} \\ a_{21} \\ a_{31} \end{bmatrix} = \begin{bmatrix} B_{1x}^a & B_{1y}^a & B_{1z}^a \\ B_{3x}^a & B_{3y}^a & B_{3z}^a \\ B_{5x}^a & B_{5y}^a & B_{5z}^a \end{bmatrix}^{-1} \begin{bmatrix} \dfrac{\boldsymbol{B}_1^a}{\left\|\boldsymbol{B}_1^m\right\|} B_{1x}^m \\ \dfrac{\boldsymbol{B}_3^a}{\left\|\boldsymbol{B}_3^m\right\|} B_{3x}^m \\ \dfrac{\boldsymbol{B}_5^a}{\left\|\boldsymbol{B}_5^m\right\|} B_{5x}^m \end{bmatrix} \tag{6-18}$$

$$\boldsymbol{n}_x^{err}\ [deg] = \cos^{-1}\left(\frac{\boldsymbol{n}_x^a}{\boldsymbol{n}_x^a} \bullet \frac{\boldsymbol{n}_x^m}{\left\|\boldsymbol{n}_x^m\right\|}\right) \tag{6-19}$$

where $\boldsymbol{n}_x^a$ is the actual orientation vector of sensing element x, and $\boldsymbol{n}_x^m$ is the experimental orientation vector of sensing element x calculated base on our MTS algorithm.

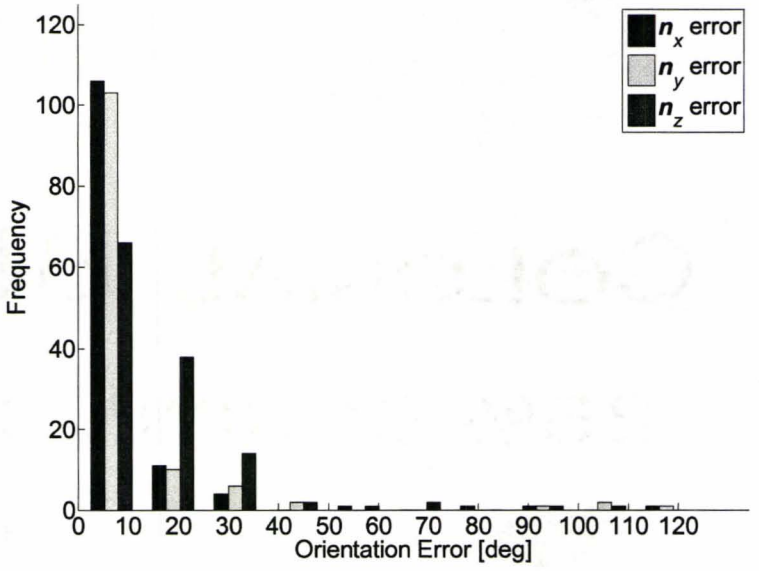

Fig 6.17: Orientation error histogram before orientation calibration.

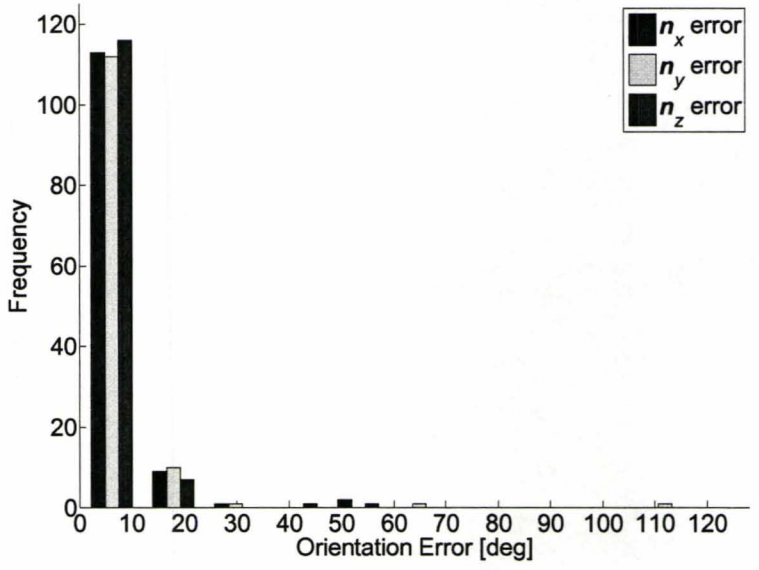

Fig 6.18: Orientation error histogram after orientation calibration.

6.2.5.3 Orientation Validation

In Fig. 6.18, the maximum orientation error is over 110 degrees, which is unacceptable. We want to investigate whether the determined orientation is accurate enough or not without even having the actual orientation. This is feasible and the reason is as the following.

In the orientation calculation process, we do not assume any interdependency of the orientation matrix as in 6-7. Each one of these vectors is orthogonal to the others and has a unity magnitude. Experimentally, some of these orientation vectors can be accurate and some of them are not.

We utilize the interdependency to "flag" the unacceptable resulting orientation vector. We define a quality factor (6-21):

$$\begin{aligned} \boldsymbol{n}_{xy}^{val}\ [deg] &= \cos^{-1}\left(\frac{\boldsymbol{n}_x^m}{\|\boldsymbol{n}_x^m\|} \bullet \frac{\boldsymbol{n}_y^m}{\|\boldsymbol{n}_y^m\|}\right) \\ \boldsymbol{n}_{yz}^{val}\ [deg] &= \cos^{-1}\left(\frac{\boldsymbol{n}_y^m}{\|\boldsymbol{n}_y^m\|} \bullet \frac{\boldsymbol{n}_z^m}{\|\boldsymbol{n}_z^m\|}\right) \\ \boldsymbol{n}_{zx}^{val}\ [deg] &= \cos^{-1}\left(\frac{\boldsymbol{n}_z^m}{\|\boldsymbol{n}_z^m\|} \bullet \frac{\boldsymbol{n}_x^m}{\|\boldsymbol{n}_x^m\|}\right) \end{aligned} \tag{6-20}$$

$$QF = \left|90^0 - \boldsymbol{n}_{xy}^{val}\right| + \left|90^0 - \boldsymbol{n}_{yz}^{val}\right| + \left|90^0 - \boldsymbol{n}_{zx}^{val}\right| \tag{6-21}$$

Here we evaluate the quality factor from experimental measurements only. In this case, we know whether the orientation measurements are good or not in advance without knowing the actual orientation.

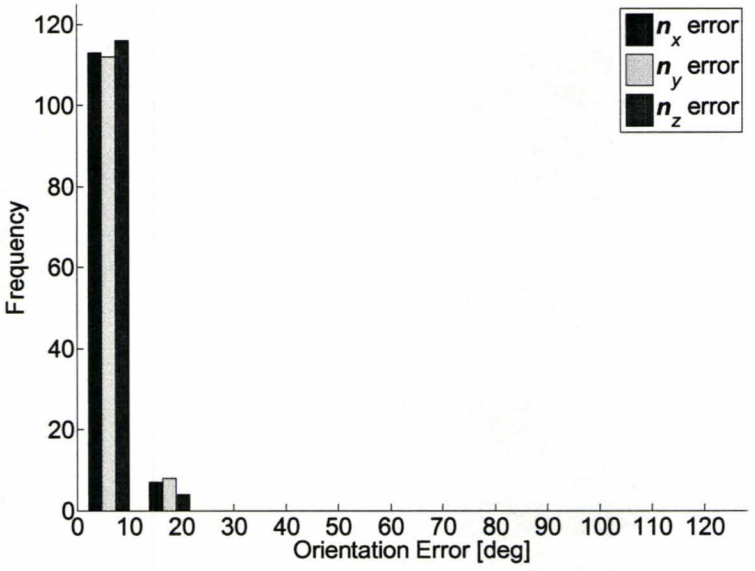

Fig 6.19: Orientation error histogram with quality factor applied.

We set our orientation tolerance as 15 degrees for each sensor coil and "mark" the unacceptable orientation measurements as in (6-22).

$$\begin{cases} if & QF < 3\times 15^0 \quad acceptable \\ else & QF \geq 3\times 15^0 \quad unacceptable \end{cases} \tag{6-22}$$

After applying quality factor and get rid of the unacceptable orientation samples, we have the Fig. 6.19.

6.3 EFFICIENCY OF 3-D PORTABLE MAGNETIC TRACKING SYSTEMS

Our 3-D MTS utilizes ANN for real-time P&O detection and SM modeling for accuracy improvements. The ANN significantly speeds up P&O determination process and release the "bottleneck" of the overall tracking performance. SM modeling improves the accuracy of the P&O responses in a cost-benefit-efficient manner.

6.3.1 Artificial Neural Networks

For real-time P&O tracking, we use the ANN model as our signal processing unit. The functionality of the ANN model is the PE process of position information $[x \quad y \quad z]^T$ from experimental signal $\boldsymbol{B}_{am}^{mag\_ob}$ (6-6).

By comparing the ANN model implemented PE with traditional PE process we have the followings pros and cons:

Pros:

1. Extremely fast in terms of computational time.
2. Starting point independent.
3. Global minimum convergence.
4. Straight computation, no iterative process.

Cons:

1. Requires time consuming training process (TABLE 6.8).
2. Accuracy is guaranteed only in the region of interest.

TABLE 6.8:
COMPUTATIONAL TIME COMPARISON

	PE	ANN
Number of samples	200	200
Computational time	80 min	1.3 sec
number of local minimum	9	NA
Training time	NA	5 hr 18 min

TABLE 6.9:
3-D POSITION EXTRACTION OPTIONS

options	values
optimization functions	fmincon
lower bound [cm]	[-10 -10 0]
upper bound [cm]	[10 10 20]
objective function	$\left\|\boldsymbol{B}_{am}^{mag\_ob} - \boldsymbol{B}_{am}^{mag}\right\|^2$
options.MaxIter	10^2
options.MaxFunEvals	5×10^2
options.TolFun	10^{-8}
options.TolX	10^{-10}
options.DiffMaxChange	10^{-1}
options.DiffMinChange	10^{-8}
options.TolCon	10^{-8}

The ANN is a continuous model in the region of interest. The inputs of the ANN are the position dependent signals $\boldsymbol{B}_{am}^{mag\_ob}$ from field sensor and the outputs are the 3-D position $[x \quad y \quad z]^T$ of the field sensor relative to field generator.

The computational times for both the ANN model and traditional PE is shown in TABLE 6.8. The PE options are shown in TABLE 6.9. The ANN is suitable for applications to real-time computational tasks because of its short computational time.

6.3.2 Space Mapping Modeling

To improve the accuracy of the MTS, we utilized ANN-based coarse model and Output SM (Fig. 6.1 and 6-12).

Our coarse model is the PE process of 3-D position from $\boldsymbol{B}_{am}^{mag\_ob}$ signals (6-6) based on the ideal case of Faraday's induction law. Our fine model is the PE process based on the practical case of Faraday's induction law. It takes the environmental interferences mostly caused by nearby conducting materials and manufacturing errors of the setup into account. These parameters are complicated to be modeled mathematically.

To achieve fast and accurate position tracking simultaneously, we utilized ANN-based coarse model with Output SM instead of complex fine model development. As a result, we avoid the time consuming fine model development and achieve the same degree of accuracy of P&O responses.

Here, the position calibration is dependent on the environment. We have to re-calibrate the system when the environment is changed. The geometrical shapes of the

field generating elements have to be fixed without any twisting. If the field generator do deform, the resulting position responses will no longer be valid.

6.4 3-D MECHANICAL IMPLEMENTATIONS

For practical applications, the shape of field generating elements can be maintained by fixing them in non-metallic materials such as solid plastic. The size of the field sensing elements can be reduced in order to be inserted into a "pill". The well trained ANN model can be fabricated into a chip for real-time signal processing purposes.

The miniature transmitting antenna can be integrated with the field sensor for P&O defined magnetic field measurements and signal transmitting. The miniature transmitting antenna can be integrated with a signal processing unit for 3-D P&O determination.

The field generator coils can be mounted on a solid plastic piece of elliptical shape that fits the human body. The plastic part also hosts the microcontroller, the receiving miniature antenna, the controllable switches and the battery. The microcontroller is used to control the excitation and measurement by signalling the controllable switched. The battery is the power source for magnetic field generation.

6.4.1 Number of turns for each coil

The number of coils for field generating/sensing elements can be used to linearly adjust the strength of emf_{am} signal (6-23). The signal strength has to be sufficient enough for accurate measurements:

$$emf_{am} = 2\pi f N_1 N_2 \boldsymbol{B}_{am}(x,y,z) \bullet \boldsymbol{S}(\phi,\theta,\varphi) \tag{6-23}$$

where N_1 is the number of turns for field generator, N_2 is the number of turns for field sensor and f is the excitation frequency.

6.4.2 Frequency selection

The emf_{am} signal is also linearly proportional to the excitation frequency f. High frequency excitation is good for enhancing the emf_{am} signal we are trying to measure. However, it has to be avoided because of high losses inside the human body. Also, for a given magnetic field, the eddy current in non-metallic materials increases when the excitation frequency increases. The eddy current induces its own magnetic field, which affect our original magnetic field generated by field generator.

For low-frequency excitation, the magnetic field contributed by eddy current is negligible for non-metallic materials. For high frequency, the effect of eddy current is significant and cannot be neglected.

6.4.3 Geometrical shapes selection

The geometrical shapes of field generating elements have to be selected in such a way that associates a unique $[x \quad y \quad z]^T$ position with a given $\boldsymbol{B}_{am}^{mag}$ signal. Furthermore, the $\boldsymbol{B}_{am}^{mag}$ signals have to be sensitive to position changes in order for ANN to "learn" the input/output relationship and give accurate responses.

6.4.4 Heterogeneous medium

In reality, the human body is heterogeneous. The values of the conductivity σ and the permittivity ε are dependent on the type of tissue. The permittivity ε will not affect our measurement accuracy because it does not affect the magnetic field at low frequencies.

The position dependency of the conductivity σ is good for our MTS. Because the position dependent σ makes the conducting path less "conducting" compared to the homogenous medium. The different conducting properties create different conducting blocks, which partially inhibit the current flow. In a homogeneous medium, the conductivity is uniform, so the current is relatively easy to form a conducting path.

6.5 CONCLUSIONS

We present for the first time of our portable MTS exploiting ANN and SM modeling. We design the suitable geometry configuration for field generating and field sensing elements such that patients can carry the MTS as simple as a "jacket" during the examination without affecting their regular activities. Under this design constraint, we optimize the geometrical shape of the field generating elements of field generator in order to achieve signals of high sensitive with respect to position change.

A MatLab [20] program is developed to model the electromagnetic filed distribution and the resulting induced signal. PE is implemented in MatLab (Optimization Toolbox) to verify the mathematical algorithm of P&O determination.

We apply the ANN model to do the computational task for real-time position tracking, which is traditionally done by the iterative PE process. We utilize SM modeling for system calibration to improve the accuracy of position responses. The quality of the determined orientation is evaluated by a Quality Factor (QF) as in 6-21. As a result, we know how accurate the orientation measurement is in advance without knowing the actual orientation.

We combine the ANN and SM modeling to achieve fast computational time and accurate P&O determination simultaneously so that we can avoid the time consuming complex fine model development. Very good match of P&O is obtained between our calculated P&O and the actual P&O.

REFERENCES

[1] Given Image, Israel. (n.d). *Overview of Capsule Endoscopy*. Retrieved July 29, 2008, from http://www.givenimaging.com/en-us/Patients/Pages/pagePatient.aspx

[2] Olympus Corp, Japan. (2008). *EndoCapsule*. Retrieved July 29, 2008, from http://www.nano-tera.ch/nanoterawiki/EndoCapsule

[3] RF System Lab, Japan. (n.d). *The Next Generation Capsule Endoscope: Sayaka*. Retrieved July 29, 2008, from http://www.rfamerica.com/sayaka/index.html

[4] Intro Medic KIST, Korea. (2008). *MicoCam*. Retrieved July 29, 2008, from *http://www.nano-tera.ch/nanoterawiki/MicroCam*

[5] Jinshan Science & Technology, China. (2008). *OMOM*. Retrieved July 29, 2008, from http://www.nano-tera.ch/nanoterawiki/OMOM

[6] T. Nagaoka and A. Uchiyma, "Development of a small wireless position sensor for medical capsule devices," IEEE EMBS. *International Conference*., Sept. 2004.

[7] W. Hou, X. Zheng, and C. Peng, "Experimental Study of Magnetic-based Localization Model for Miniature Medical Device Placed Indwelling Human Body," *IEEE Conference*, Changhai, China, pp. 1309-1312, Sept. 1-4, 2005.

[8] E. Paperno, I. Sasada, and E. Leonovich, "A new method for magnetic position and orientation tracking," *IEEE Trans. Magn*., vol. 37, pp. 1938-1940, July 2001.

[9] E. Paperno, and P. Keisar, "Three-Dimensional Magnetic Tracking of Biaxial Sensors," *IEEE Trans. Magn*., vol. 40, no. 3, pp. 1530-1536, May 2004.

[10] M. H. Bakr, K. Wang and M. J. Deen, "Accuracy Improvement of Magnetic Tracking Systems Using ANNs and Space Mapping Modeling," *ACES Conference*, Niagara Falls, pp. 603-608, March 2008.

[11] NDI. (2008). *NDI Electromagnetic (EM) Tracking Technology*, Retrieved July 30, 2008, from http://www.ndigital.com/medical/technology-em.php

[12] Ascension Technology Corporation. (2008). *Tracking 3D World*, Retrieved July 30, 2008, from http://www.ascension-tech.com/index.htm

[13] M. Schneider, "Measuring Position and Orientation using Magnetic Fields," U.S. Patent 6,073,043, June 2000.

[14] F. H. Rabb, "Remote Object and Orientation Locator," U.S. Patent 4,314,251, Feb. 1982.

[15] A. S. Edelstein, "Magnetic Tracking Methods and Systems," U.S. Patent 6,675,123 B1, Jan. 2004.

[16] P. T. Anderson, G. L. Beauregard and C.D. Cherry, "Magnetic Tracking System," U.S. Patent 7,096,148 B2, Aug. 2006.

[17] J. W. Bandler, Q. S. Cheng, S. Koziel, and K. Madsen, "Why space mapping works," *Second Int. Workshop on Surrogate Modeling and Space Mapping for Engineering Optimization, SMSMEO-06*, Lyngby, Denmark, Nov. 2006.

[18] *DSP Lock-In Amplifier model SR850*, Stanford Research Systems, 1999.

[19] *3478A Multimeter*, Hewlett-Packard, 1981.

[20] MatLab ver. 7.1, The MathWorks Inc, 3 Apple Hill Drive, Natick, MA 01760-2098, USA, 1994, http://www.mathworks.com/

[21] Q. J. Zhang, K. C. Gupta. *Neural Networks: For RF and Microwave Design*. Boston: Artech House, 2000.

[22] S. Haykin. *Neural Networks: A Comprehensive Foundation (2nd Ed)*. Prentice Hall, 1999.

[23] ***NeuroModeler*** Ver. 1.5, Carleton University., 1125 Colonel By Drive, Ottawa, Canada, K1S 5B6.

CHAPTER 7

CONCLUSIONS

In this thesis, we presented an investigation of portable Magnetic Tracking Systems (MTS) for real-time Position and Orientation (P&O) determination. This MTS is applicable for wireless endoscopy applications. Our approach efficiently recovers the P&O of the sensor with respect to reference coordinate frame. For the first time, Artificial Neural Networks (ANN) and Space Mapping (SM) Modeling are utilized in MTS in order to determine the P&O information in an accurate real time manner.

Chapter 2 briefly reviewed the basic concepts of MTS. These include its hardware assemblies, Degrees-Of-Freedom (DOF), reference coordinates frame and P&O parameters calculations. Various implementations were presented and its features were highlighted for comparison purposes. We presented how to utilize Faraday's induction law and Biot-Savart's law to implement our own portable MTS for wireless endoscopy application.

Chapter 3 reviewed the concept of ANN, including its structures, information propagation and the development of ANN model. The existence of accurate ANN model

for any complex problems is guaranteed according to Universal Approximation Theorem. The mathematical formulation for ANN training process was presented. The utilized software (***NeuroModeler***) was introduced for automated ANN model generation.

In Chapter 4, we briefly reviewed the concept of SM and its framework for optimization and modeling. We presented different mapping methods in SM to match surrogate model responses with the time intensive fine model responses. The Parameter Extraction (PE) procedure is important to establish the mapping and updating surrogate model. The framework for SM optimization and SM modeling is present step by step.

In Chapter 5 and Chapter 6, we presented our portable MTS exploiting ANN and SM modeling. We designed the suitable geometry configuration for the magnetic field generator and the field sensor such that patients can carry the MTS during the examination without affecting their regular activities. Under this design constrain, we optimized the geometry shape of the field generating elements of field generator in order to achieve signals of high sensitivity with respect to P&O change.

A MatLab program was developed to model the electromagnetic filed distribution and the resulting induced signal. PE was implemented using the MatLab optimization toolbox to verify the mathematical algorithm of P&O determination.

We applied ANN model to carry out the computational task for real-time P&O tracking, which was traditionally done by the iterative PE process. We utilized SM modeling for system calibration to improve the accuracy of P&O responses. The quality of the determined orientation was evaluated by a Quality Factor (QF). As a result, we

knew how accurate the orientation measurement was in advance without knowing the actual orientation.

We combined the ANN and SM modeling to achieve fast computational time and accurate P&O determination simultaneously so that we avoided the time consuming complex fine model development. Very good match of P&O was obtained between our calculated P&O and the actual P&O.

The author suggests the following future research points:

1 Improvement in the accuracy of P&O determination.

The accuracy has to be further improved to help surgeons during surgery. In the area of small intestine, the intestines are closely packed. Within limited position accuracy, there is a possibility that the calculated location is actually in the neighboring section of the small intestine.

2 Developing miniature antenna for signal transmitting.

A miniature antenna fitted in the "pill" has to be designed for signal transmission. The heterogeneous medium properties have to taken into account as it can attenuate the transmitted signals, thus affecting the received signal characteristics and its signal-to-noise ratio.

3 Developing a detailed model with heterogeneous medium.

In a heterogeneous medium, the permeability μ will be position dependent. We have to re-simulate the magnetic field to generate proper data for ANN model training. The position dependent conductivity σ actually improves the measurement accuracy

since it partially inhibits the current flow. The permittivity ε will not affect our measurement accuracy because magnetic field measurements are not affected by ε.

4 Miniaturization for the sensing system.

Technologies have to be combined and the size has to be shrunk in order to be fitted into a "pill". Miniaturization has to be applied to optical imaging components, electronic components and the power consumption. The trick is to simplify and combine two parts with close proximity together instead of shrinking everything in size and adding them up. For example, the P&O dependent signals induced in the sensor can be further reused for the powering purposes.

5 Correlating P&O information with observation images.

The resulting P&O information can be correlated with the observation images to monitor the recovery status. As a result, every point in the observation images will have P&O information associated with it. This will help physicians to determine whether the original problem is getting worse or it is an entirely new problem.